Optical Coherence Tomography for Dermatological Applications

Borup Thomsen, Jakob

2011

Citation for published version (APA):
Borup Thomsen, J. (2011). *Optical Coherence Tomography for Dermatological Applications*. [Doctoral Thesis (monograph), Atomic Physics]. Division of Atomic Physics, Department of Physics, Faculty of Engineering, LTH, Lund University.

Total number of authors:
1

Optical Coherence Tomography for Dermatological Applications

Jakob Thomsen

Division of Atomic Physics
Department of Physics
Lund University
2011

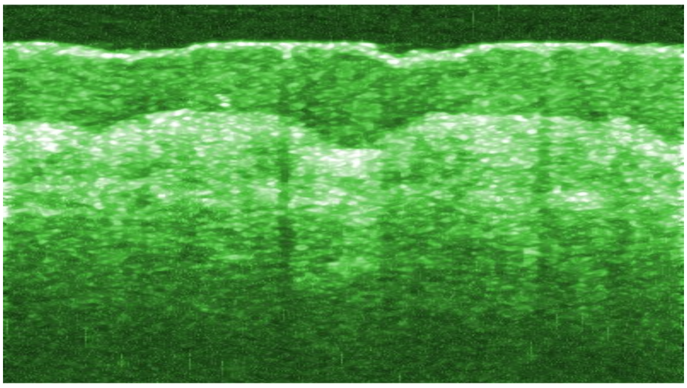

Doctoral Thesis

LUNDS
UNIVERSITET
Lunds Tekniska Högskola

Optical Coherence Tomography
for Dermatological Applications

Printed in Sweden by Media-Tryck, Lund, 2011

Division of Atomic Physics
Department of Physics
Faculty of Engineering, LTH
Lund University
P.O. Box 118
SE-221 00 Lund
Sweden

http://www.atomic.physics.lu.se

ISSN 0281-2762
Lund Reports on Atomic Physics, LRAP-433

ISBN 978-91-7473-079-1

Abstract

Optical coherence tomography (OCT) is a non-invasive optical imaging technique providing $\sim$10 μm resolution of tissue in vivo. Within ophthalmology, OCT has already proven its value and is routinely used for diagnosing retinal diseases. In many other areas the potential of OCT is explored worldwide, while the technique itself is further developed with improved imaging speed, resolution and extensions such as functional imaging.

This thesis focuses on improvements and tailoring of OCT for applications within dermatology, especially skin cancer diagnostics. A two-fold approach combining clinical measurements and development of better suited OCT equipment has been attempted. The diagnostic value at the current stage of OCT has been evaluated in a cooperation with medical doctors. The study included 100 patients and showed a need for further improvements of the technique to make accurate diagnosis possible. Studies with a smaller number of patients investigated the possibility of using OCT for thickness measurements of lesions and human nails. The results were in correlation with ultrasound measurements, but with a higher precision. In addition to these diagnostic studies, an attempt to monitor treatment progress of photodynamic therapy was initiated. The use of Doppler OCT for measuring blood flow changes has the potential to tailor the treatment individually eventually with an improved outcome. A Doppler OCT system was tested using phantoms and normal skin followed by patient investigations. Addressing the technical difficulties of performing these measurements and suggesting possible solutions was the major outcome.

Regarding the technical development, the primary concern was to improve the resolution of the imaging technique, in particular the depth resolution. A high depth resolution OCT system was constructed for imaging with a resolution of about 2 μm and this system was tested with a number of light sources. The possible advantages for diagnostic purposes were not evaluated because none of the light sources were suited for imaging. The focus has therefore been testing of the system showing promising results. With a suited light source the diagnostic value of an increased resolution might be evaluated using this system.

Populärvetenskaplig sammanfattning

Cancer diagnostics is an increasingly important task in the modern world due to an increasing cancer incidence and because diagnostics and treatment are given higher priority. There are many requirements to a diagnostic system. First of all it is important to provide an accurate diagnosis to be able to choose the right treatment. In addition, it is preferable that the method is non-invasive opposite the common used biopsy. Moreover, a relative quick method without any post processing is advantageous. Finally, a relative cheap method is preferable not to prevent widespread use. In general there are no diagnostic systems today fulfilling all criteria mentioned above. Therefore intensive research in new diagnostic systems is performed including optical methods. Optical coherence tomography (OCT) is a non-invasive optical technique providing real time images of tissue with a resolution of about 10 μm. The technique is simple and therefore relative low cost commercial systems are potentially realizable. However, it is still an open question whether OCT images can replace biopsies.

The scope of this project is to investigate if OCT can contribute to an improved diagnosis of skin diseases, in particular skin cancer. This has been accomplished by performing clinical measurements as well as improvement and tailoring of the technique. In cooperation with medical doctors, the main clinical study involved 100 patients with skin cancer and investigated the potential for diagnostics. This study revealed that technical improvements are needed before OCT might be used. An improved spatial resolution enables visualization of finer details in the images and could be important for the diagnostic value of OCT. The technical part of this project has therefore been focused on improving the resolution to a level enabling single cell visualization. An OCT system supporting imaging with a resolution of about 2 μm has been constructed. The system has been tested with preliminary light sources developed in an European collaboration with promising results. Unfortunately, the light sources have not been fully developed and therefore clinical measurements using the system have not been possible.

In addition to the diagnostic studies and development of the technique itself,

monitoring of treatment has been attempted. Using a Doppler OCT system it is possible to detect the blood flow in the skin. During treatment of skin cancer using photodynamic therapy, measurement of changes in blood flow has been attempted because it is hypothesized that this could be used for determining the treatment effect. Potentially, the blood flow information could be used for tailoring the treatment individually to every patient and eventually improve the outcome. These introductory measurements have identified a number of problems and possible solutions are suggested.

Populärvetenskaplig sammanfattning (Danish)

Diagnostik af kræft sygdomme er en atter voksende opgave i dagens samfund, idet forekomsten er voksende og fordi diagnostik og behandling prioriteres højerere og højere. Kravene til et diagnostisk system er mange. Først og fremmest er det vigtigt at kunne stille en nøjagtig diagnose for at kunne sætte ind med den rette behandling. Desuden er det ønskeligt, at metoden er ikke-invasiv i modsætning til de traditionelt benyttede vævsprøver. Endvidere er det bekvemt, at den diagnostiske undersøgelse er hurtig at foretage og ikke behøver tidskrævende efterbehandling før en diagnose kan stilles. Endelig er det en fordel, hvis metoden ikke er for kostbart, så udbredelsen af teknikken ikke begrænses unødigt. I dag findes generelt ingen ideelle diagnostiske systemer der opfylder alle kravene ovenfor og derfor forskes intensivt i nye metoder til diagnostik, heriblandt nyere optiske metoder.

Optisk kohærenstomografi (OCT) er en ikke-invasiv teknik der optager realtime billeder af levende væv. Da teknikken er relativ enkel, er der potentiale for at færdige systemer kan blive forholdsvis billige. Det er imidlertid ikke eftervist, at OCT har den fornødne nøjagtighed til at erstatte nuværende metoder. Formålet med dette projekt er netop at belyse om OCT kan bidrage med forbedret diagnostik af hudsygdomme, specielt hudkræft. Dette er forsøgt ved dels at lave kliniske målinger, men i høj grad også ved forfining af teknikken. For at undersøge det kliniske potentiale, er der via samarbejde med læger udført flere rækker af patientmålinger. Den primære undersøgelse involverende 100 patienter med hudkræft og forsøgte at kortlægge muligheden for diagnostik. Disse indledende resultater tyder på, at der i høj grad er behov for tekniske landvindinger før OCT har diagnostisk relevans i forbindelse med hudkræft. En øget opløsning der muliggør visualisering af finere detaljer er muligvis en forbedring der kan betyde rigtig meget for den diagnostiske værdi af OCT. Den tekniske udvikling har derfor primært været fokuseret på at øge opløsningen. Målet har været at opnå en opløsning så enkelte celler kan visualiseres, hvilket antages vigtigt for diagnostiske formål. I projektet er der konstrueret et OCT system beregnet til billeddannelse med omkring 2 *μm* dybde opløsning. Systemet er testet med foreløbige lyskilder fra et europæisk samarbejde, men har endnu ikke været brugt til kliniske målinger pga. mangel på egnede lyskilder.

Foruden diagnostiske studier og udvikling af selve teknikken, er der endvidere undersøgt muligheden for at monitorere en behandling. Med et Doppler OCT system er det muligt at detektere den ganske beskedne blodgennemstrømning i huden. I forbindelse med behandling af hudtumorer med fotodynamisk terapi, er der målt på ændringen i blodgennemstrømningen, idet dette formodes at kunne relateres til effekten af behandlingen. Potentielt kan disse informationer bruges til at skræddersy behandlingen til den enkelte patient og i sidste ende forbedre behandlingens effektivitet. Resultaterne af disse indledende målinger har identificeret en række praktiske problemer og mulige løsninger til disse.

List of Publications

I H. Morsy, M. Mogensen, J. Thomsen, L. Thrane, P. E. Andersen, G. B. Jemec, *"Imaging of cutaneous larva migrans by optical coherence tomography"*, Travel Medicine and Infectious Disease, **5**(4), 243-246 (2007)

II M. Mogensen, J. B. Thomsen, L. T. Skovgaard , G. B. E. Jemec, *"Nail thickness measurements using optical coherence tomography and 20 Mhz ultrasonography"*, British Journal of Dermatology, **157**(5), 894-900 (2007)

III M. Mogensen, B. M. Nürnberg, J. L. Forman, J. B. Thomsen, L. Thrane, G. B. E. Jemec, *"In vivo thickness measurement of basal cell carcinoma and actinic keratosis with optical coherence tomography and 20 Mhz ultrasound"*, British Journal of Dermatology, **160**(5), 1026-1033 (2009)

IV M. Mogensen, T. M. Jørgensen, B. M. Nürnberg, H. Morsy, J. B. Thomsen, L. Thrane, G. B. E. Jemec, *"Assessment of optical coherence tomography imaging in the diagnosis of non-melanoma skin cancer and benign lesions versus normal skin: observer-blinded evaluation by dermatologists and pathologists"*, Dermatologic Surgery, **35**(6), 965-972 (2009)

V L. Thrane, H. E. Larsen, K. Norozi, F. Pedersen, J. B. Thomsen, M. Trojer, T. M. Yelbuz, *"Field programmable gate-array-based real-time optical Doppler tomography system for in vivo imaging of cardiac dynamics in the chick embryo"*, Opt. Eng., **48**(2), 023201 (2009)

Related work by the author

- J. B. Thomsen, M. Mogensen, H. Morsy, T. Jørgensen, L. Thrane, P. Andersen, G. B. E. Jemec, *"Optical coherence tomography in dermatology"*, 9th

MICCAI conference, MICCAI workshop on biophotonics imaging, Lyngby (DK), 6 Oct 2006. IMM-Technical report-2006-17 p. 83-92

- Poster presentation at “Biophotonics Summer School”, Ven (Sweden), 2007

- J. Thomsen, N. Bendsøe, K. Svanberg, S. Andersson-Engels, T. M. Jørgensen, L. Thrane, H. E. Larsen, F. Pedersen, P. E. Andersen, *“Optical Doppler tomography for monitoring vascularization during photodynamic therapy of skin cancer lesions”*, Photonics Europe 2008, Strasbourg (France). SPIE Proceedings Series, 6991, 699118

- J. B. Thomsen, B. Sander, M. Mogensen, L. Thrane, T. M. Jørgensen, G. B. E. Jemec, P. E. Andersen, *“Optical coherence tomography: Technique and applications”. In “Advanced Imaging in Biology and Medicine”.* Technology, Software Environments, Applications. Sensen, C.W.; Hallgrimsson, B. (eds.), (Springer, Berlin, 2009) p. 103-130

Abbreviations

BCC	Basal Cell Carcinoma
D-OCT	Doppler Optical Coherence Tomography
FD-OCT	Fourier Domain Optical Coherence Tomography
FPGA	Field programmable gate array
FWHM	Full Width Half Maximum
MM	Malignant Melanoma
NMSC	Non Melanoma Skin Cancer
OCM	Optical Coherence Microscopy
OCT	Optical Coherence Tomography
PCF	Photonic Crystal Fiber
PS-OCT	Polarization Sensitive Optical Coherence Tomography
SD-OCT	Spectral Domain Optical Coherence Tomography
SS-OCT	Swept Source Optical Coherence Tomography
TD-OCT	Time Domain Optical Coherence Tomography
UHR OCT	Ultra-high Resolution Optical Coherence Tomography

Contents

Chapter 1

Introduction to OCT

The scope of this project has been to develop OCT equipment for dermatological applications, especially diagnostics of non-melanoma skin cancer. An improvement of the depth resolution has been the primary goal of the technical development. Furthermore, the potential of OCT as a diagnostic tool has been explored through clinical measurements on humans. Even though this thesis is focused on applications and development of OCT within dermatology, this introductory chapter will serve as an overview of technique and the wide variety of applications. Hopefully, this will make the rest of the thesis easier digestible and motivate the project.

Optical coherence tomography (OCT) is a non-invasive optical imaging technique that has developed rapidly since the first realization in 1991 [1]. At present OCT is commercially available and accepted as a clinical standard within ophthalmology for diagnosis of retinal diseases. Applications within biology and medicine are currently explored by many research groups worldwide. In parallel efforts are aimed at technical improvements regarding imaging speed, resolution, image quality and functional capabilities. OCT is often characterized as the optical analogue to ultrasound using light instead of sound to probe the sample and map the variation of reflected light as a function of depth. OCT is capable of providing real-time images with a resolution typically better than 10-20 μm and imaging with a resolution of 1 μm or less have been demonstrated [2, 3, 4]. The penetration depth is highly tissue dependent and is typically limited to a few millimeters. The combination of high resolution and relatively high imaging depth places OCT in a regime of itself filling in the gap between ultrasound and confocal microscopy.

1.1 The technique

Optical coherence tomography is based on interference of light, which is related to the coherence properties of light. In contrast to a laser radiating nearly monochromatic light OCT employs a broadband light source emitting polychromatic light. In this section the principle of operation is explained referring to the first implementations, so-called time domain OCT (TD-OCT). In 1995 a more effective scanning scheme known as Fourier domain OCT (FD-OCT) was introduced improving imaging speed. The principle of FD-OCT will also be explained followed by a discussion of resolution, choice of wavelength and functional OCT.

1.1.1 Time domain OCT

The principle of OCT may be explained with reference to figure 1.1 [5, 6, 7]. A Michelson interferometer as shown in figure 1.1a can be used to measure the ability of light to interfere with itself, i.e. the ability to amplify or blur itself ('constructive' and 'destructive' interference, respectively). Light is split into two paths using a beam splitter (half transparent mirror). The light directed against the mirrors are reflected, recombined at the beam splitter and detected. Interference between the two reflections is possible only when the path lengths of the two arms are matched within the so-called coherence length of the light source. The coherence length is determined by the spectral width of the light - a broad optical spectrum corresponds to a short coherence length and a narrow optical spectrum to a long coherence length. When using a light source with a large coherence length interference arises for even relatively large differences in path length. When correspondingly using a source with a small coherence length interference only arises when the two path lengths are matched within the so-called coherence length of the light. The coherence length determines the axial resolution. It is exactly this effect that is used in OCT for distinguishing signals from different depths of the sample. Consider one of the mirrors in the Michelson interferometer interchanged with a biological sample as shown in figure 1.1b. Then every position of the scanning mirror corresponds to collection of signal from a thin slice in the sample. In other words, determining from where the reflection originates is possible. Assuming a light source with Gaussian spectral shape, the intensity I of the interference signal measured at the detector can be expressed as [6]

$$I \propto \cos(2\omega_0 \Delta l / v_p) \exp(-2\Delta l^2 \sigma^2 / v_g^2) \qquad (1.1.1)$$

where ω_0 denotes the optical frequency of the light, Δl the path length difference between sample and reference arm, v_p the phase velocity of light, v_g the group velocity of light and σ the spectral bandwidth of the light source (1/e value). Eqn. (1.1.1) describes a sinusoidal signal as function of Δl superposed an exponential

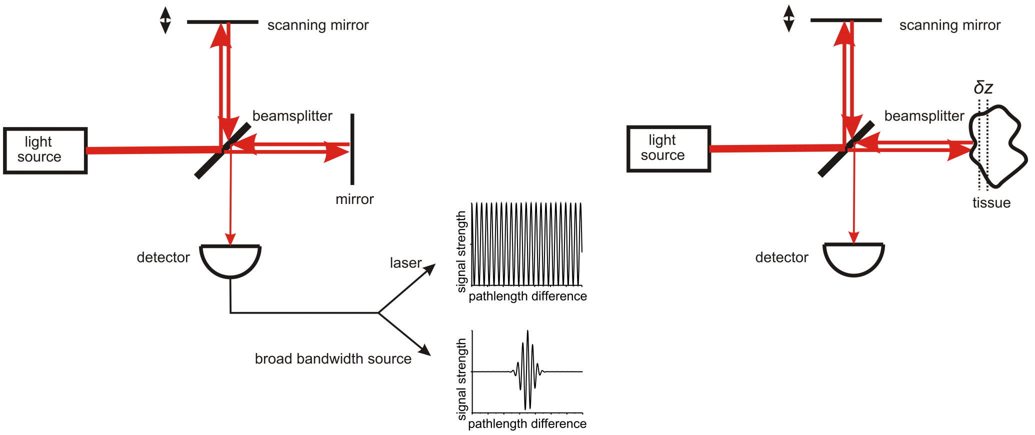

a) b)

Figure 1.1: a) A Michelson interferometer and the interferometric signal b) A Michelson interferometer with the fixed mirror replaced by a sample.

decreasing function of Δl. In figure 1.1a the interference signal in eqn. (1.1.1) is shown with a light source emitting a broadband spectrum. It is evident from eqn. (1.1.1) that the exponential function decreases more rapidly for larger values of σ, i.e. the broader the optical spectrum, the thinner slice contributes to the signal. The thickness δz of the slice that contributes to the signal, see figure 1.1b, is equal to the depth resolution of the system and inverse proportional to the bandwidth σ of the light source according to eqn. (1.1.1), see also section 1.1.3 (the larger bandwidth the better resolution). The mechanism for selecting signal from a specific depth is also referred to as coherence gating. By moving the scanning mirror the coherence gate successively selects interference signal from different depths. In this way a depth scan recording can be obtained, also referred to as an A-scan. The depth scanning range is limited by the mirror displacement. Transverse resolution is determined by the spot size, which can be changed with the focusing optics. It is important to point out that transverse and depth resolution, respectively, are independent opposite to for example microscopy, see section 1.1.3. Two dimensional data is obtained by moving the beam across the sample while acquiring data (B-scan). By translating the beam in two directions over a surface area three dimensional data can be collected. The A-scan rate is the fundamental quantity determining the image acquisition time when B-scan images are acquired. Imaging in a plane parallel to the surface at a certain depth of the sample is known as én face imaging. The interference signal is amplified, filtered to improve the signal-to-noise ratio and then digitized and transferred to a computer. From the digital signal the reflection strength is extracted. Data is typically presented in an image using either a gray scale or color palette. A free-space optical beam propagation as sketched in figure 1.1 is possible even though optical fiber-based systems are more convenient for clinical use. In figure 1.2a a commercial OCT system for ophthalmologic diagnostics is shown (Zeiss), figure 1.2b shows a fiber-based prototype OCT system in a clinical environment, figure 1.2c an OCT image of the human retina and 1.2d an image acquired on the human skin.

1.1.2 Fourier Domain OCT

In the TD-OCT scheme an A-scan is acquired by successively moving the coherence gate recording from one depth at a time. A more efficient scheme of acquiring interference data was suggested and first realized in 1995 [8], with detection of light from all depths of the sample simultaneously. This method is referred to as Fourier domain OCT and can be further divided into spectrograph based systems, denoted spectral domain OCT (SD-OCT), and swept source OCT (SS-OCT) employing a scanning laser and single detector[1]. In figure 1.3a a typical setup for SD-OCT is shown. The light source used is the same as for TD-OCT but the reference mirror is fixed. At the interferometer output a spectrograph is used for detection, i.e. light is dispersed using for example a grating, meaning split into single wavelengths or equivalent wave numbers k, and every component is detected with a separate detector (array detector). The intensity $I(k)$ measured with the array detector consist of the superposition of light from the reference arm and the sample

$$I(k) = S(k) \mid \exp(i2kr) + \int_{z_0}^{\infty} R(z) \exp(i2kn(r+z)) dz \mid^2 \tag{1.1.2}$$

where $k = 2\pi/\lambda$ is the wave number, $S(k)$ the power spectrum of the light source, n the refractive index of the sample, $R(z)$ the amplitude of the backscattered light from the sample, z_0 is the offset between reference plane and sample surface related to the mirror position, $2r$ is the path length of the reference arm and $2z$ is the path length difference between reference arm and sample. Without loss of generality it is assumed in eqn. (1.1.2) that light from the reference arm is reflected without loss. It is only the interference term in eqn. (1.1.2) corresponding to the cross term that carries depth information

$$I(k)_{int} \propto S(k) \int_{z_0}^{\infty} R(z) \cos(2knz) dz \tag{1.1.3}$$

---

[1] Unfortunately there is no convention about the names, hence FD-OCT and SD-OCT are frequently interchanged.

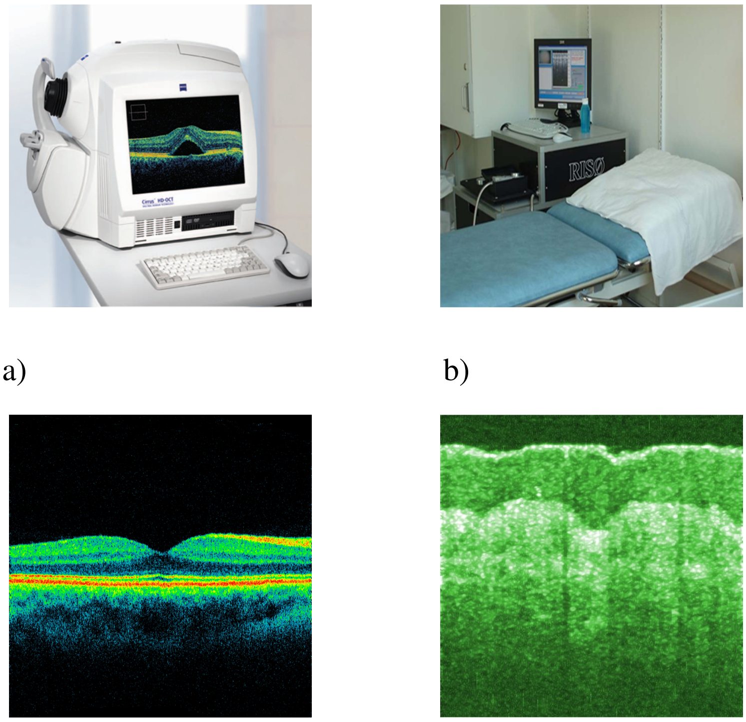

a) b)

c) d)

Figure 1.2: a) Zeiss Cirrus OCT system tailored for ophthalmology (courtesy Carl Zeiss Meditec AG) b) Prototype OCT system in a clinical environment c) OCT image of the healthy retina in a human eye showing distinct retinal layers d) OCT image of human skin (palmar aspect, thumb) with a clear visible boundary between the stratum corneum (dark upper layer) and the living part of epidermis, and a visible change from a high intensity band (epidermis) to a darker area (dermis).

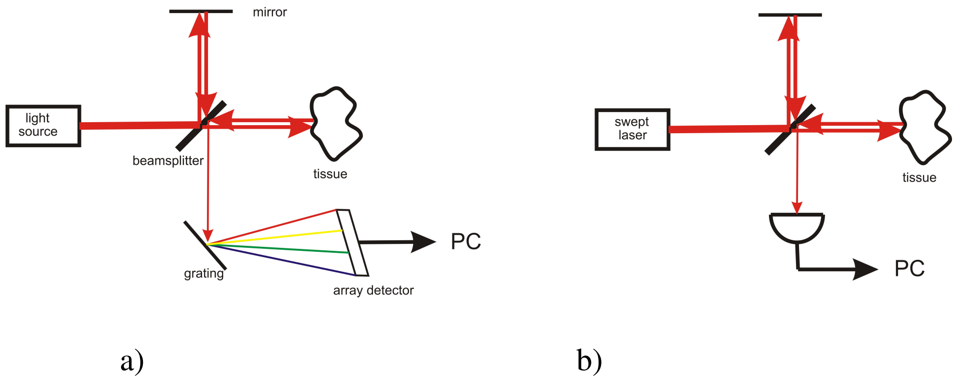

Figure 1.3: Different embodiments of FD-OCT. a) SD-OCT b) SS-OCT system. In both cases a frequency analysis of the measured signal is needed to find the reflection strength with depth.

As seen by eqn. (1.1.3) the strength of the backscattered light $R(z)$ from a given depth z corresponds to an oscillation of $I(k)$ on the array detector with a certain frequency of π/nz. In other words, the depth information is now frequency encoded at the array detector. The strength of the backscattered light $R(z)$ can therefore be extracted from the detected signal by a frequency analysis (Fourier transform). The depth scanning range is basically limited by the resolution of the spectrograph which is closely connected to the number of elements on the array detector. From eqn. (1.1.3) it is clear that the frequency at the detector array increases with depth. The detector samples the signal in equal wavelength intervals $d\lambda$. The corresponding wave number interval $\delta k \propto k^2 \delta\lambda$ is increasing with wave number or equivalent with imaging depth. This uneven sampling results in a degradation of the resolution with depth if the detector signal is used directly. Non-linear scaling algorithms are needed to correct for this effect [6].

In figure 1.3b a typical setup for SS-OCT is shown. The broad bandwidth light source usually employed has been exchanged with a laser that can scan over a range of wavelengths. Furthermore a single detector is used. The interference signal at the detector is for each wave number given by eqn. (1.1.3), but with one detector the intensity change with wavelength cannot be measured as in SD-OCT. Instead by changing the laser wavelength with time or equivalent the wave number k by a constant rate it is seen from eqn. (1.1.3) that the frequency of the detected signal only depends on the path length difference z between sample and reference arm, i.e. the sample depth. Therefore a frequency analysis of the detector signal gives the reflection strength as a function of depth. The depth scanning range in this scheme is determined by the line width of the scanning laser because this determines the coherence length of light.

Comparing the two FD-OCT schemes, SD-OCT can be regarded as the superposition of many single-wavelength interferometers operating in parallel, whereas SS-OCT operates with one wavelength at a time. The advantage of FD-OCT systems is the simultaneous detection from all depths which may be used to increase the speed or sensitivity [9]. However there is some controversy regarding this issue. An analysis concluded that TD-OCT theoretically has the highest sensitivity followed by SS-OCT and SD-OCT [10]. Recently, a study compared the imaging depth of SS-OCT and TD-OCT experimentally and showed a superior imaging depth in favor of TD-OCT [11]. The choice of OCT implementation should therefore be determined with respect to the application, i.e. need for speed, imaging depth, resolution etc. Even though FD-OCT are considered as the modern version, TD-OCT might still have some relevance for applications not requiring fast imaging but need of high imaging depth.

While TD-OCT is limited by the speed of the scanning mirror, SD-OCT is limited by the read-out speed of the detector array or laser sweep rate, respectively. The highest achieved A-scan rate is currently 60 Mhz using a spectral domain system [12]. To overcome the limiting read-out rate of the array detector, this has been replaced by 256 photodiodes. The fastest system using a swept source achieves an A-scan rate of 20 MHz [13]. Both implementations are much faster than time domain systems that typically operate at a scale of 10 kHz. With an A-scan rate of 370 kHz a B-scan image consisting of 500 A-scans can be acquired in about 1 ms corresponding to a frame rate of roughly 1000 Hz, i.e. 1000 images per second. The fast imaging rate allows 3D data to be acquired with limited motion artifacts, which in ophthalmology for example has been used to visualize a macular hole in 3D [14].

1.1.3 Resolution and sensitivity

As mentioned above the depth resolution is dependent on the bandwidth of the light source. Assuming a Gaussian spectrum the depth resolution δz is defined as [6]

$$\delta z = \frac{2\ln(2)\lambda_0^2}{\pi n \Delta\lambda} \tag{1.1.4}$$

with λ_0 denoting the center wavelength of the light source, n the index of refraction of the sample and $\Delta\lambda$ the spectral bandwidth of the source (full width half maximum). Eqn. (1.1.4) is valid for both time and Fourier domain systems, but in practice the number of elements on the array detector can limit the resolution in SD-OCT. When the depth resolution is a few micrometers or below, the regime is denoted ultra-high resolution OCT (UHR OCT) and such resolutions have been obtained in several OCT implementations [2].

The transverse resolution δx is determined by the spot size of the optical beam [6]

$$\delta x = \frac{4\lambda_0 f}{\pi d} \tag{1.1.5}$$

where f is the focal length of the lens used for focusing and d is the diameter of the beam at the lens. As a unique property compared to for example confocal microscopy, the transverse and depth resolutions are independent (depth resolution depends on bandwidth of the source; transverse resolution depends only on focusing optics). This property makes imaging with a high depth resolution possible with a relative large working distance; for example necessary for imaging of the human retina. The spot size - and therefore the transverse resolution - varies with depth on a scale known as the depth of focus z_d given by [6]

$$z_d = \frac{\pi \delta x^2}{2\lambda_0} \tag{1.1.6}$$

As seen by eqn. (1.1.6), higher transverse resolution results in smaller depth of focus. Therefore higher transverse resolution is followed by a faster degradation of transverse resolution with imaging depth. In other words there is a trade-off between transverse resolution and the maximum imaging depth in OCT. Therefore a moderate transverse resolution is often used allowing a reasonable maximum imaging depth. In addition to this inevitable degradation of transverse resolution with depth, light scattering also causes degradation with depth which is well-known in microscopy. In the multiple scattering regime this effect is predicted substantial by theoretical models of the OCT signal [15]. The trade-off between imaging depth and transverse resolution (not including light scattering) can be overcome by overlapping the coherence gate and the position of the spot during a depth scan, so-called dynamic focusing. However, this is only possible within the TD-OCT regime because FD-OCT acquires all points in an A-scan at the same time. Using an axicon lens it is possible to maintain a small spot over a larger depth, which to some extent overcomes the problem [16]. When choosing a high transverse resolution, imaging in a plane parallel to the surface is convenient since then only slow dynamic focusing is needed. This is known as én face scanning and combined with high transverse resolution referred to as optical coherence microscopy (OCM). This imaging mode is the analog to confocal microscopy. Notice, however, that fluorescence, which is often the main contribution to the signal in confocal microscopy, is not registered using OCT because fluorescent light is incoherent. The advantage of OCM compared to confocal microscopy is an increased imaging depth because multiple scattered out of focus light is partly filtered out using the interference principle in OCT [17].

The signal to noise ratio (SNR) of an OCT system is given by

$$SNR = 10\log\left(\frac{\eta P}{h\nu NEB}\right) \tag{1.1.7}$$

where P is reflected sample power ($\propto$ source power), η the detector efficiency, h Plancks constant, ν the optical frequency and NEB the noise equivalent bandwidth equal to the electronic bandwidth of the signal. Because the electronic bandwidth increases with optical bandwidth (i.e. increased depth resolution) and with increased imaging speed, there is a trade-off between speed, resolution and SNR. The signal to noise ratio is also linearly dependent on the source power. The sensitivity is a measure of how weak signals that can be detected relative to the input and therefore relates to the maximum imaging depth. Usually sensitivity and SNR is used interchangeable even though other definitions exists [10]. Most OCT systems achieve sensitivity in the range of 90-100 dB, which means signals as small as $10^{-9} - 10^{-10}$ of the input can be detected. In figure 1.4 the resolution and penetration of OCT and OCM are sketched together with confocal microscopy and ultrasound. Confocal microscopy has superior resolution but very limited penetration whereas ultrasound has large penetration but coarser resolution. OCT and OCM fills in the gap between ultrasound and confocal microscopy with a larger penetration than confocal microscopy and higher resolution than ultrasound. Furthermore OCT does not need physical contact to the sample. Comparing OCT to other imaging modalities the lack of resolution in the favor of OCT is striking (magnetic resonance imaging, X-ray imaging for instance). Another advantage of OCT is the possibility of producing very small probes, which is highly relevant for endoscopic use where a fiber optical implementation is also advantageous.

1.1.4 Light source requirements

As already mentioned, light sources for OCT needs to emit a broad spectrum because this is equivalent to short coherence length and correspondingly high depth resolution. Furthermore optical power, spectral shape and noise characteristics are important parameters [6, 7]. Commercial turn-key sources are available, but only with a bandwidth allowing resolution on a scale of about 10 μm. Sources with larger bandwidth are desirable and achievable on a research basis i.e. more complicated and expensive setups not yet suitable for clinical use. As an example a femto-second laser pumping a photonic crystal fiber (PCF) has been used to achieve a resolution less than 1 μm [3]. Notice in this context that the same light sources can be used for both TD-OCT and SD-OCT. For SS-OCT a scanning laser is employed, which is also commercially available with a scanning range corresponding to a depth resolution of 10 μm and limited speed compared to state of the art sources developed in research. Compact and low-cost broadband sources

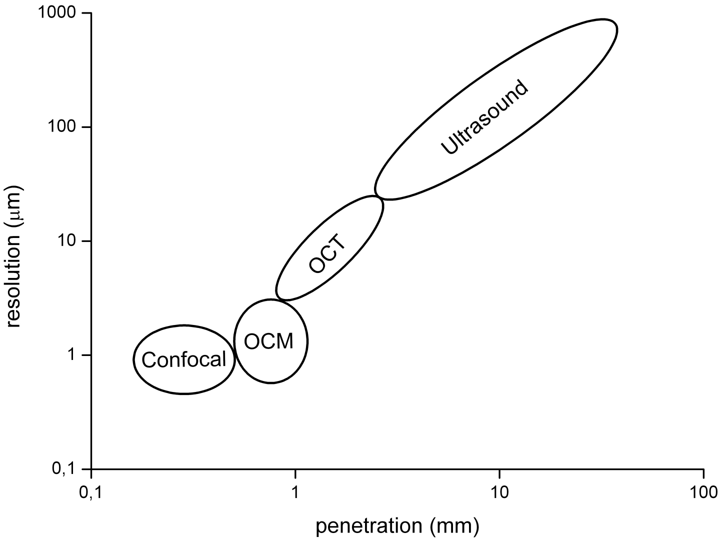

Figure 1.4: OCT and OCM compared to ultrasound and confocal microscopy regarding resolution and penetration, notice the log scale on both axes)

(including scanning lasers) are currently an active research area. The choice of wavelength is important for the imaging depth and depends on the application. When light is propagating through tissue it is attenuated by scattering and absorption. Light scattering is decreasing with wavelength which is an argument for choosing longer wavelengths. However light absorption can be considerable higher at longer wavelengths and therefore there is a trade-off when choosing wavelength. In figure 1.5 the absorption spectra of water and melanin are shown, respectively, with an indication of the regions with low light absorption known as the ’water windows’. Another issue is dispersion which is the difference in light velocity for different wavelengths resulting in a degradation of depth resolution due to different wavelengths arriving at different times at the detector. In the case of water for example, the dispersion is zero for a wavelength in the order of about 1050 nm [18]. For imaging the retina, center wavelengths in the range of 800-1100 nm are desirable to minimize the water absorption and dispersion in the outer part [19]. In highly scattering tissue, such as skin, center wavelengths in the range of 1300 nm is typically employed lowering scattering losses. In biologic tissue with low water content, experiments have shown an advantage of using a wavelength as high as 1600 nm regarding maximum imaging depth [20].

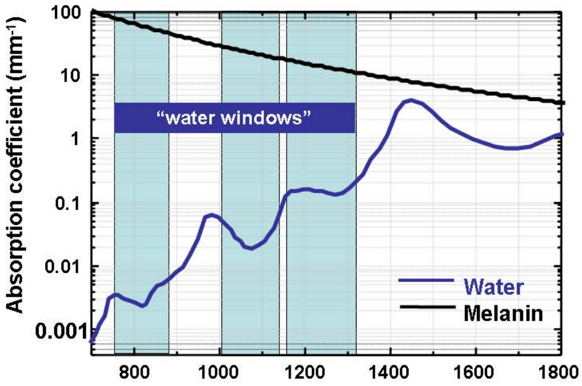

Figure 1.5: The dependency on wavelength for tissue absorption. Data from [21] and [22]

1.1.5 Functional OCT

Up to this point we have only considered the information represented by the amplitude of backscattered light referred to as structural OCT images. Functional OCT adds additional information extracted from the measured signal. This includes flow measurements by Doppler OCT (D-OCT), birefringence detection by polarization sensitive OCT (PS-OCT) or spectroscopic information (spectroscopic OCT). Functional OCT can provide valuable knowledge of the sample which is not contained in the structural OCT image.

Doppler OCT

The first system implementations of Doppler OCT acquired the velocity of the scatters by analysis of a single A-scan [23, 24]. Later, another method was introduced acquiring more A-scans in the same transverse position. By comparison of these A-scans the velocity of the scatters can be found by looking at the displacement of the signal knowing the time between two A-scans. This method is known as sequential A-scan processing and the advantage compared to the former is an increased image speed that allows real-time Doppler imaging while maintaining the capability of sub-mm/s velocity sensitivity [25]. Even though the last method measures a velocity and not the Doppler shift directly as the first implementations, it is still named Doppler OCT. A more descriptive name would be displacement sensitive OCT, but would probably introduce some confusion. Flow information is also obtainable using laser Doppler imaging but contrary to D-OCT there is no depth resolution [26]. Using D-OCT it is for example possible to visualize the embryonic vascular system at high speed [27]. Even though it is the velocity parallel to the beam direction that is measured, an absolute velocity determination without prior knowledge of the flow direction has been demonstrated by analysing the spectrum of the backscattered light [28]. The flow information can be mapped in the same way as structural OCT images using a gray scale palette but is typically shown in colors. More commonly, however, D-OCT is overlayed the structural OCT image showing the flow information in color and the structure in gray-scale, thus, making it easy to assess flow relative to structure. Measurements of total blood flow volume in the human retina was demonstrated recently *in vivo* [29]. D-OCT is expected to be important for diagnosis of a number of retinal diseases including glaucoma and diabetic retinopathy, but the research in this area is still at an early stage [30].

Polarization sensitive OCT

In general, light can be described as a transverse wave allowing two possible independent directions of the vibration plane. The direction of the vibration plane is known as the polarization plane [31]. Usually the velocity of light in a medium is independent of the polarization. However, materials exist for which the velocity depends on the polarization; these are referred to as birefringent materials or are said to exhibit birefringence ('two index of refraction'). In biological tissues it is usually highly organized tissue as for example collagen fibrils that exhibit birefringence. The net effect of light propagation through a birefringent material is a change of the polarization direction with propagation distance. Polarization sensitive OCT first demonstrated with free-space optics in 1992 is capable of measuring this change [32]. Later fiber-based polarization sensitive systems have been demonstrated [33]. PS-OCT can be used to identify tissue that is birefringent and as a diagnostic tool for diseases that break up the ordered structure resulting in a loss of birefringence. In ophthalmology it has been suggested that PS-OCT can be used for a more precise determination of the retinal nerve fiber layer thickness which is important for glaucoma diagnosis [34]. For diagnosis of age-related macular degeneration PS-OCT has also been suggested to provide important information [35].

Spectroscopic OCT

Light absorption at specific wavelengths is a signature of the sample composition and may be of great value. The use of a broadband light source in OCT makes absorption profile measurements of the sample possible, which is denoted spectroscopic OCT [36]. Spectroscopic OCT combines spectroscopy with high resolution imaging enabling mapping of the chemical structure. Spectroscopic OCT becomes increasing relevant with broader bandwidth sources since it is more likely to coincide with certain relevant or desired sample absorption lines. The technique has been used to assess the oxygen saturation level in blood [37]. Because OCT typically operates in the infrared region, elastic scattering is actually more common than absorption. Imaging separately with two different wavelengths is another spectroscopic approach which probes the wavelength dependent scattering. From these separate images a differential image can be constructed with increased contrast [38].

1.1.6 Combining OCT with other techniques

Development of multi modal systems is a popular discipline these days. Combining OCT with Raman spectroscopy and fluorescence are examples of such multi modal systems that has been attempted. The idea is to collect complimentary molecular information adding to the spatial resolved morphology provided by OCT. Considering diagnostics, OCT may be used to delineate a certain lesion while the molecular information ideally is used for increased diagnostic accuracy. Combining coherent antistokes Raman spectroscopy (CARS) with OCT was introduced in 2005 [39]. A fully integrated system combining Raman spectroscopy and OCT has been demonstrated and improved diagnostics in dermatology is suggested [40]. Fluorescence lifetime imaging is another modality which recently has been fused with OCT offering chemical information of the sample [41]. In another study, OCT and multiphoton is combined to investigate skin lesions [42]. Photoacoustic imaging measures the ultrasonic waves generated when light is absorbed in tissue, transferred to heat and leading to transient expansion. In this way the absorption of light can be measured and used for forming images. Recently, a system integrating photoacoustic and OCT was demonstrated [43]. Using a wavelength characteristic of blood absorption, vessel identification is also feasible using photoacoustic imaging [44]. Another system utilized the sound-light interaction to improve the maximum imaging depth by suppressing the influence of multiple scattering which is important for many applications including skin investigations [45]. So far, the diagnostic potential of these multi modal systems are not fully explored and future studies are needed to investigate the diagnostic power of these systems.

1.2 OCT in ophthalmology

OCT was first applied in ophthalmology and the use has expanded rapidly since the introduction of the first commercial system in 1996. Eye diseases are common and early diagnosis is important in many cases in order to avoid visual decline making high resolution imaging relevant. Today OCT is widely used clinically because it provides in vivo images of the retinal layers with higher resolution than any other technique. In order to image the retina and the optic nerve head, penetration through the outer $\sim$ 0.5 mm cornea is necessary which requires a relatively weak focus of light (long working distance) resulting in moderate transverse resolution. With confocal microscopy a weak focus inevitable leads to low depth resolution. On the other hand using OCT the transverse and depth resolutions are in-dependent (see section 1.1.3) and imaging with moderate transverse resolution does not affect the depth resolution since this is determined by the bandwidth of the light source. Therefore OCT is capable of imaging the retina in vivo with high depth resolution. Furthermore no physical contact to the eye is needed contrary to for example ultrasound. Due to the commercialization and use of OCT as a clinical standard this section is primarily concerned with the description of the use of OCT in the clinic. The ongoing technical development of OCT for ophthalmology is described in the last part of this section.

1.2.1 Commercial OCT systems for ophthalmology

The first commercial OCT system for ophthalmic use was introduced to the market in 1996 (Carl Zeiss Meditec) and in the following years the next generations of systems were released with improved resolution, speed and software (see figure 1.2a for the newest ’Zeiss Cirrus’ OCT system). More than 10000 systems have been sold by Zeiss (2008) and more producers have entered the market [46]. Today OCT is used in larger clinics but the trend is a spread into smaller clinics as well. Because cornea mainly consists of water, a wavelength of 800 nm has been preferred to minimize absorption, see section 1.1.4. The resolution is typically 5-10 μm, sufficient to distinguish different layers in the retina. Retinal structures inaccessible with any other techniques can be detected with OCT which is the reason for the success in ophthalmology. OCT is the clinical standard for a number of retinal diseases and is used on a daily basis in the clinic for diagnosis, monitoring and treatment control of for example macular holes, age related macular degeneration, glaucoma and diabetes. A review with a more complete description of ophthalmic OCT is found in [30].

1.2.2 Routine examinations of the retina using OCT

Visualization of the layered structure of the retina is possible as illustrated with the OCT image of a healthy retina in figure 1.6. The fundus image of the retina shows the fovea in the middle, the place with maximum visual resolution or power being used for example when reading or watching television. In the right part of the image the optic nerve is located with nerve fibers and blood vessels running in and out of the retina. The white bar corresponds to the position of the OCT

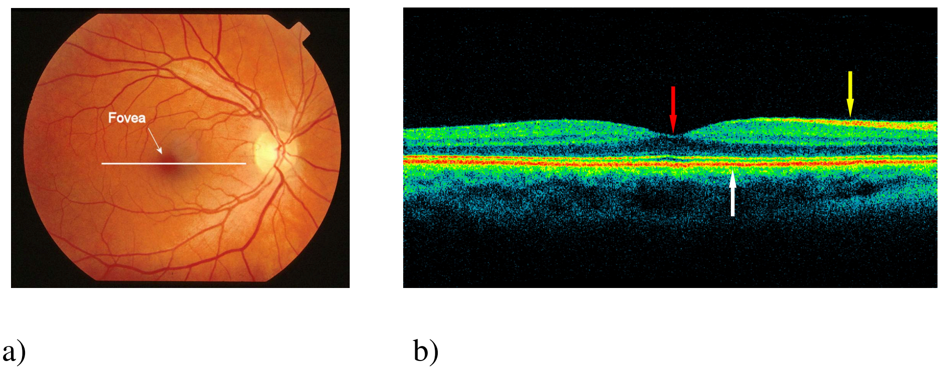

Figure 1.6: Images of a normal retina. a) Fundus image with the white line indicating the position of the OCT scan b) OCT image corresponding to the position of the white line in 3.1a (6 mm wide). Red arrow - position of fovea; yellow arrow - nerve fiber layer; white arrow - retinal pigment epithelium.

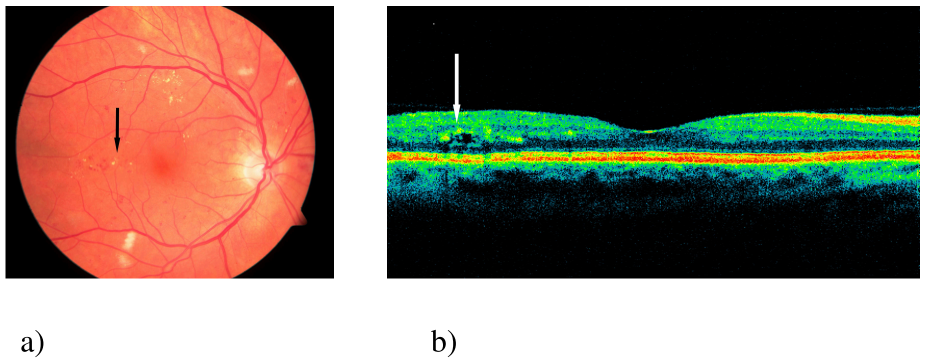

Figure 1.7: Images of the retina belonging to a diabetic patient. a) Fundus image with the arrow indicating faint protein precipitation close to the fovea b) OCT image of the retina where the protein precipitation is easily seen (white arrow).

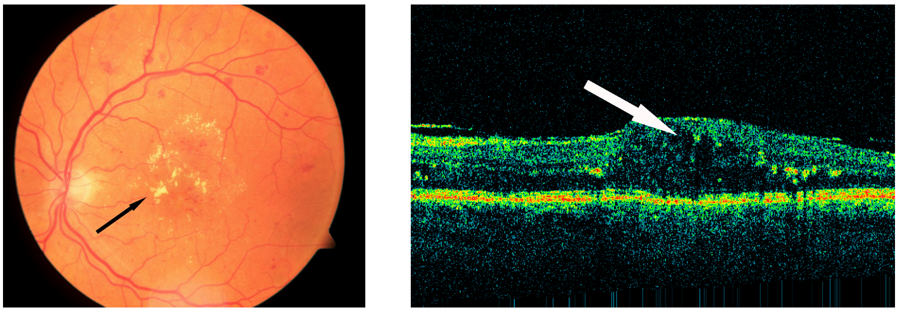

a) b)

Figure 1.8: Images of the eye from a patient with a large edema. a) Fundus image showing deposition of proteins as white spots (black arrow) b) Corresponding OCT image which clearly shows the edema (white arrow). The quality of the OCT image is reduced due to an increased scattering and absorption in the thickened retina.

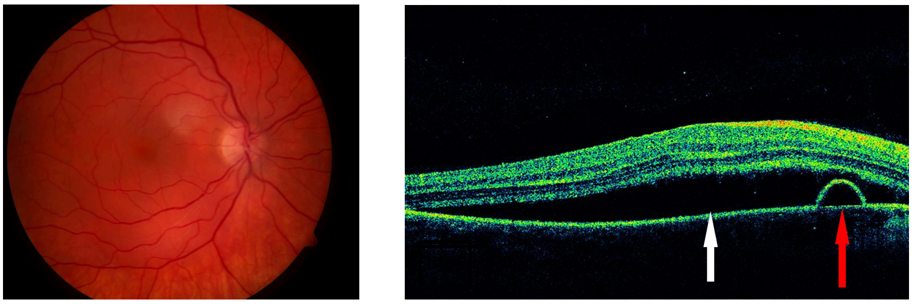

a) b)

Figure 1.9: Images from a patient with "serous chorioretinopathy" leading to a large, distinct fluid accumulation both subretinal (i.e. just anteriorly to the pigment epithelium) and a smaller, dome shaped, fluid accumulation posteriorly to the pigment epithelium. a) Fundus image b) Corresponding OCT image which clearly shows the presence of the fluid accumulation anteriorly to the pigment epithelium (white arrow) and posteriorly to the pigment epithelium (red arrow).

scan shown in figure 1.7b (6 mm, 512 A-scans). The most inner layer of the retina is the nerve fiber layer (figure 1.6) where nerve fibers carrying the signal from the photo receptors join in a layer toward the optic nerve. The fovea contains the largest density of photo receptors and is also the thinnest part of the retina, ap-proximately 160 mm thick. The nerve fiber layer is highly reflecting (red and white) while the photo receptors are less reflecting (black and blue). In the outer part of the retina the hyper reflecting retinal pigment epithelium is seen anteriorly to the underlying Bruchs membrane and choriodea. From a range of 2D OCT images reproducible thickness measurements of the retinal nerve fiber layer can be obtained [47]. The thickness of the nerve fiber layer will probably soon be an important parameter in diagnosis of glaucoma at an early stage. Diagnosis today is only possible when visual damage has happened [48]. Furthermore retinal thickness measurements and visualization of intraretinal and subretinal fluid are relevant for diagnosis and follow-up of age related macular degeneration, a disease where an effective treatment has been introduced worldwide during the last few years [49]. Macular holes developing around fovea is also easily visualized using OCT and if a small macular hole is present, the ophthalmologist might not be able to diagnose the hole by standard methods [50]. Macular edema is caused by protein and fluid depositions and is often a consequence of diabetes and may reduce visual acuity, particularly when the edema is close to the fovea. In figure 1.7 images from a diabetic patient is shown. In case of diabetes the blood vessels become fragile and the first sign is small bulges of the blood vessels in the retina. At a later stage of the disease bleeding from vessels and leakage of plasma occurs. Because plasma contains proteins and lipids, depositions of these are often noticed. This is seen as the white spots on the fundus image in figure 1.7 and as high reflecting areas in the OCT image. For the case shown in figure 1.7 the leakage close to the fovea is very limited and the corresponding lipid deposits on the fundus image relatively faint, while the OCT image show the highly reflecting deposit and an underlying shadow clearly. The evaluation of possible edema from fundus images or direct observation of the eye re-quires stereoscopic techniques and is very difficult. This can be judged by examining the OCT image instead. If edema is present some of the fragile blood vessels can be closed by laser treatment. The images in figure 1.8 are acquired on a patient with a large edema in the retina and the visual power is degraded to a level making reading difficult. On the image many depositions of protein is seen around the fovea (white spots). Even for trained medical doctors it is difficult to judge whether a thickening/edema is present and if laser treatment is necessary. On the other hand the OCT technique is capable of visualizing the edema and the retinal thickness before and after treatment is easily assessed. It is important when comparing new treatment techniques to quantify their effect for optimization and comparison. This is possible by using OCT. In figure 1.9 another example of edema in the retina is shown. In this case the patient is diagnosed with serous chorioretinopathy, a disease which seems to be related to stress. On the fundus image in figure 1.9a it is very difficult to sense the slightly difference in the red color of the retina. Within the OCT image the edema is however easily seen as indicated with the arrow in figure 1.8b. The fluid is seeping from the underlying choroidea through the retinal pigment epithelium and into the retina Moreover there is also fluid under the retina as seen to the right on the OCT. The cases shown, illustrates how the OCT image gives a unique possibility of detecting fluid accumulation in relation to a number of diseases giving rise to completely different morphological changes.

1.2.3 Future directions

OCT has just started its second decade as a commercial instrument for ophthalmologic diagnostics and treatment control. The rapid development is a sign of the clinical relevance in this area. This subsection deals with advances in OCT that can be expected to find the way to the clinic during the second decade.

When identifying retinal layers and determining layer thicknesses a higher depth resolution is advantageous. The visualization of more layers using a higher resolution has been demonstrated but the light source setup is not yet suitable for widespread clinical use [51]. With the development of broadband light sources suited for clinical use it is expected that higher depth resolution will be available in future commercial OCT systems. Improving the transverse resolution is complicated by aberrations introduced by the cornea. The use of adaptive optics can to a certain degree compensate for these aberrations [52, 53, 54]. Due to eye motion faster image acquisition is preferable and can be achieved using FD-OCT systems. The clinical advantages of using faster systems are not yet fully revealed since FD-OCT systems have just recently been released commercially. Fast systems makes 3D imaging possible and gives a more complete characterization of the retina and can result in better diagnostics and treatment control [55]. Traditionally a wavelength of 800 nm has been used for imaging the retina due to the low water absorption. To increase the penetration it is however advantageous to use a slightly longer wavelength at about 1050 nm thereby reducing the scattering, see section 2.4. Moreover the dispersion is lower in this region resulting in better preservation of the depth resolution. An improved penetration of 200 μm has been demonstrated at a center wavelength of 1040 nm [56]. The presence of speckle as a result of interference of light reflected from closely spaced scatters can reduce the contrast significantly and effectively blur the image. Different techniques to suppress speckle noise have been demonstrated resulting in a better signal to noise ratio and better delineation of retinal layers [57, 58]. Polarization sensitive OCT has recently been applied for retinal imaging [59]. The retinal nerve fiber layer exhibits birefringence and by using PS-OCT to de-lineate the borders, a better estimate of the thickness can be made. Furthermore it is known that for example glaucoma causes nerve fiber layer damage, therefore it is possible that PS-OCT can be used as a diagnostic tool for these diseases. Retinal blood flow is an important parameter in the characterization of a number of diseases such as diabetes and glaucoma and has been assessed with high spatial resolution using D-OCT [60]. More recently, the concept of optical microangiography (OMAG) has been introduced [61]. OMAG is an alternative approach to D-OCT which does not rely on extraction of phase as the method described in section 1.1.5. Therefore it is not sensitive to phase fluctuations and imaging of flow with reduced noise is possible. Retinal blood flow detection has been demonstrated using OMAG [62]. Finally, change in the amount of backscattered light from the dark-adapted retina caused by light stimulation has been demonstrated improving the understanding of retinal physiology and pathology [63].

1.3 OCT in dermatology

Skin abnormalities can generally be identified by the naked eye. However, simple visual inspection is highly dependent on operator skills and does not always allow for high diagnostic accuracy. Furthermore visual inspection only considers the surface of the skin. For this reason skin biopsies and subsequent histopathological analysis is therefore the reference standard to confirm clinical diagnosis and to examine deeper skin layers. Performing biopsies can be time consuming, is invasive and has potential complications, which is why it is relevant to investigate if a non-invasive technology such as OCT can be used as a diagnostic tool in dermatology. Besides diagnosis, OCT may be potentially useful as a non-invasive monitoring tool during treatment. Such monitoring would allow for more precise individual adjustment of topical or systematic non-surgical therapy. The main focus of OCT in the area of dermatology has addressed skin cancer although OCT has also been studied in relation to photo damage, burns and inflammatory diseases such as psoriasis and eczema.

1.3.1 Diagnosis of skin cancer using OCT

The two major skin cancer types are malignant melanoma (MM) and non-melanoma skin cancer (NMSC). MM are relatively rare but with a high mortality and increasing incidence[2]. NMSC is characterized by a high prevalence compared to MM. In United States of America more than 1 million are diagnosed with NMSC each year and the incidence appears to be rising [64]. Although the mortality is low

---

[2] In 2003, it was estimated that 54,200 Americans were diagnosed with melanoma (data from the U.S. Surveillance, Epidemiology, and End Results (SEER) registry).

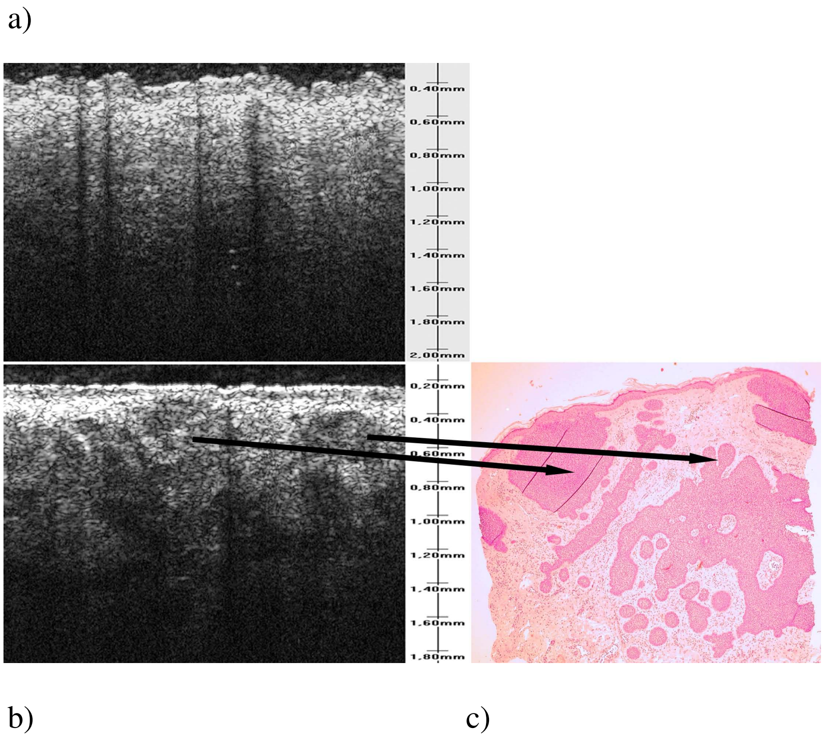

Figure 1.10: a) OCT image of normal skin b) OCT image of a BCC c) Corresponding histology (HE stain, magnification x 40). A clear structural difference between normal skin and the BCC is seen. The basaloid carcinoma cell islands main features in the histo-logical image can also be retrieved in the OCT image (arrows).

dependent on the NMSC type, the morbidity can be high caused by local tissue destruction and subsequent complications or tumor recurrence. The clinical standard for diagnosis of skin cancer is biopsy, which is invasive. In addition biopsies are usually taken as 2-4 mm punch biopsies and can therefore potentially introduce sampling errors if taken in suboptimal places for subsequent histopathological examination. Furthermore handling and processing of the biopsy takes time resulting in treatment delays and higher costs. Non-invasive *in vivo* imaging techniques such as OCT may therefore be valuable as an adjunct diagnostic tool in the clinic [65]. It is speculated that the imaging depth of OCT may furthermore be potentially useful in identifying the extent of the lesions. Determining the borders of skin cancer lesion is also relevant for choosing the optimal treatment. The typical layered structure of normal skin is shown in figure 1.10a. Usually a clear boundary between stratum corneum and the living part of the epidermis is seen in glabrous skin. The epidermis can be distinguished from dermis in OCT images [66]. Because OCT is typically not capable of resolving single cells, the diagnosis must rely on a change in the skin structure such as a break up of tissue layers, general disordered structure, a change in amount of backscattered light etc. compared to normal skin [65, 67, 66]. Malignant melanomas have been investigated in a study comparing dermoscopic observations with histology and OCT [68]. Morphological correlation was reported in 6 out of 10 cases. Differentiating benign and malignant lesions was not possible according to the authors. Improved resolution allowing single cell identification was suggested in order to make reliable diagnosis. The OCT system used in the study did not provide resolution high enough for this to be achieved. An-other group included 75 patients in a study of MM and benign melanocytic nevi and reported a loss of normal skin architecture in MM compared to benign lesions [69]. Characteristic morphological OCT features in both nevi and MM were demonstrated and confirmed by histology. Interestingly the presence of vascularity was not exclusively limited to the MM lesions [3]. The specific diagnostic accuracy of OCT was not calculated in this study. A number of studies of the diagnostic potential of OCT in NMSC have also been conducted. In contrast to reducing mortality with early MM diagnosis, the main advantage for NMSC would be the potential of reducing the number of biopsies. In figure 1.10 an OCT image of a basal cell carcinoma (BCC), the most common type of NMSC, is shown together with an OCT image of normal skin adjacent to the lesion. A difference in structure between normal skin and the skin cancer is demonstrated in the OCT image of the BCC showing a generally more disordered tissue. Furthermore, the main structures in the histology of the BCC are also seen in the OCT image. In a clinical setting the task is to differentiate between benign and malig-

---

[3] It should be mentioned that the identification of vessels was performed using structural OCT images and not D-OCT images.

nant lesions, this is much more challenging because benign lesions often show the same structure as malignant in the OCT images. Furthermore variations with age, skin type, anatomical site etc. must be taken into account [66, 70, 71]. Many studies have, however, reported high correlation between OCT images and histology, suggesting that OCT can be used to recognize NMSC lesions [72, 73, 74, 75]. An element of subjectivity was introduced in this evaluation because decisions were based on visual inspection of the OCT images. This was the case in most of the cited studies, although it has been suggested that machine learning tools may aid and improve the diagnostic accuracy of OCT. The potential of automatic feature extraction using non-parametric machine learning algorithms was demonstrated in a pilot study concerning the possibility to distinguish BCC (the most prevalent NMSC type) from actinic keratosis [76]. Another study including more than 100 patients aimed at distinguishing between sun-damaged skin, actinic keratosis and normal skin [77]. A horizontal edge detection technique was employed to measure the presence of layered structure in epidermis. The edge detection was automated and resulted in about 70% correct classification. The presence of dark band in epidermis evaluated by the naked eye gave a correct classification rate of about 85%. A pilot study used OCM with high lateral resolution for identifying BCC morphology with promising results even though larger studies are required to evaluate the diagnostic potential [78].

Functional OCT has also been suggested to improve the accuracy. The use of PS-OCT images has been investigated for NMSC [79]. The highly organized collagen fibers in dermis result in birefringence. In skin cancer lesions the ordered structure breaks down. Therefore it was suggested that distinguishing normal skin and BCC was possible using PS-OCT and this was confirmed by the two cases studied [79]. In addition to tissue changes caused by invasive growth, the neovascularisation of tumors is an important biological and morphological feature of malignancy. D-OCT is therefore another possible approach to the diagnosis of malignant lesions. Increased vascularity around skin tumors would be expected in case of malignancy. D-OCT data from clinical studies of skin tumors is not available at present. Diagnosis of skin cancer lesions has already been attempted by the use of laser Doppler imaging, but this method gives no depth resolution which could be important for determining the borders of the lesion [26]. Multiphoton imaging is an emerging method which may provide information about the chemical structure of tissues *in vivo* [80]. Multiphoton imaging has shown promising results in skin cancer diagnosis but the methods appear to be restricted by a limited penetration depth [80]. OCT and the multiphoton technique can be combined into unified system such that two types of images are acquired at the same time. One approach may therefore be to use the multiphoton image for determining if a lesion is benign or malignant and the OCT image for determining the thickness of the lesion. This requires that the OCT image carries information in the deeper region about the transition from tumor tissue to normal tissue. Using Raman spectroscopy the change in chemical composition between BCC and the surrounding normal skin can be detected with high accuracy [81]. But Raman spectroscopy does not provide depth resolved information like OCT and therefore delineation of tumor borders in depth is not possible.

1.3.2 Emerging applications in dermatology

The organized collagen structures in skin break down when exposed to high temperatures. Because the collagen structures can be detected using PS-OCT it is possible to measure the depth and extent of a burn which are crucial parameters when deciding if treatment is necessary. PS-OCT may also be used for monitoring of the healing process. A significant difference in birefringence between burns and unaffected skin has been reported [82, 83, 84]. The common skin disease psoriasis is challenging to treat and currently there exist no precise instruments for evaluating the treatment effect of psoriasis which is essential to improve the treatment possibilities. Employing OCT for monitoring changes during a treatment, guiding treatment and follow up has been attempted [85, 86].

1.4 Applications in biology and medicine

Besides the applications mentioned above, OCT has been applied in several other areas. In this section some of these will be described briefly with emphasis on cardiology, oncology and developmental biology. This is not a complete list of feasible applications but rather cases exemplifying the areas where OCT is applied or where the potential of OCT is currently being investigated.

The skin has an easy accessible surface that can be investigated using OCT. Moving to the inside of the body a number of so-called hollow organs, such as the cardiovascular system, gastrointestinal tract, bladder etc., also contains accessible surfaces which can be reached using an endoscope. On these epithelial surfaces, tools for detecting pre-cancerous changes are needed in order to perform early diagnostics. Therefore it is relevant to investigate if OCT is capable of detecting pre-cancerous lesions.

In general, a feasible application must take advantage of some of the unique properties of OCT, such as the relative large penetration combined with micrometer resolution, no need of physical contact to the sample, or the possibility of producing small probes for endoscopic applications. In cardiology, gastroenterology, gynecology, urology and respiratory medicine it is essential to use a small probe that can be integrated with an endoscope. In developmental biology, it is the micrometer resolution combined with millimeter penetration and non-invasiveness

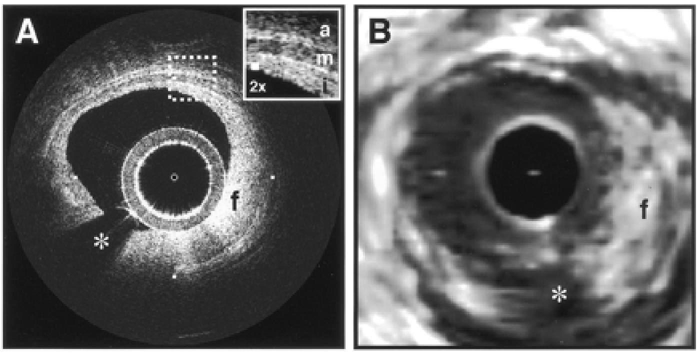

a) b)

Figure 1.11: Comparing fibrous coronary plaque imaged with OCT and ultrasound. a) OCT image b) Corresponding 30 MHz ultrasound image. i: intimia with intimial hyperplasia, m: media, a:adventitia, f: fibrous plaque, *: guidewire artifact. figure 2 from [88]. Printed with permission.

that makes OCT attractive. Moreover, the non-invasiveness makes progression over time possible which is of high value in many applications.

1.4.1 Cardiology - diagnostics and monitoring

Cardiologic diseases are the leading cause of death worldwide; for example according to the World Health Organization 16.7 million people died from cardiovascular diseases in 2003 corresponding to about 30 % of all deaths [87]. A vulnerable plaque in the arteries is the most prevalent condition leading to myocardial infarctions. Therefore, the ability to detect this type of plaque is important. Early diagnosis is essential for the prognosis and makes high resolution imaging of the cardiovascular system highly relevant. A vulnerable plaque is characterized by a 50 μm fibrous cap overlying a lipid pool. Previously, ultrasound imaging has been used to characterize plaque lesions, but the resolution is not sufficient to resolve the structures and make a reliable diagnosis [88, 89]. OCT provides a much higher resolution than ultrasound making more detailed characterization of the morphology possible [90, 91]. In figure 1.11, a comparison of fibrous coronary plaque imaged with OCT and ultrasound is shown (rotational scan). It is evident that OCT provides a much more detailed image with better delineation of layers than ultrasound. *Ex vivo* measurements demonstrated the ability to distinguish different plaque types [92, 93]. For fibrous plaque the sensitivity and specificity was 71-79 % and 97-98 % respectively [93]. For fibrocalcific plaque it was 95-96 % and 97 % and for lipid-rich plaque it was 90-94 % and 90-92 % [93]. *In vivo* characterization of plaque has also been reported and is currently an issue of intense research [94, 95]. It has also been investigated if the use of PS-OCT can assist further in identifying vulnerable plaque [96]. Due to loss of organized collagen in these lesions detectable with PS-OCT it might be possible to diagnose with even higher accuracy than by structural OCT alone.

In the treatment of coronary stenosis it is common to insert a stent to maintain the blood supply to the heart. Insertion of a stent in the right place is possible by OCT guidance as investigated by a number of studies [97, 98]. Unfortunately, the presence of a stent may result in growth of scar tissue leading to restenosis in some cases. Therefore it is necessary to monitor the patients after insertion. Detection of thin scar tissue layers has been demonstrated to be possible using OCT and with a higher sensitivity than ultrasound due to a much higher resolution [99, 100]. OCT is therefore a valuable follow up tool for deciding if and when to take action. Insertion of stents and follow up are commercial available and is an alternative to previously used intra vascular ultrasound imaging [101].

1.4.2 Oncology

Apart from OCT imaging of skin cancer, described in section 1.3.1, a number of other applications in oncology have been explored. This includes attempts to detect pre-cancerous changes in the esophagus, bladder, lung, breast and brain. Early detection of cancer is important to maximize the survival rate. Therefore it is relevant to investigate if non-invasive and high-resolution imaging with high diagnostic accuracy can be provided by OCT. Due to the limited penetration, OCT imaging of inner organs must be performed either during open surgery or via an endoscope. During surgery, OCT can potentially be used to guide and help the surgeon delineate tumor borders and guide surgery. Examination of the esophagus is performed for diagnosis of cancer and pre-cancer conditions. Usually the esophagus is visual inspected through an imaging endoscope, but the ability of detecting pre-cancerous changes is difficult. Excisional biopsies suffer from sampling errors and have a number of disadvantages when performed in the esophagus such as bleeding. High frequency endoscopic ultrasound has also been used for imaging esophagus but lack resolution to detect cancer with high accuracy [102]. The same holds for X-ray and magnetic resonance imaging. Because OCT provides a much higher resolution than the imaging techniques mentioned above, it is relevant to investigate whether OCT can improve the diagnostic accuracy and detect cancer at an earlier stage which is essential for the prognosis. Barrett's esophagus is a condition which can progress to cancer and once diagnosed a screening is performed regularly to monitor the development. Barrett's esophagus has been imaged with endoscopic ultrahigh resolution OCT and compared with histology [103]. A difference between normal esophagus versus Barrett's esophagus and esophageal cancer was reported, and it was concluded that OCT is capable of imaging the fine structures in esophageal tissue. Another study investigating this subject reported 78 % accuracy of detecting dysplasia in patients with Barrett's esophagus [104]. Bladder cancer is traditionally diagnosed using cystoscopy, i.e. visual inspection through an endoscope. This method gives information about the surface of the bladder and therefore diagnosis of sub-surface tumors are not possible. Detection of pre-cancerous changes is not possible either. OCT has been used to examine the bladder walls [105, 106]. In healthy bladder tissue the mucosa, submucosa and muscularis layers were visible in the OCT images, whereas break up of this structure in invasive carcinoma was reported. A study including 87 areas in 24 patients reported a sensitivity and specificity of 100 % and 89 %, respectively [107]. OCT has also been applied for imaging the bronchial airways [108, 109]. A high correlation between OCT images and histology was reported and the authors suggest a potential application in lung cancer diagnostics. Using OCT for breast cancer diagnosis has been suggested [110]. The problem of determining lymph node involvement in breast cancer has been investigated through an *ex vivo* study [111]. In this study, the OCT images was shown to correlate well with histopathology. Furthermore OCT can be used as monitoring tool to assess tumor margins during surgery of breast cancer [110]. In the treatment of prostate cancer by photodynamic therapy, D-OCT has been used for monitoring the treatment [112]. Recently, human kidneys have been examined *ex vivo* demonstrating that identification of histopathologic features was possible [113].

1.4.3 Developmental biology

Within developmental biology, OCT has been used to visualize many different developmental processes in many different small-animal models during more than a decade. It is not possible to cover all the applications here, but a recent rather detailed review of OCT in developmental biology can be found in [114]. OCT was introduced to developmental biology in 1997 by Boppart et al. [115]. One of the most promising and fascinating applications of OCT within developmental biology is related to the study of human heart development. The heart is the first organ to form and function in vertebrates and undergoes simultaneous structural and functional maturation as it transforms in a dynamic process from a straight tube to a four-chambered heart [116]. Malformations of the heart are among the most common birth defects, and are the leading cause of birth defect related deaths [117]. However, the cause of most heart defects still remains unknown. For the understanding of normal and abnormal heart development studied in different small animal models, there is a need for a real-time, non-invasive imaging tech-

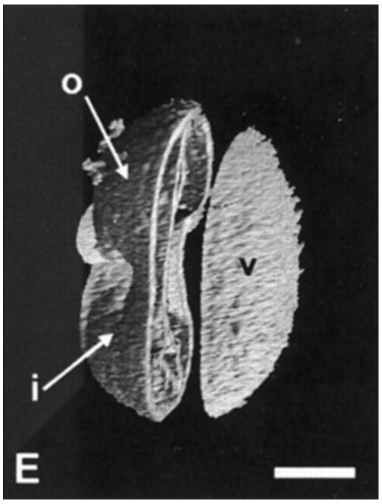

Figure 1.12: 3D OCT scan of a 56 hours old (HH-stage 15) chick embryo heart of an CNC-ablated embryo. Cutaway reveals further internal structural details. O indicates outflow limb; i, inflow limb; v, presumptive ventricle. Bar = 0.250 mm. figure 2E from [118]. Printed with permission.

nique with micrometer resolution and millimeter penetration depth. It has turned out that OCT is well suited for anatomical and functional imaging of the developing cardiovascular system, as it has been demonstrated by various groups in recent years for different species [114, 118, 119, 120, 121, 27]. As an example, figure 1.12 shows a 3D OCT scan of a 56 hours old (HH-stage 15) chick embryo heart of an CNC-ablated embryo [118]. Among the most recent studies in this field is the investigation of one of the most critical but poorly understood processes during cardiovascular development: the establishment of a functioning coronary artery (CA) system. By using OCT, the first *in vivo* recordings of developing CAs in chick embryo hearts have been obtained [122]. Again, this demonstrates the use and strength of OCT to help understanding the complex processes studied in developmental biology.

1.5 Summary

In conclusion OCT is a non-invasive optical imaging technique providing real-time video rate micrometer resolution images with millimeter penetration thereby filling in the gap between ultrasound and confocal microscopy. Moreover functional extensions are possible enabling flow detection (D-OCT), birefringence detection (PS-OCT) and extraction of spectroscopic in-formation (spectroscopic

OCT). The technical development reveals faster systems, higher resolution and better image quality. Regarding the applications of OCT, the technique is already accepted as a clinical standard in ophthalmology and has proven invaluable in diagnostics and treatment control of many eye diseases. The majority of OCT systems used in the clinic today are relatively slow compared to state of the art research OCT systems although faster FD-OCT systems currently are emerging in the clinic. It is therefore expected that the advantages of higher speed has not been completely revealed yet. Furthermore the OCT systems used in the clinic are without functional OCT extensions. Preliminary research results show a remarkable improvement in diagnostic information by using higher resolution, faster data acquisition (3D data) and functional OCT. Therefore it is expected that major improvements in diagnostics are feasible in the coming decade of OCT as a commercial instrument. For skin cancer diagnostics OCT possess many useful features, it has been studied clinically although convincing studies reporting high-accuracy diagnosis are sparse. It seems that a different approach is needed to make it a diagnostic tool in the clinic. Cellular resolution would make it possible to see how the cells are ar-ranged in the skin which is the parameter used for diagnosis by histology. Also confocal microscopy studies reported diagnostic accuracy higher than 95 % [123]. Therefore a much higher resolution is probably required to make OCT a strong imaging modality for skin cancer diagnostics. This requires either broader band-width light sources (better depth resolution) or tighter focus (better transverse resolution). The latter is conveniently implemented in an en face mode like confocal microscopy (OCM). In this context it is important to emphasize that the depth and transverse resolution is degraded with depth in highly scattering tissue. If high-resolution images are necessary to make an accurate diagnosis, it is probably only possible to generate useful images for diagnostics to a depth less than the 1-2 mm penetration depth. In cardiology there is a need for detection of vulnerable plaques and OCT has already shown promising results. Within oncology a wide variety of lesions has been examined including esophagus, bladder, lung, breast and brain with promising results. Finally, in developmental biology OCT has proved its value by providing *in vivo* micrometer resolution images that help understanding the complex processes studied in this field.

Chapter 2

Skin cancer diagnostics

Diagnostics of skin diseases and development of OCT systems suited for this purpose is the main subject of this thesis. A general introduction to dermatological applications including skin cancer was outlined in section 1.3.1. In order to evaluate the diagnostic value of optical coherence tomography, a clinical protocol involving 100 patients with skin cancer has been performed and the results are presented in paper **IV**. Besides this major study, a few smaller clinical studies have been performed and are presented in paper **I-III**. The intention of this chapter is to supply a description of the system used for the clinical measurements and summarize the main conclusions of these measurements.

2.1 OCT system

In figure 2.1 a sketch of the time domain OCT system is shown. A commercial super luminescent diode with a full width half maximum (FWHM) bandwidth of 66 nm around 1300 nm and a power of about 20 mW is employed. In the reference arm, the delay length is modulated by a scanner consisting of a grating, a lens, a scanning mirror and a stationary mirror [124]. The working principle of the scanner is explained in more detail in chapter 3 because a similar scanner is also used for the high resolution system. The A-scan rate is determined by the scanning mirror rate (galvano scanner) which is 120 Hz. Therefore a cross sectional image is typically acquired in a few seconds. Following detection, the signal is amplified ($\sim$ 30 dB) and filtered to remove low frequency noise (30 kHz high pass). The analog signal is digitized and the envelope is calculated on a FPGA board (field programmable gate array) by applying a Hilbert transform. Finally, the image data is transferred to a computer using an analog frame grabber. In figure 2.2a the spectrum of the light source is shown. A near gaussian spectrum corresponding to a resolution of about 8 μm (in tissue) and a power of more than 20 mW. In figure

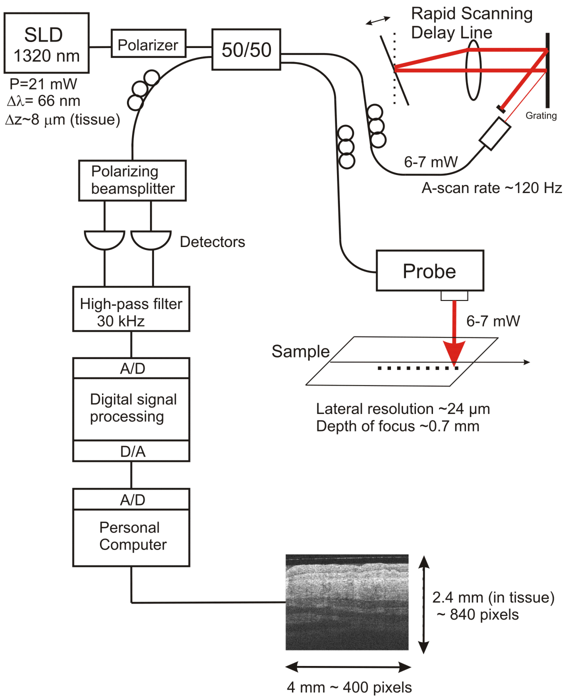

Figure 2.1: Sketch of the time domain OCT system primary used for clinical measurements

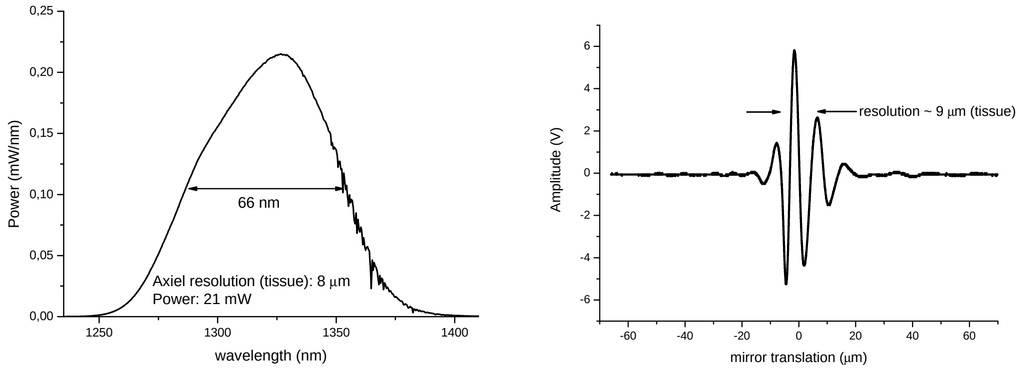

a) b)

Figure 2.2: a) the power spectrum of the light source b) an interferogram obtained with a mirror in the sample arm confirming near-theoretically resolution

2.2b an interferogram is shown confirming an actual resolution close to the theoretically value. The transverse resolution is per definition equal to the spot size of the beam, in this case approximately 24 μm. The relative crude transverse resolution was chosen to obtain a high imaging depth which is important for delineation of tumors in depth.

In a clinical environment, twisting of the sample fiber is unavoidable and the effect is a change in the polarization state of the back reflected light from the sample arm. This affects the amplitude of the interferometric signal and must therefore be overcome in order to acquire useful data independent of the actual fiber movement. In order to avoid this effect, we have used quadrature detection involving two detectors and polarizing optics as shown in figure 2.1[4]. A polarizer was inserted between the source and interferometer to linearly polarize light. At the exit of the interferometer, a polarizing beamsplitter is inserted and dual detection of the two orthogonal polarization states are employed. In front of the polarizing beam splitter, a polarization controller is used to split the intensity of the light from the reference arm equally between the two polarization channels. By using this setup, we obtain an OCT signal virtually insensitive to polarization changes. This is tested by changing the polarization of the reflected sample arm light using a polarization controller while observing the change in signal strength. Less than a 3% change was observed experimentally. The drawback of this arrangement is an effective reduction in power from the source with about 25% (especially due to the polarizer). This does not affect the sensitivity significantly (about 1-2 dB) and therefore the maximum imaging depth was not affected noticeable either, whereas the detection scheme is of great benefit in the clinic.

The dual detection scheme described above makes a simple kind of PS-OCT possible. According to Hee et al, the phase retardation may be calculated as [32]

$$\phi(z) = \arctan(I_1/I_2) = k_0 z \Delta n \tag{2.1.1}$$

where I_1 and I_2 denotes the intensities measured by the two detectors, k_0 the wave number, z the depth and Δn the difference in refractive index between the two directions of the sample. Eqn. (2.1.1) assumes that the sample is illuminated with circular polarized light. In that case the phase retardation is independent of the sample orientation. In a free space system, it is simple to control the polarization state, whereas in a fiber based system the polarization state is affected by fiber twisting unavoidable in a clinical situation. This means that our simple implementation is not suitable for measuring absolute values of phase retardation. Having these limitations in mind, a simple detection of birefringence is in most cases possible. The only exception is when the sample is illuminated by a linear polarization state parallel to one the optic axes of the sample. In a clinical setting, however, each patient is usually imaged with slightly different positions of the probe and therefore biological birefringence is usually detected in at least one

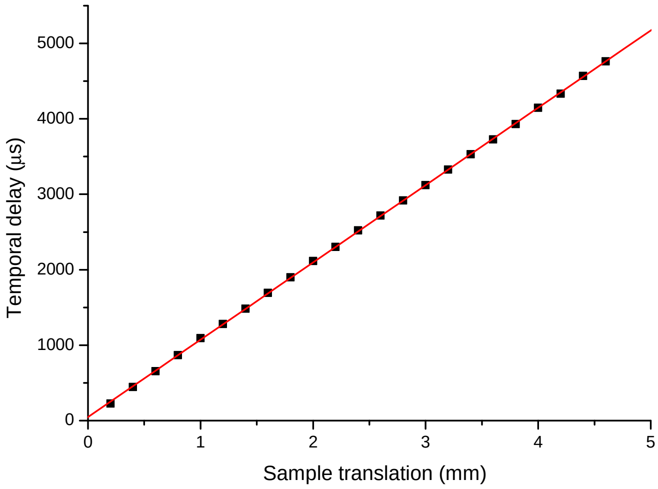

Figure 2.3: The reference scanner exhibits a linear relation between translational and temporal delay which is important for constant pixel spacing

of the measurements. Notice also that the polarization sensitive image is just a simple manipulation of the acquired detector signals. Therefore the OCT and PS-OCT data are acquired simultaneously. A more reliable polarization sensitive detection scheme requires signal processing of 4 images acquired with the sample illuminated with different polarization states [33].

In figure 2.3 the correspondence between the translation of a mirror in the sample arm and the temporal signal measured by the detector is shown. A linear relation is demonstrated which is important for maintaining constant sampling spacing. Furthermore it is important to have a constant reflection from the reference arm, such that a change in interferometric signal strength is only due to a change in amount of light reflected from the sample. By careful adjustment of the reference scanner, the intensity modulation during scanning could be reduced to about 4-5%. In figure 2.4 a photo of the mobile system and the hand-held probe is shown. The probe is completely closed in order to make cleaning and disinfection possible. To avoid a major reflection from the discontinuity between the glass plate and skin, ultrasound gel was applied to skin before imaging. Thereby the air gap between skin and glass plate is filled out with material and only minor changes in the index of refraction is experienced, resulting in a continuous signal behavior around the discontinuity. The probe also contains a video camera which can be used for finding the right position on the skin.

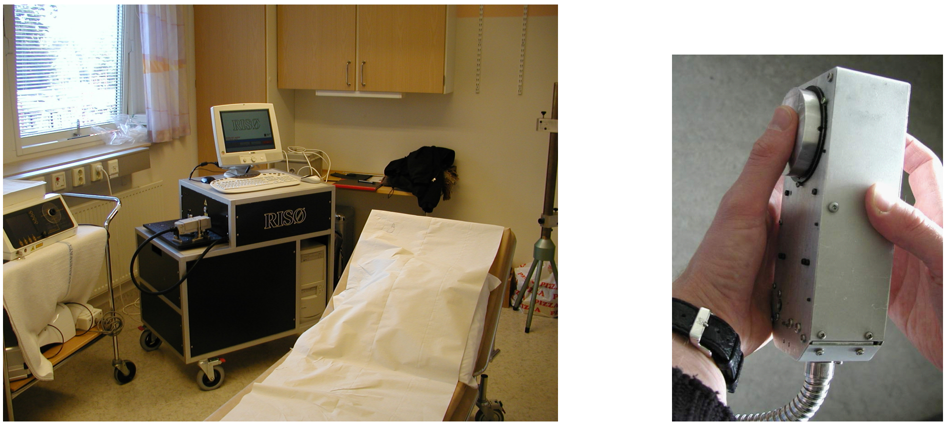

a) b)

Figure 2.4: a) the OCT system in the clinic b) the hand held probe

2.2 Review of clinical measurements

The system described in the previous section was used for the studies presented in paper **I-IV**. In paper **I** it was shown that OCT is capable of detecting the tropical disease where the larva migrans invades the outer layers of the skin. The larva digs small tunnels of less than 0.5 mm and these could be visualized in one out of three patients. In comparison, 20 MHz ultrasound was not capable of visualizing the tunnel, which is justified by the much lower resolution. Paper **II** identifies features of the human finger nail in OCT images and compares ultrasound and OCT for measuring nail thicknesses. A correlation between thicknesses measured by OCT and ultrasound is demonstrated. Furthermore, OCT is shown to have a higher reproducibility. Measuring thicknesses of skin cancer lesions is explored in paper **III**. OCT was found to be more precise compared to 20 MHz ultrasound. Finally, the diagnostic study including 104 patients is presented in paper **IV**. Distinguishing between normal skin and skin cancer lesions is possible using specific OCT features and a sensitivity of 79% to 94% and specificity of 85% to 96% was estimated. However, differentiation between benign and malignant lesions is not possible suggesting further improvements of the technique like for example higher resolution.

Chapter 3

Improvement of depth resolution

Even though OCT provides images with a resolution competitive or even better than most imaging systems, cellular resolution is not achieved routinely. High resolution and the possibility of imaging single cells is relevant for diagnostic and biologic purposes, for example the previous chapter motivated an increase in resolution for skin cancer diagnostics. An improvement of the resolution has therefore been attempted since OCT was introduced [2, 3, 4, 38]. In this chapter an OCT system designed for improved depth resolution at a center wavelength of 1300 nm is presented. The design aims for a resolution of about 2 μm approaching single cell visualization capabilities. Such a resolution corresponds to an optical bandwidth of 250 nm making use of high bandwidth optical components mandatory. Imaging speed has not been the concern, but rather to obtain a high depth resolution and demonstrate the possible advantages for skin cancer diagnostics. In addition to the system itself, a broad band light source is also required to perform high resolution imaging. These sources are developed through an European project as 'turn key' sources providing sufficient power and low noise [125]. The first experiments with prototype sources from this project are presented in section 3.5. Furthermore, a collaboration with a Danish company developing light sources was established and the results of this work is presented in section 3.4.

3.1 Design of high resolution OCT system

The high resolution implementation was performed in time domain because the imaging speed was not of primary concern. High depth resolution imaging requires the use of high bandwidth light sources and corresponding optical components supporting the bandwidth. Especially, the following issues are important to consider:

- Optical fibers are preferable single mode in the entire optical spectrum used.

design wavelength	1300 nm
single mode operation	above 1150 nm
mode field diameter	4.8 μm
numerical aperture	0.2
insertion loss (BS, CIR)	3.7 dB
return loss (CIR)	40 dB

Table 3.1: Specifications of the custom made fiber, beam splitter and circulator (BS: beam splitter, CIR: circulator).

- Beam splitter is homogenous, i.e. with a constant splitting ratio independent of the wavelength.
- Optics for collimation and focusing in the sample arm is suitable for high bandwidth operation.
- Reference scanner supports the spectrum of the light source, i.e. the source spectrum is not distorted by passing through the scanner.

Using a multi mode optical fiber (or equivalently a single mode fiber with too high cut off wavelength) results in an non-perfect overlap of light at the detector and therefore in a reduced amplitude of the interferogram, i.e. a reduction in signal to noise ratio [2]. Furthermore, light traveling in different modes arrives at slightly different times at the detector. This effectively introduces a smeared out interferogram corresponding to loss of depth resolution. If the beam splitter is not homogenous, a distorted interferogram with a possible loss of depth resolution is the result [2]. A standard 1300 nm single mode fiber is typically single mode above about 1250 nm which is not sufficient considering a light source with a bandwidth of more than 200 nm. Standard beam splitters and circulators are also quite narrow band for this purpose. Therefore custom made components were ordered from a Canadian firm[1]. In table 3.1 the specifications of the fibers, beam splitter and circulators are shown. According to these specifications, single mode operation is maintained for a spectrum of about 250-300 nm around 1300 nm. The 50-50 beam splitter is also designed for a similar bandwidth with an insertion loss of about 3.7 dB comparable to standard components. Initially, a circulator supporting the full bandwidth was not available and instead we used two beam splitters. Later on, a custom made circulator was available thereby improving the actual power used by a factor of two. In terms of sensitivity this corresponds to an improvement of approximately 3 dB according to eqn. (1.1.7). In figure 3.1 a sketch of the system with the circulator configuration is shown. In the relevant

---

[1] Fiber Optic Network Technology

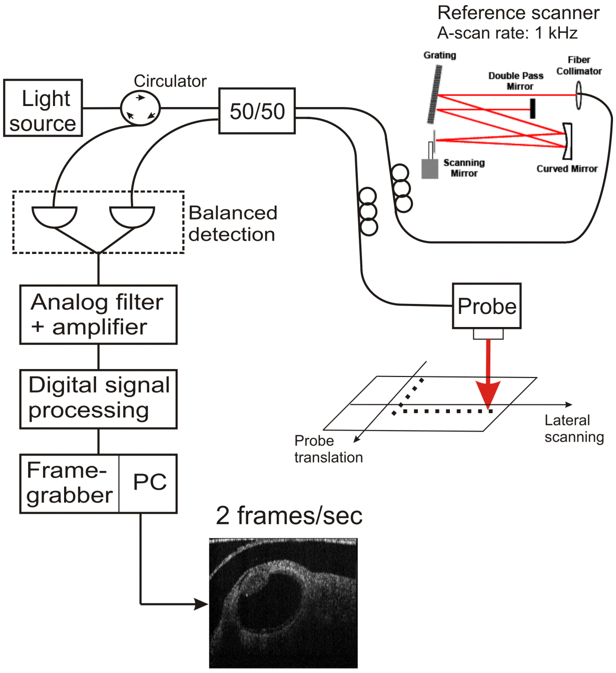

Figure 3.1: Schematics of the high resolution OCT system.

sections below it is pointed out whether the 'two-beam-splitter solution' or the circulator was used. The interference signal is detected using a balanced photo detector to suppress intensity noise from the source. For optimizing the balanced detection the two signal paths to the detector have equal lengths. The interference signal is centered at 3 MHz with a bandwidth of 2.5 MHz (240 nm broad source). Following photo detection, the signal is band pass filtered and amplified. The interferogram is digitized and converted to an analytic signal by passing it through a digital filter, which eliminates the negative frequency components. The envelope is calculated as the modulus of the analytic signal. The lateral scan is generated by an external saw-tooth generator. Data are transferred to a computer via a frame grabber and the image is finally displayed on the screen. Data acquisition is controlled by a Labview program (National Instruments). The collimating and focusing optics were chosen for high bandwidth operation (achromatic lenses) and such that a spot size of about 10 μm was obtained. An improved transverse resolution is easily obtained by focusing to a smaller spot size. However, since we do not use dynamic focusing, this would result in a transverse resolution strongly varying with depth. Moreover, the maximum imaging depth would decrease. Finally, the spectrum reflected from the reference scanner has to be nearly identical with the source spectrum. Otherwise a loss of depth resolution is unavoidable. This is in general the most critical point in the design of the system and can be serious limiting. The reference scanner made for this particular system, supports about 250 nm (FWHM) bandwidth and operates at 1 kHz. A more detailed description of the reference scanner and the operating principle is found in the following section including a discussion of the trade-offs between scanning speed, effective delay length and bandwidth support.

3.2 The reference scanner

There has been a number of implementations of the reference arm in a TD-OCT system [5]. The simplest solution is a mirror moving back and forth which is highly limiting regarding scanning speed. Fiber stretching by piezo electric elements have been demonstrated but requires long fiber lengths to provide a sufficient scan length thereby introducing unwanted dispersion. Retro reflectors mounted on a galvano scanner have been used but with modest scan speed. A grating based reference scanner as used in our system has advantages of high speed, high scan length and dispersion compensation possibilities [124]. Dispersion is for example introduced if the fiber lengths in reference and sample arm are different or due to the focusing lenses in the sample arm. By displacing the diffraction grating relative to the lens, the dispersion can be compensated. Furthermore, the center frequency can be adjusted independent of the scan length. The drawback is a complex construction with a high power loss. The design of the reference scanner aimed for the following specifications

- Central wavelength at 1300 nm
- Bandwidth support of 240 nm (about 2 μm resolution in tissue)
- Scan length of about 2 mm in tissue (refractive index is assumed to be 1.4)
- Scanning speed as fast as possible with the requirements above fulfilled

3.2.1 The principle of the reference scanner

A sketch of the scanner is shown in figure 3.2b. The principle for generating a path length modulation is the same as for the scanner shown in figure 3.2a, the only difference is the replacement of the lens with a curved mirror. The motivation for using reflective components only, is a reduction in dispersion mismatch between sample and reference arm [128]. Referring to figure 3.2b, light entering the scanner is dispersed using a diffraction grating. The curved mirror is placed at a distance from the grating equal to the focal length of the mirror. Therefore the

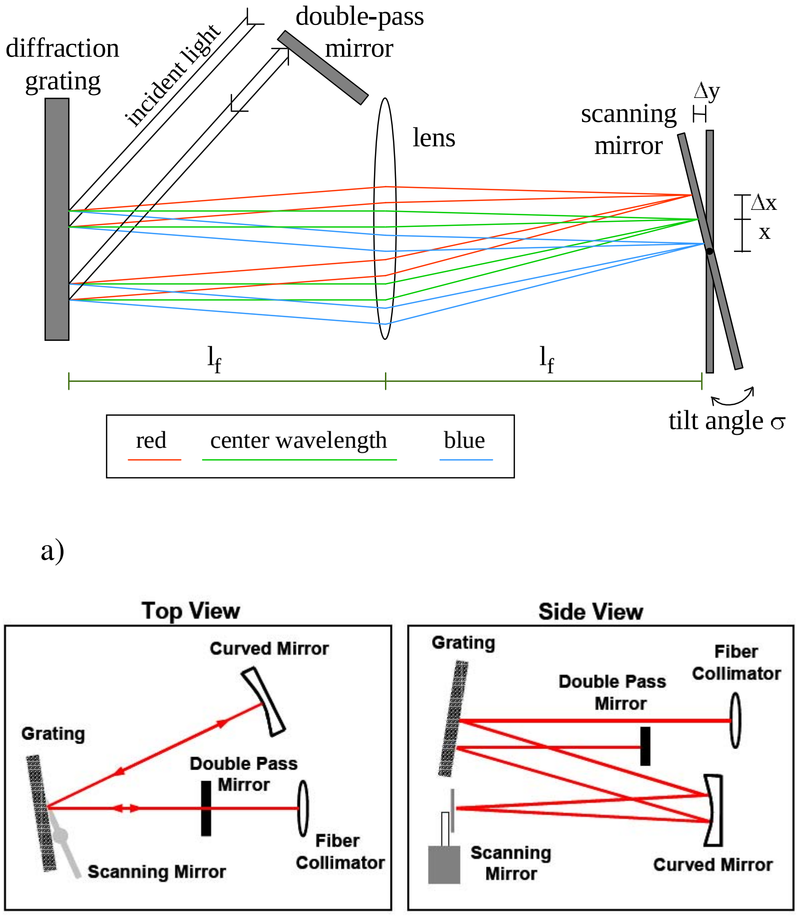

a)

b)

Figure 3.2: Sketch of the reference scanner. a) scanner using a lens. Figure 1 from [127] b) equivalent scanner using a curved mirror. Figure 2 from [128]. Printed with permission.

diverging spectrum is collimated toward the scanning mirror. Every position of the scanning mirror corresponds to a different path length through the scanner and in this way a scan of the mirror corresponds to a path length modulation. More formally, the path length difference through the scanner Δl_ϕ between a wavelength λ and the center wavelength λ_0 may be derived with reference to figure 3.2a

$$\Delta l_\phi(\lambda) = 4\sigma x + \frac{4\sigma f(\lambda - \lambda_0)}{p} \tag{3.2.1}$$

where σ is the angle of the tilting mirror, x is the offset of the center wavelength on the scanning mirror, f is the focal length of curved mirror and p is the pitch of the diffraction grating. To derive eqn. (3.2.1) the grating equation was used and the paraxial approximation employed ($\sin\theta \approx \theta$). The corresponding phase shift is the path length difference multiplied by $2\pi/\lambda$. Using eqn. (3.2.1), the group path length difference is found by differentiating the phase shift with respect to angular frequency ω ($\omega = 2\pi c/\lambda$) and multiplying by c

$$\Delta l = 4\sigma x - \frac{4\sigma f \lambda_0}{p} \tag{3.2.2}$$

The group path length difference Δl in eqn. (3.2.2) is equal to the scan length generated by the reference scanner and is directly proportional to the scanning mirror angle σ. By differentiating eqn. (3.2.1) with respect to time and evaluating at $\lambda = \lambda_0$ the phase velocity is obtained. One cycle of interferometric signal is equal to the center wavelength λ_0 and therefore dividing by λ_0 the center frequency is obtained ($\lambda_0 f_0 = v$)

$$f_0 = \frac{4x}{\lambda_0}\frac{\partial\sigma}{\partial t} \tag{3.2.3}$$

The carrier frequency in eqn. (3.2.3) can also be found by calculating the Doppler shift applied by the scanning mirror. The interferogram contains a continuum of wavelengths each Doppler shifted by a different amount $\lambda v/c$ where v is the velocity of the scanning mirror. Therefore the interferometric signal contains a continuum of frequencies given by $\Delta\nu v/c = \Delta\lambda v/\lambda_0^2$. Using eqn. (3.2.2) this bandwidth is expressed as

$$\Delta f = \frac{2\Delta\lambda}{\lambda_0^2}\left(2x - \frac{2f\lambda_0}{p}\right)\frac{\partial\sigma}{\partial t} \tag{3.2.4}$$

In the design phase, eqn. (3.2.3) is used to determine the mirror offset x given the center frequency of the signal. In this way the center frequency can be tailored for detection electronics and in particular 1/f noise can be suppressed. The scan length is determined from eqn. (3.2.2). In this context it is pointed out that the

mirror frequency	1 kHz
curved mirror focal length	50 mm
grating pitch	1/150 mm
effective delay (tissue)	2.1 mm
optical bandwidth support	240 nm
center frequency	3 Mhz
bandwidth of interferometric signal	2.5 Mhz

Table 3.2: Reference scanner key parameters

effective scan length when using a sinusoidal driven resonance scanner is only about 2/3 of this value. Finally the bandwidth must be calculated to tailor filters and detection schemes using eqn. (3.2.4). The degrees of freedom is the scanning mirror angle amplitude, scanning mirror frequency (in practice mirror size is affected by speed), the focal length f of the curved mirror and the pitch p of the grating.

3.2.2 Design parameters

As mentioned, there is a trade-off between scanning speed, scan length and bandwidth support. For example increasing the optical bandwidth increases the minimum scanning mirror size and therefore the speed. This can partly be compensated by choosing a grating with a smaller pitch, but then the scan length is affected. In table 3.2 the chosen design parameters and corresponding specifications for the reference scanner is listed. The reference mirror is driven by a 1 kHz resonance scanner allowing 1000 A-scans per second. The optical parts were assembled using a commercial rod system together with home-made solutions. A photo of the final scanner is shown in figure 3.3.

3.3 System test and characterization

The high resolution system was initially tested and aligned using a commercial light source with a bandwidth of about 65 nm and a power of 25 mW (Inphenix super luminescent diode). These tests were performed using Corning SMF28 fiber and a standard 1300 nm circulator and beam splitter.

Data acquisition is performed with an equal time spacing between successive points. To ensure that the physical distance between successive points are the same along an A-scan, the reference scanner has to exhibit a linear relation between time delay and physical distance. The resonance scanner is driven by a

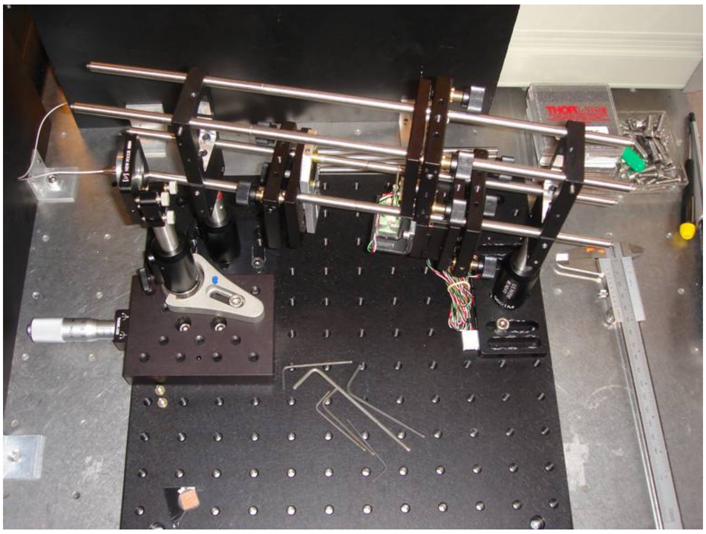

Figure 3.3: The reference scanner

sinusoidal voltage and to accomplish linearity, only 2/3 of the actual scan is used for data acquisition. This property was tested by translating a mirror in the sample arm and observing the corresponding time delay. In figure 3.4 the sample translation versus time delay is shown and demonstrates a linear relation. The effective delay is 2 mm in tissue corresponding to 2/3 of the sine oscillation of the reference mirror. This is a reasonable value because in highly scattering tissue like skin, the penetration is typically 1-2 mm. In most cases it was possible to adjust the reference scanner to accomplish the right center frequency while limiting the modulation to about 20%. The modulation is here defined as the intensity modulation of the reflected light from the reference arm during a scan cycle. Because the OCT signal is proportional to the electric field amplitude, the modulation of the OCT signal is only about 10 %. In figure 3.5 an interferogram recorded with a mirror in the reference arm is shown together with an OCT image acquired on human skin. The expected resolution with the commercial source is calculated using eqn. (1.1.4) to about 10 μm. The measured width of the interferogram is about 13 μm and this is a verification that dispersion compensation is possible with a 65 nm band width source. The sensitivity was also measured using the standard fiber components. With a mirror in the sample arm, the beam was attenuated using optical density filters until the OCT signal (after filtering and envelope detection) was not visible any more due to noise. A value of 102 dB (+/- 2 dB) was obtained, which is reasonable compared to most other time domain systems operating at the same speed.

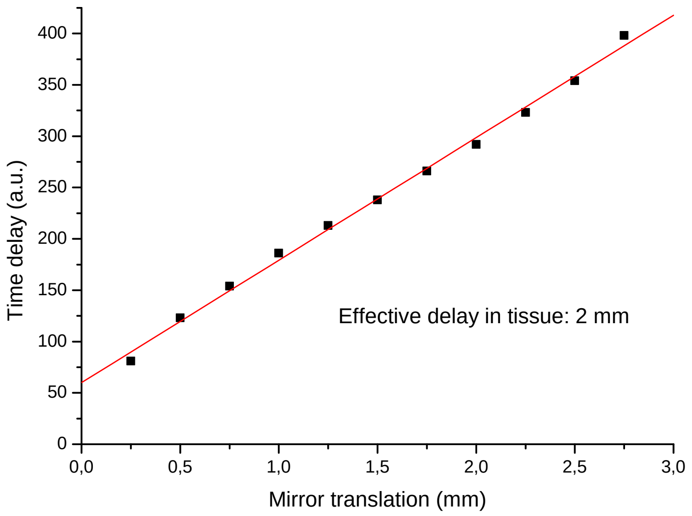

Figure 3.4: The dependency between time delay and physical distance was tested for the broad band reference scanner and demonstrated a linear relation.

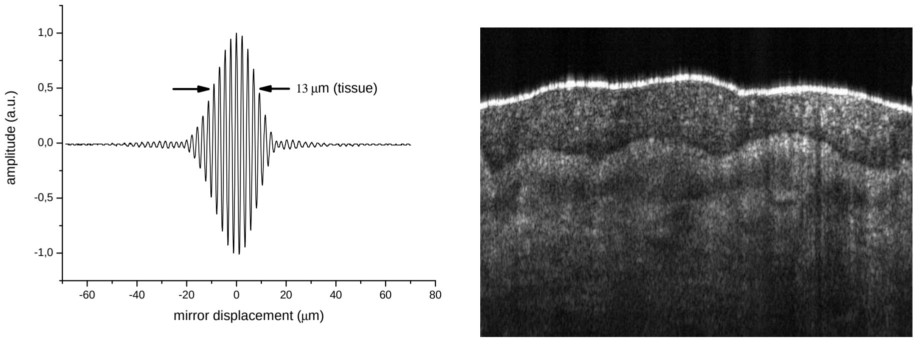

a) b)

Figure 3.5: a) An interferogram obtained with a commercial light source b) OCT image of the human skin, width: 2.1 mm, height: 1.5 mm.

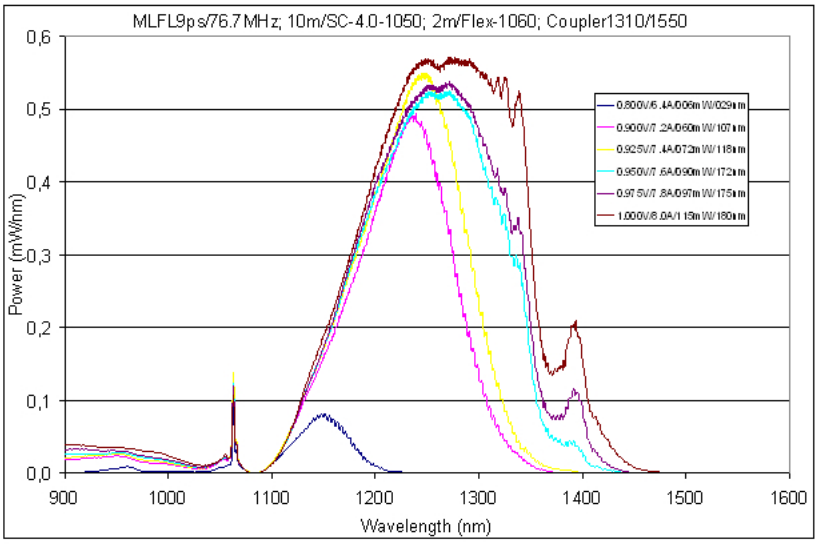

Figure 3.6: The spectrum from the light source for different pump power.

3.4 Tests with supercontinuum light sources

In a collaboration with a Danish company, two attempts were made to demonstrate high resolution OCT with light sources under development provided by this company. In this section the experiments using these sources and the results are described. At this stage, only the two-beam splitter solution was available. Unfortunately the excess loss of the custom made splitters were about 50% in the first experiments. With this in mind, the first experiments are primarily a test of the reference scanner performance and a test of suitability of the light sources for OCT imaging. Later an improved version of the beam splitters were received and used for the second part.

3.4.1 Pico-second pumped PCF

The light source setup consist of a pump laser broadened in a PCF also known as super continuum generation. The pump is a fiber laser delivering pulses of a few pico-seconds at a wavelength of 1064 nm with a repetition rate of about 75 Mhz. Before entering the PCF, light is optical amplified to reach a power sufficient to explore the non-linear effects of the PCF and broaden the optical spectrum. In figure 3.6 the spectrum is shown for different pump power. The spectrum is near Gaussian with a bandwidth of 140-180 nm (FWHM) and a power as much as 120 mW. The minor peak at 1060 nm is residual light from the pump and is not expected to cause any problems because of the much lower power level compared to the 1300 nm region. Even though the custom made fiber parts had a very high loss we did test the broad bandwidth behavior to make sure that the band width support was satisfactory. In figure 3.7a the transmission spectrum of the beam splitter is compared with the unshaped super continuum light spectrum. It is apparent, that the beam splitter is not limiting the bandwidth. In figure 3.7b the source spectrum is compared to the spectrum transmitted through the two arms of the beam splitter. A small discrepancy between the light reflected from the two arms and the spectrum of the source is seen. It is very likely, that the source spectrum has changed between the measurements due to the setup and therefore it should not be interpreted as a distortion of the spectrum by the beam splitter. In figure 3.8 the light source spectrum is compared to the spectrum after transmission through the beam splitter and reference scanner. Any bandwidth limitations introduced by the reference scanner is not observed and therefore a bandwidth of at least 150 nm (FWHM) is supported. In figure 3.9 an interferogram acquired with a mirror in the sample arm is shown. This is to illustrate the limited signal to noise ratio even for a large sample reflection. The interferogram can be compared to the one in figure 3.5 obtained with a commercial source.

3.4.2 Continuous wave pumped PCF

The second setup is based on a continuous wave Ytterbium laser delivering about 10 W at 1060 nm. Light from the laser is used to pump a 150 m PCF generating a super continuum around 1300 nm. Typically a bandwidth (FWHM) of 140-180 nm is obtained with a power of 100-200 mW dependent on the PCF coupling efficiency. We suspected the origin of the noise described in the previous experiments to be the pump laser and the optical amplification resulting in intensity noise of the super continuum at a frequency near the OCT signal. Therefore it was quite interesting to test a light source using a different pump laser and without optical amplifiers. Unfortunately the result was not any better than with the previous light source. Therefore an investigation of the intensity noise imposed on the spectrum was initiated. This can be investigated using a fast (photodiode) detector, an AC isolator and an electrical spectrum analyzer. For a commercial source the intensity noise is in the range of 130-140 dB/Hz whereas this prototype source has a value of 90-100 dB/Hz only. In other words, the intensity noise is about 4 orders of magnitude higher than for a commercial source. It is quite complicated to relate the intensity noise directly to the OCT signal-to-noise-ratio. Therefore it is difficult to judge whether the intensity noise is the main reason for a non-sufficient signal to noise ratio. In principle the intensity noise is canceled out when balanced detection is used if the power illuminating the two detectors are the same. Using the two-beamsplitter solution, this is definitely not the case

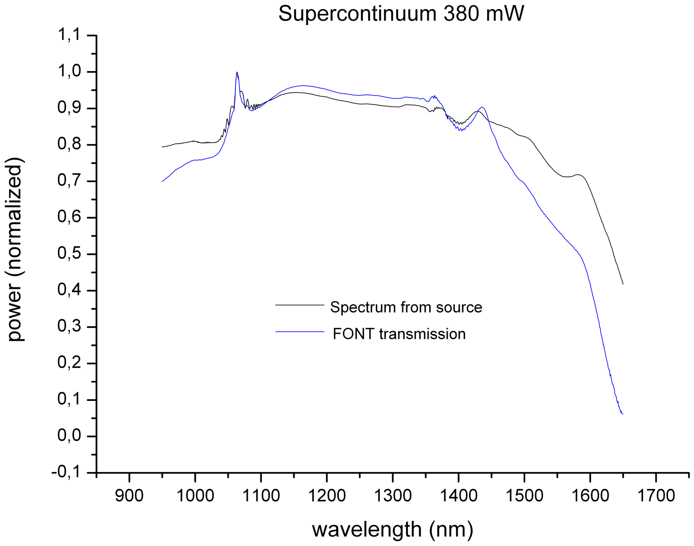

a)

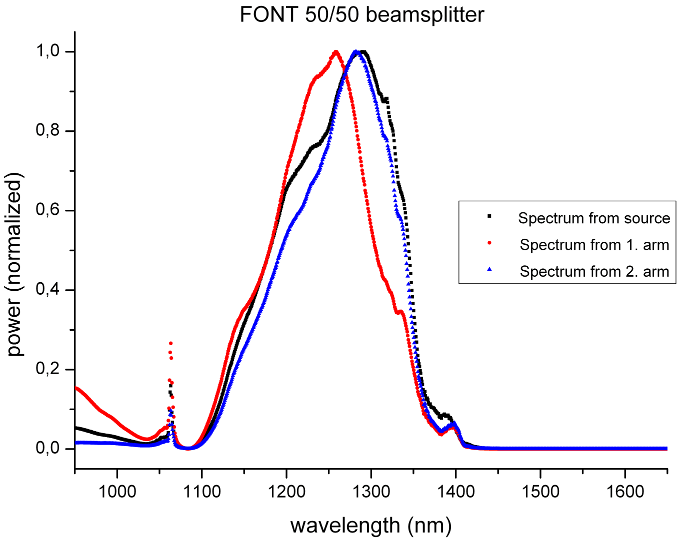

b)

Figure 3.7: Transmission characteristics of the custom made beam splitter. a) with unshaped spectrum b) with shaped spectrum.

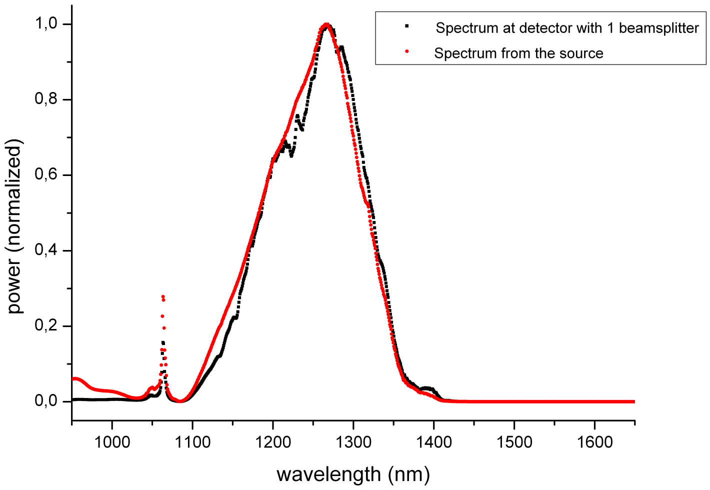

Figure 3.8: The reference scanner band width support characteristics.

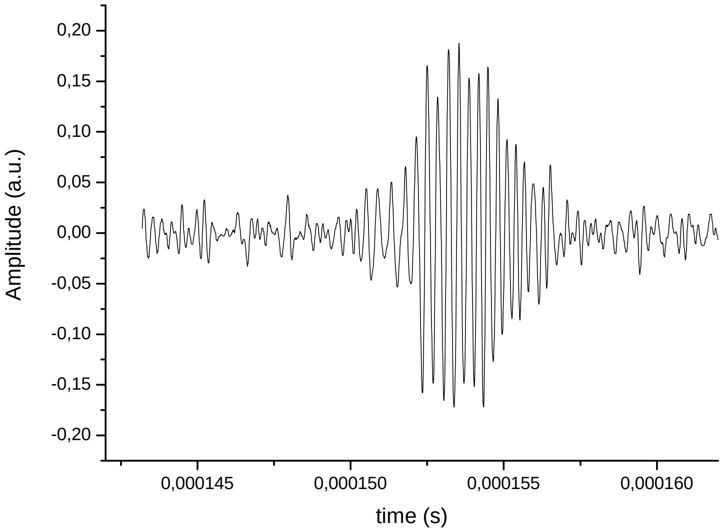

Figure 3.9: Interferogram obtained with a mirror in the reference arm. The time-distance calibration was not done, this is rather an illustration of the limited signal to noise ratio.

and this could be one reason for the non-sufficient noise suppression. Balancing of the power at the two detectors using attenuators did not solve the problem. A precise balancing is probably needed because of the pronounced noise level of source. Furthermore, if the beam splitter is not completely homogenous and the intensity noise is relatively strong, it is not possible to cancel the intensity noise completely. A custom made bulk optic beam splitter circumventing this problem has been reported by another group [38]. This splitting ratio of this custom made beam splitter has been measured to be 0.5 +/-0.03 within the entire spectrum used. The homogeneity of the custom made beam splitter was not investigated, but this could be an issue for the future. Due to the two-beam-splitter configuration the light source also receives feedback from the interferometer and could give rise to instability in spectrum and lead to noise. It is therefore possible that the intensity noise in reality is much higher than the measured values, because when measuring the intensity noise, the source only experiences a very small feedback. This could be the reason that imaging using these light sources was not possible.

3.5 Tests with semiconductor diode sources

The sources described in this section are developed in an European project known as NANO UB-SOURCES (nano ultra broad band sources) and is based on a quantum dot structure [125]. Compared to the super continuum sources described in the previous section, these sources are characterized by very low intensity noise level [126]. Measurements show an intensity noise less than 130 dB/Hz which is better than most commercial sources and much better than the super continuum sources described in the last section. For these initial tests, only the naked diodes were available in 3 different versions (M3339, VN590, VN1045). Therefore the first task was concerned about mounting, current supply connection, temperature stabilization and fiber coupling of the emitted light. Finally, the fiber coupled light was used for OCT imaging together with the broadband OCT system.

3.5.1 Fiber coupling of diodes

The diodes were placed in a mount including a peltier element for temperature stabilization. The mount is shown in figure 3.10c. Current and temperature control was performed using Newport commercial controllers. The emitted light was collected using a high numerical aperture lens as shown in figure 3.10a. Because the dimensions of the diode are different in vertical and horizontal planes, the collimated beam is elliptical. This is corrected by using two cylindrical lenses operating on just one dimension of the beam (an expanding telescope). Finally the beam is focused to a spot size corresponding to the mode field diameter of the

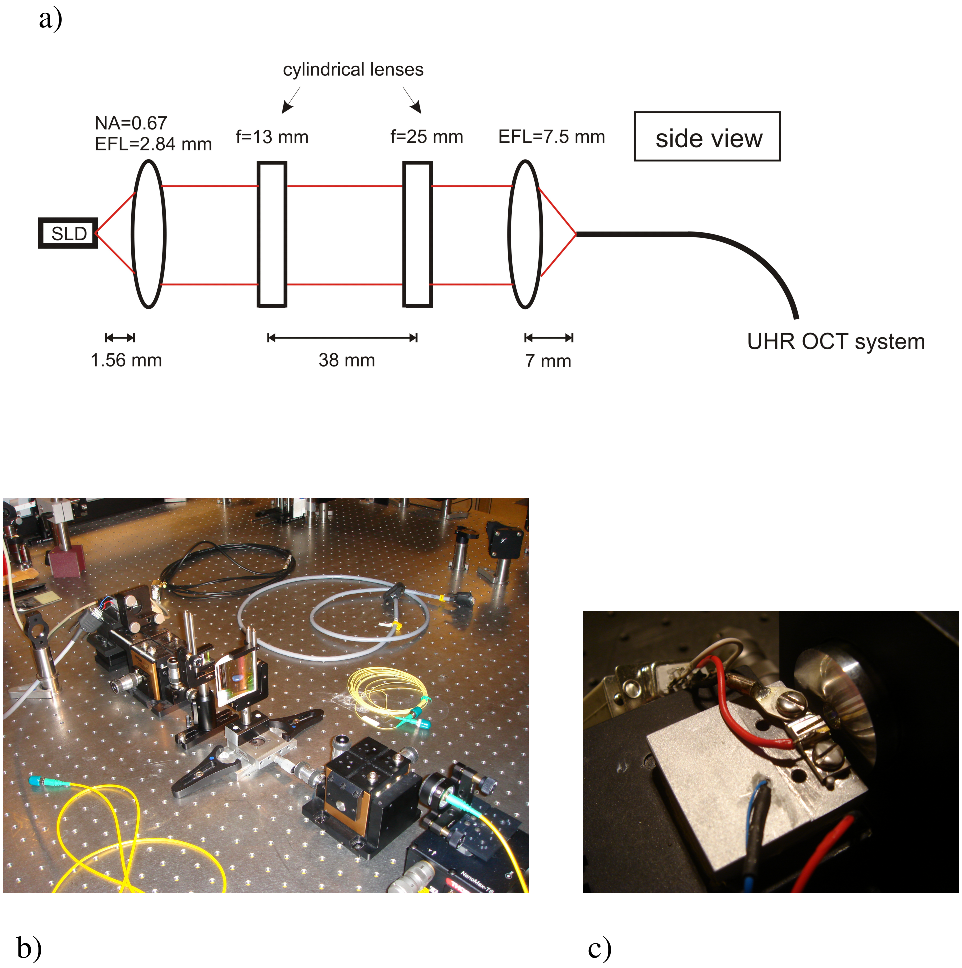

Figure 3.10: The setup for coupling light from the quantum dot based super luminescent diode into the fiber based OCT system, a) sketch of the lenses used for beam shaping b) photo of the setup c) the super luminescent diode

fiber. A photo of the setup is shown in figure 3.10b. Light was coupled directly into a fiber equal to the custom made beam splitter (4.8 μm mode field diameter) to permit high efficiency coupling to the OCT system. This is quite important because coupling from a SMF28 fiber to the custom made fiber introduces a loss of about 30% due to different mode field diameters (experimental measured value). The fiber was mounted on a 3-dimensional translation stage which can also rotate around vertical and horizontal planes to permit maximum degrees of freedom. The beam quality and dimensions were optimized using a beam scanner in between the optical components and finally an optical power meter to optimize the setup for maximum power transmission.

3.5.2 Version M3339

The two-beam splitter configuration was used for this diode. The spectrum of the source is shown in figure 3.11a. It delivers about 50 mW free space and has a bandwidth of 43 nm (FWHM) corresponding to a resolution of 11 μm in tissue, in agreement with the measured value in figure 3.11b. It was possible to couple 12 mW into the OCT system resulting in a sensitivity of 75 dB. This should be compared with a value of 78 dB using a commercial 1300 nm source, same power and same system configuration. As is seen from figure 3.11a the center wavelength is about 1160 nm and therefore about 1/3 of the spectrum is below the fiber cutoff wavelength. Multi mode operation below this wave length results in loss of signal strength and therefore a decrease in sensitivity. Assuming 1/3 of the power is completely lost, i.e. the actual power used for OCT is 2/3 of the 12 mW, a reduction in sensitivity of 2 dB is expected according to eqn. (1.1.7). In addition, the detector response is about 10-15% lower at 1160 nm compared to 1300 mn. This effect corresponds to 1 dB using again eqn. (1.1.7). In total, the sensitivity using the M3339 is expected to be 3 dB lower than the 1300 nm commercial source (assuming same noise properties) which is in accordance with the measurements above. Nevertheless it was possible to acquire OCT images using the quantum dot diode as shown in figure 3.11c.

3.5.3 Version VN590

The two-beam splitter configuration is used for this diode. The spectrum of the source is shown in figure 3.12a. It delivers about 4 mW free space and has a bandwidth of 105 nm (FWHM) corresponding to a resolution of 6 μm in tissue, in agreement with the measured value in figure 3.12b. Due to power limitations, OCT imaging was not performed using this source.

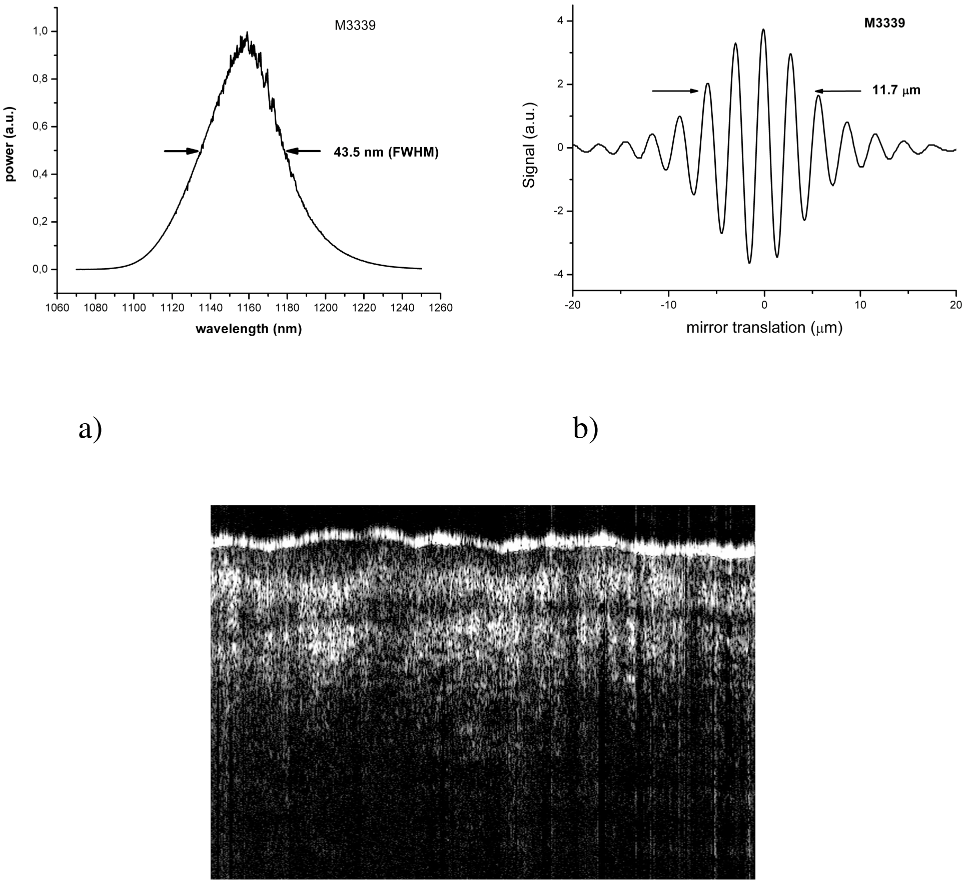

a) b)

c)

Figure 3.11: a) spectrum of M3339 b) interferogram obtained with a mirror in the reference arm c) OCT image acquired on the human skin, width: 1.7 mm height: 1.2 mm

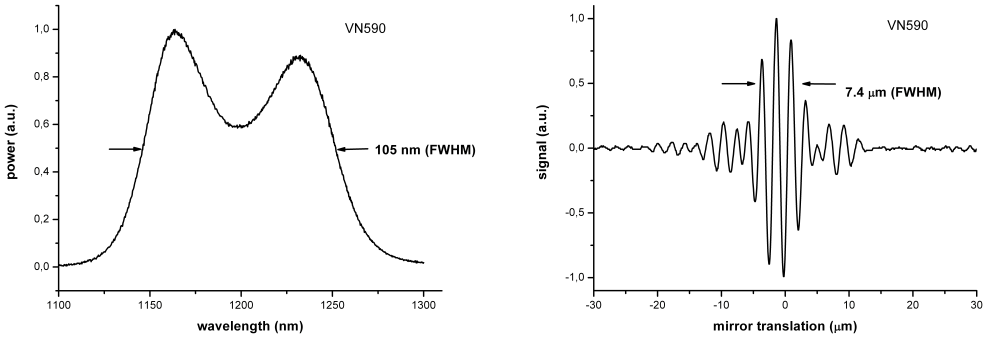

a) b)

Figure 3.12: a) spectrum of VN590 b) interferogram obtained with a mirror in the reference arm

3.5.4 Version VN1045

The circulator configuration is used for this diode. The spectrum of the source is shown in figure 3.13a. It delivers about 50 mW free space and has a bandwidth of 74 nm (FWHM) corresponding to a resolution of 9 μm in tissue, in agreement with the measured value in figure 3.13b. It was possible to couple 14 mW into the OCT system resulting in a sensitivity of 78 dB. In figure 3.13 two OCT images are shown.

3.6 Summary

In conclusion it has been shown, that the high resolution OCT system supports high bandwidth and achieve sensitivity and image quality as expected. The main limitation has been the availability of wide bandwidth light sources necessary to demonstrate high resolution OCT images. With a suitable source exhibiting sufficient power and low noise, OCT images with a resolution close to 2 μm is expected to be achievable using the system.

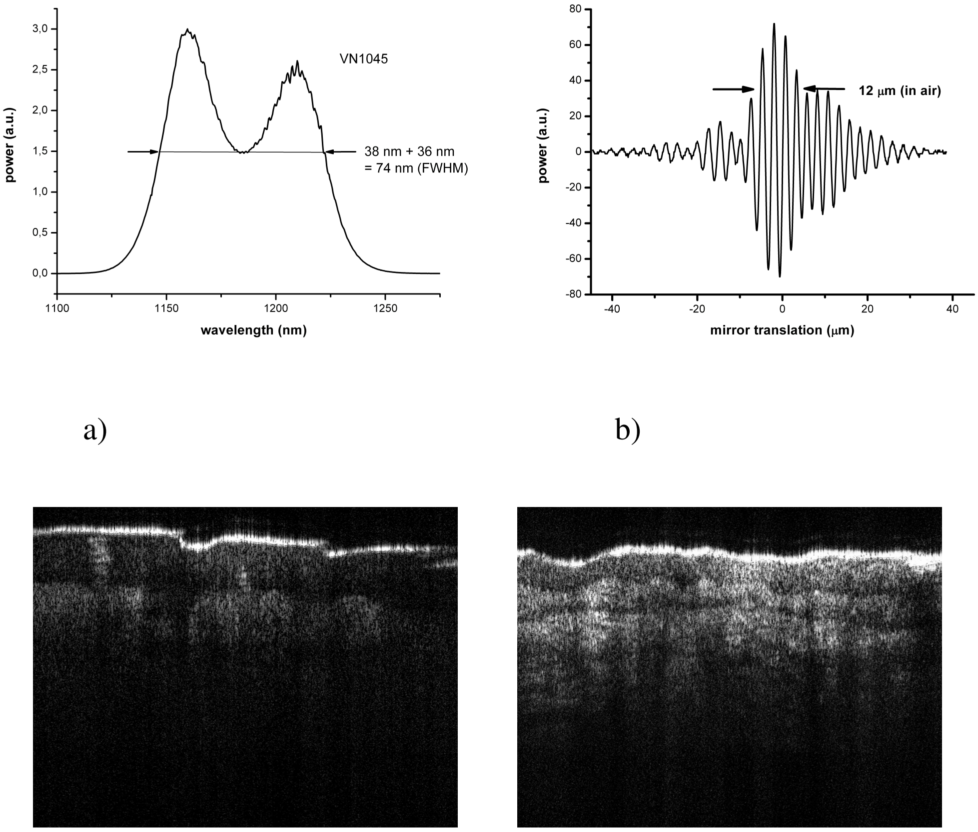

a) b)

c) d)

Figure 3.13: a) spectrum of VN1045 b) interferogram obtained with a mirror in the reference arm c) OCT image acquired on the human thumb with two sweat glands visible, width: 1.8 mm height: 1.3 mm d) OCT image acquired on the human skin, width: 1.8 mm height: 1.3 mm

Chapter 4

Doppler OCT for monitoring treatment

As mentioned in the introduction, D-OCT has a potential for improved diagnostics of different diseases. In addition, it has been suggested that D-OCT could also be used as a tool for monitoring progress during a treatment. In this way it would be possible to tailor the treatment individually to the patient and eventually improve the outcome. In order to reach this ambitious goal, a significant change in blood flow during treatment has to be demonstrated and related to the stage of the treatment. A preliminary attempt to investigate blood flow changes with D-OCT during treatment of skin cancer lesions by photodynamic therapy (PDT) is presented in this chapter. The D-OCT system used for these measurements has also been used for imaging chick embryos and this work is presented in paper **V** together with phantom measurements.

4.1 D-OCT for monitoring PDT

PDT is a non-invasive treatment used for different kinds of cancer and other diseases such as retinal disorders [129]. For skin cancer the advantage of using PDT instead of for example radiotherapy or excision is a better cosmetic result. The treatment modality relies on a sensitizer distributed in the tumor which is excited by light at the right wavelength and reacts with the surrounding tissue resulting in tumor death. The process is shown schematically in figure 4.1. The sensitizer can be distributed either systemically, i.e. through the bloodstream, or topically, for example a cream applied on the skin. After some time, depending on the distribution method, the sensitizer accumulates within the tumor. Following an illumination of the tumor area with adequate wavelength, a photo-chemical process is induced and results in tumor destruction. The treatment effect can be divided

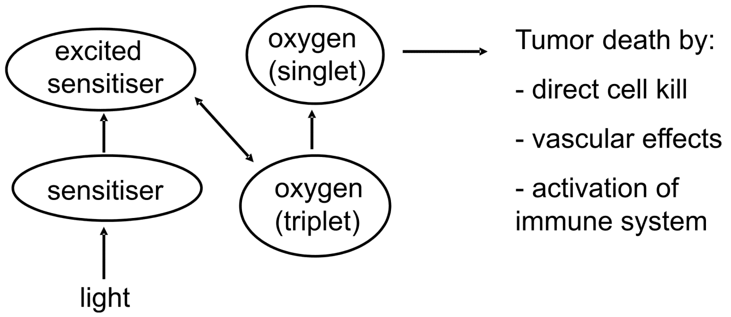

Figure 4.1: The scheme for PDT. The sensitizer is administered in the tumor tissue which is then illuminated with light at a wavelength corresponding to a transition of the sensitizer. The excited sensitizer reacts with tissue oxygen and produces the singlet oxygen state which is highly chemically reactive and eventually leads to cell death via direct cell destruction, vascular damage and activation of the immune system.

in several categories - direct cell kill, indirect response due to vascular effects, and immunological responses. The importance of vascular effect depends on several parameters such as the type of photosensitizer, its distribution pathway, and time between drug supply and light illumination. Understanding these processes in more detail is relevant to optimize the treatment. If the primary effect of PDT is a vascular damage, the time between sensitizer supply and light illumination should be chosen for maximal sensitizer concentration in the blood vessels. On the other hand, if the primary effect is tumor cell destruction, a maximal sensitizer concentration at critical locations in the tumor itself should be the goal. Laser Doppler perfusion imaging has previously been used for blood flow imaging, but does not provide spatial depth resolution [130]. By instead using D-OCT, information about spatial localization of blood flow is possible, and therefore adds additional knowledge. Monitoring vascular changes during PDT with D-OCT has previously been performed on animals during PDT using an interstitial implementation [131]. In this study a decrease in blood flow was reported during PDT of prostate cancer with a systemical distributed sensitizer. In another study using Laser Doppler perfusion imaging, an increase in flow was reported during PDT of skin tumors with a topical distributed sensitizer [132]. Recently, an initial decrease in blood flow followed first by an increase and thereafter slowly decrease was shown using a spectroscopic technique [133]. The blood flow pattern was shown to be dependent on the lesion and level of irradiance. In this study, we aim for non-invasive *in vivo* blood flow measurements on human skin tumors during PDT with a topical applied sensitizer. We have the further advantage of high

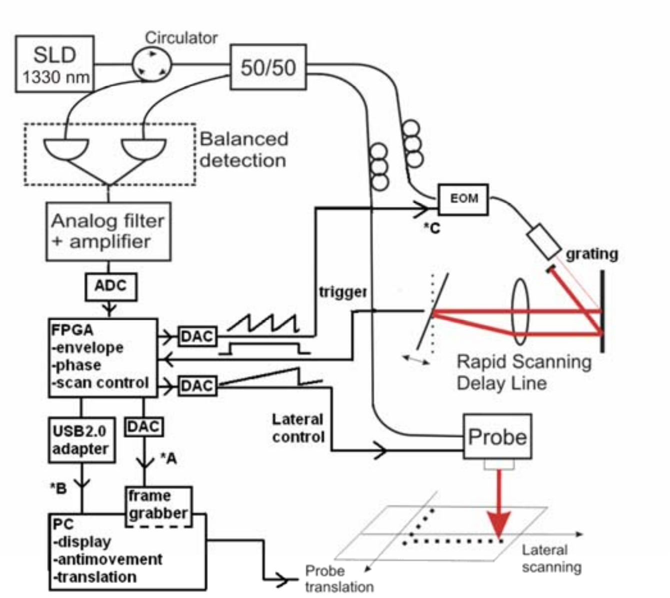

Figure 4.2: D-OCT system block diagram. When acquiring only structural OCT images, data is acquired using the analog frame grabber (*A), the EOM is switched off (*C), and the carrier frequency is set by the delay line. In Doppler mode, data is acquired using the USB interface (*B), and the carrier frequency is then set by the EOM.

spatial resolution compared to most other techniques.

4.2 System description and phantom measurements

The OCT system used in this study is a fiber-based time domain system operating at 1300 nm. A sketch of the system is shown in figure 4.2. The light source is a superluminescent diode with a power of 20 mW and a bandwidth of 66 nm (FWHM) corresponding to a depth resolution of about 8 μm in tissue. Relevant parameters for the system is listed in table 4.1. A circulator is used to accomplish balanced detection to suppress excess noise from the light source thereby improving the signal-to-noise ratio. In the reference arm, an optical delay line similar to the system described in chapter 2 is used, but with the galvano scanner replaced by a faster resonance scanner. The resonance frequency of the resonance scanner is 4 kHz resulting in real time image acquisition of 8 frames per second for an image consisting of 500 A-scans. The system can be operated in two modes, ei-

Table 4.1: Key parameters for the D-OCT system

Center wavelength	1300 nm
Axial PSF (FWHM)	10 μm
Spot size	30 μm
Sensitivity	100 dB
A-scan rate	4 kHz
Interferogram center frequency	3.2 kHz

ther acquiring OCT images only or OCT/D-OCT simultaneously. In OCT mode, the interference signal is detected using a photo detector, band pass filtered and amplified. The interferogram is digitized and converted to an analytic signal by passing it through a digital filter, which eliminates the negative frequency components. The envelope is calculated as the modulus of the analytic signal. The lateral scan is generated by an external saw-tooth generator. Data are transferred to a computer via a frame grabber and the image is finally displayed on the screen. Data acquisition is controlled by a Labview program (National Instruments). Due to the higher data acquisition speed compared to the previously described system, it is possible to acquire 3-dimensional image data as shown in figure 4.3. In the D-OCT mode, an electro-optical modulator (EOM) sets the carrier frequency of the interferogram [134]. A lateral scan is provided by a galvanometer pivoting a mirror to obtain a B-scan image. Envelope and phase information are calculated in a FPGA board (Altera Corp. EP1S80) employing the Kasai algorithm using typical 2 to 8 scans in every lateral position [135]. Data is acquired using an USB interface, and the carrier frequency is then set by the EOM. The phase shift due to block motion of the probe or sample is reduced by a motion artefact rejection algorithm [136]. The sequential scan processing algorithm ensures high velocity sensitivity while maintaining real time imaging, and the motion artefact rejection makes it possible to visualize blood flow *in vivo* with a suppression of noise induced by inter probe-skin movements. By overlaying the flow information to the structural OCT image, so-called Colour D-OCT images are constructed. To suppress noise induced by motion of probe or sample, the hand-held probe was mounted on a supporting arm for the *in vivo* skin measurements presented below, see figure 4.4. Furthermore a link between probe and skin was mounted to provide an angle of 74° between surface and optical beam and provide stability. In general, blood flow was then more pronounced than when measuring with a beam perpendicular to the skin. This means that there is a tendency that blood vessels run parallel to the skin surface.

To test the systems ability of detecting velocities, measurements on a flow

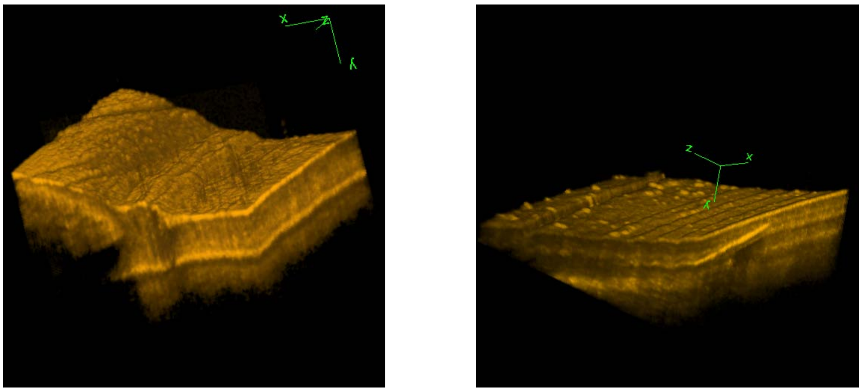

a) b)

Figure 4.3: 3-dimensional image data from a human nail in vivo: a) rendering showing a clear boundary at the nail bed b) image acquired across a white spot on the nail. A high reflection from the middle part of the nail is seen. Dimensions of both renderings: 2.5 mm longitudinal, 2.3 mm vertical and 2 mm transverse. Acquisition time about 50 seconds.

Figure 4.4: The probe was mounted on a supporting arm for stabilization and to reduce noise induced by unwanted probe-sample inter movement, here demonstrated by an OCT model.

phantom with known flow velocity was performed prior to the clinical measurements. A picture of the setup used for the measurements is shown in figure 4.5a. The stationary solid phantom was a mixture of epoxy resin, hardener, ink, and TiO_2-particles aiming for optical properties close to biological tissue. In a depth of 150 μm in the stationary phantom, a small flow channel with a diameter of 400 μm had been drilled as shown in figure 4.5b. For all measurements, we used an intralipid 2% solution for the flow phantom, and an angle of 80.2° between the flow channel and the optical beam. An example is shown in figure 4.5c, with the flow profile in figure 4.5d through the centre of the flow channel. To extract the peak or maximum velocity in the flow channel, a second order polynomial fit is used. In figure 4.6, the peak velocity determined by the D-OCT system is plotted as a function of the pump peak velocity. As expected for a laminar flow, the curve shows a linear relation between the pump flow velocity and the velocity measured with the D-OCT system. A minimum detectable average flow velocity of about 0.3 mm/s was estimated for this particular angle.

4.3 Measurements on normal skin

In order to prepare for the measurements in the clinic, measurements on normal skin was performed to optimize the system. For example the angle between skin surface and beam direction was important to improve the signal strength. Also the threshold phase shift, i.e. the lower limit that determines when a phase shift is shown in the image or not, was crucial to get an image with suppressed noise but with signal from real blood flow. These parameters were chosen empirically by measuring on normal skin. In figure 4.7 an example of a normal skin D-OCT image acquired after the relevant settings has been adjusted. The image is acquired on the palm of a hand and illustrates that the system is able to measure flow velocities typically found in skin. For all skin measurements, 8 sequential was used A-scans to calculate the phase shift. This was necessary to avoid influence of noise. With an image consisting of 320 lateral positions, the frame rate was about 1.5 Hz. During these tests, an interesting observation was made. By following a blood vessel over a few minutes, the flow showed a periodic variation with a change between maximum and almost zero activity. To investigate this effect further relative large vessels on the skin of the hand was monitored for a few minutes using a stable setup with hand and probe attached to each other. In this way a change in angle or position and the corresponding change in signal could be neglected. To quantify the flow change, pixels above a certain threshold in a region of interest was counted as a function of time. This number is hereafter referred to as the flow activity or simply the activity. An example of a measurement on the palm of the hand is shown in figure 4.8. To suppress frame-

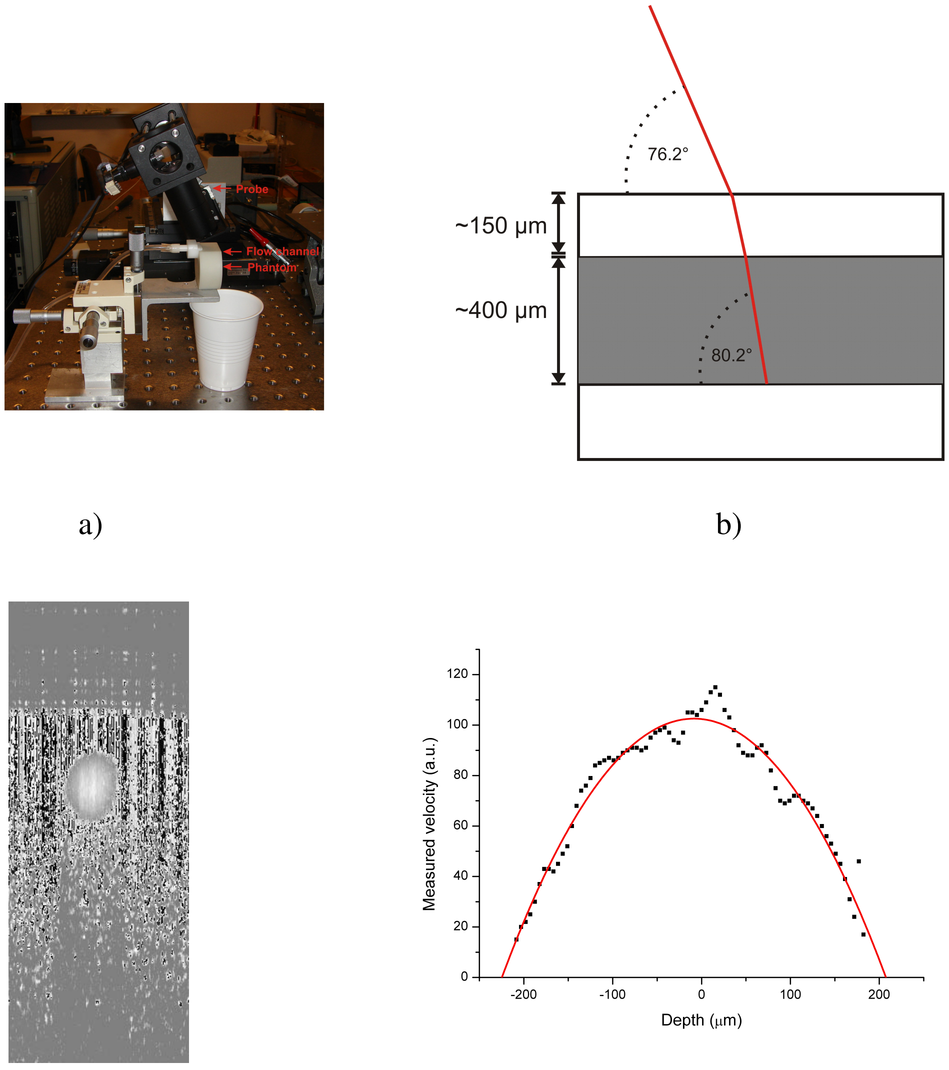

a) b)

c) d)

Figure 4.5: Setup for phantom measurements. a) photo of the setup b) sketch of the setup showing relevant angles c) D-OCT image of the phantom with a flow velocity of 4 mm/s d) corresponding plot of A-scan from the image and a parabolic fit.

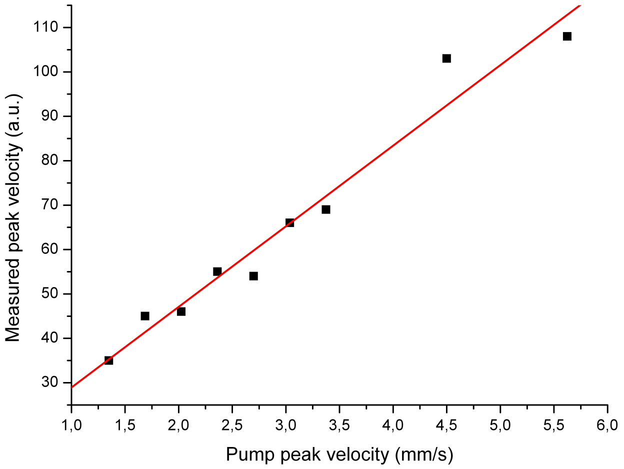

Figure 4.6: Calibration curve obtained from the phantom measurements. As expected a linear relation between pump velocity and measured phase shift is demonstrated.

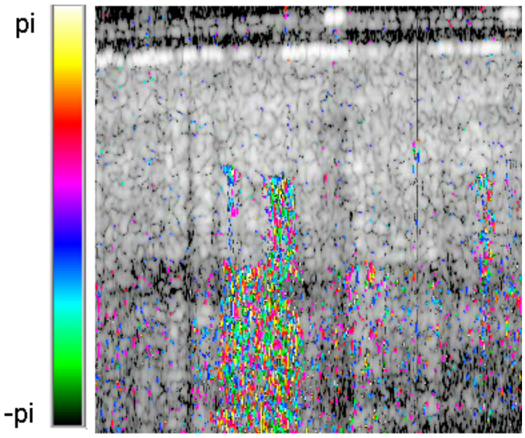

Figure 4.7: D-OCT image acquired on the palm of a hand showing the presence of a blood vessel in dermis (width: 1.3 mm, height: 1.5 mm). The color scale indicates the phase shift.

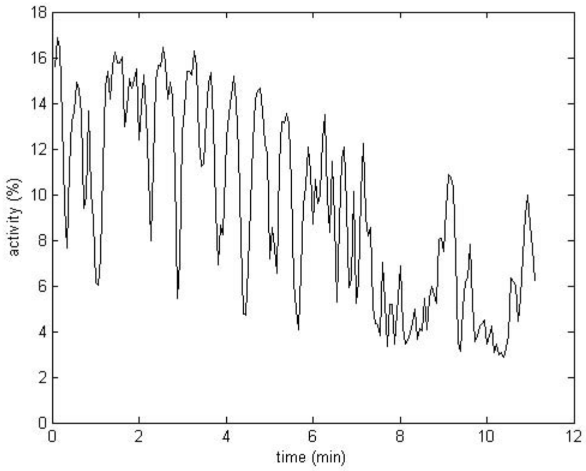

Figure 4.8: D-OCT measurements on normal skin showing time variations. The activity is defined as the sum of pixels with a phase shift above a certain threshold in the region around the vessel. Frame to frame variations were suppressed by averaging 5 frames.

to-frame fluctuations and noise in general, an average of 5 frames was used for this example. The period of the variation is on a scale of minutes or less and was reproducible. Temperature fluctuations with corresponding flow change cannot be ruled out. However, the time scale of the observed blood flow changes seems too fast to be explained by temperature changes. Furthermore the measurements were performed in a room with a stable temperature. On the other hand, the general tendency of a decrease in blood flow with time, see figure 4.8 could be explained by the cooling of the skin attached to the metal extension of the probe, see figure 4.4. But it could also be due to the test person getting relaxed after resting for some minutes. A more objective measure of the changes would be a sum of pixels in the entire image since the region-of-interest is observer dependent. However, this was not possible due to pronounced noise hiding the actual signal. For detecting the effect of varying blood flood, the definition of activity in a region-of-interest is sufficient. The observations above is in agreement with previous findings recording oxygen tension in the human forearm [137]. In this paper the blood flow was measured using a polarographic method without spatial depth resolution. The periodic changes is a complication to monitoring of blood flow changes because it can not necessarily be distinguished whether a change in blood flow is caused directly by the PDT treatment, or just reflects a natural fluctuation. Only by averaging blood flow activity for a time much longer than the period of the natural cycle one can compensate for this effect. This requires measurement durations of at least a few minutes which is a serious problem for D-OCT as a monitoring tool. Assuming a constant blood flow period, an alternative could be to measure in the same phase of the period. This approach would allow comparing blood flow acquired in shorter duration times. However, the stability of the periodic blood flow pattern should be investigated beforehand. The practical use would definitely be limited.

4.4 Clinical measurements

Following the tests described above, clinical measurements on patients with skin tumors were performed. The aim was measuring the blood flow activity before, during and after PDT. First, the sensitizer, in this case 20% ALA cream, was applied to the patients. A few hours are then needed for absorption and distribution within the tumor. Then, the tumor area is illuminated for about 15 minutes with red light to excite the sensitizer and complete tumor destruction. For all images, 8 A-scans were acquired at each lateral location to calculate the phase shift resulting in an acquisition time of about 0.7 s. for a 1.3 mm wide image. Using fewer A-scans for calculating the phase shift results in faster imaging acquisition but unfortunately also in more pronounced noise. We expected an increased blood flow near a tumor compared to normal skin because a tumor is characterized by having an increased metabolism. However, this was not confirmed by our measurements, we observed only very limited blood flow near tumors just like in most normal skin. The observations for normal skin is in agreement with a study using laser Doppler flowmetry reporting an average dermal blood concentration of about 1% or less depending on the site of the skin [138].

Due to the limited blood flow around skin tumors, it was very critical to measure at the same position on the skin to compare blood flow at different times. This requirement would have been more relaxed if blood flow around a tumor was more pronounced and homogeneous. Measuring at the same position proved impossible and therefore we are not able to conclude whether blood flow changes during PDT treatment. Furthermore, variations due to the pressure of the probe on the skin were observed. Therefore, it is important to apply the same pressure every time, and especially to avoid a high pressure that limits the flow. In figure 4.9, a single frame acquired on scar tissue after radiotherapy of a tumor is shown for illustration showing a superficial blood vessel. The frame is part of a movie showing the pulsative nature of the blood flow. In conclusion, we are able to detect blood flow but investigating blood flow changes during PDT of human skin tumors is not possible with the setup presently used due to practical issues.

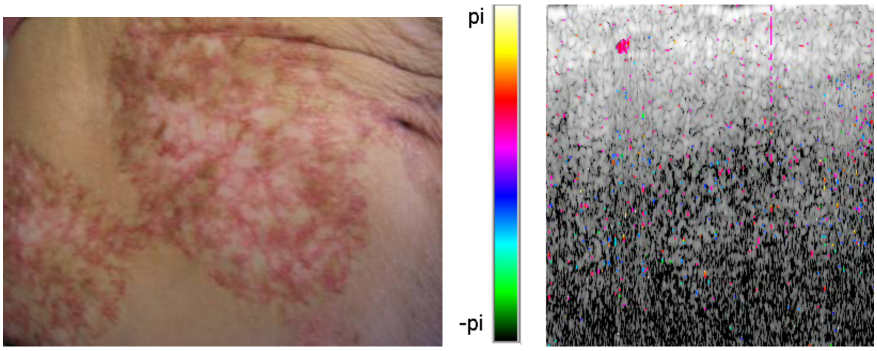

Figure 4.9: Measurements performed on the stomach of a 62 year old woman with scar tissue due to radiotherapy of skin cancer. The colored spot corresponds to a superficial blood vessel (width: 1.3 mm, height: 1.5 mm).

4.5 Summary

As mentioned above, the results of these measurements are extremely sensitive to motion, position and pressure on the skin. When the goal is to measure changes in vascularization, it is critical to measure at the same position within the width of the B-scan. Since the width corresponds to the spot size of the beam, we must be able to position the probe with an accuracy of less than about 30 mm. In practice, this is very difficult. Due to these practical problems, it does not make sense to quantify the blood flow changes because we do not know if changes are related directly to the PDT treatment or rather to a displacement in position, change in angle, pressure applied to the skin etc. In order to make more reliable measurements, a setup with a stationary probe that is not moved in between the measurements is necessary. This can be accomplished by using an interstitial D-OCT implementation with a needle placed in or around the tumor measuring continuously during PDT as demonstrated by Li et al [131]. However, a needle implementation of D-OCT can also affect the blood flow which should be taken into account. Furthermore the non-invasiveness is abandoned which is a serious drawback considering D-OCT as a monitoring tool. On the other hand, if D-OCT is used for research purposes to get more insight to the PDT process it is less critical to use the needle implementation. Minimization of noise induced by motion of the probe is also important, and a faster data acquisition is therefore preferred. This can be accomplished with Fourier domain systems [139]. Using a state-of-the-art Fourier domain D-OCT system would also allow acquiring three dimensional data very fast. Because a larger surface area is then covered, the position of the probe from time to time is less critical than when using only a single B-scan. Natural fluctuations should also be considered and requires for example averaging over time. Finally, we only detected the presence of blood flow and did not measure the absolute value of the velocity. It is also relevant to measure absolute velocities without prior knowledge of the angle between the optical beam and the flow direction in the blood vessel which has already been demonstrated [28]. With these improvements of the setup, future measurements can provide knowledge of blood flow changes during a PDT treatment.

Comments on papers

I H. Morsy, M. Mogensen, J. Thomsen, L. Thrane, P. E. Andersen, G. B. Jemec, *“Imaging of cutaneous larva migrans by optical coherence tomography”*, Travel Medicine and Infectious Disease (2007)

I prepared the system used for the measurements.

II M. Mogensen, J. B. Thomsen, L. T. Skovgaard , G. B. E. Jemec, *“Nail thickness measurements using optical coherence tomography and 20 Mhz ultrasonography”*, British Journal of Dermatology (2007)

I prepared the system used for the measurement, participated in data collection, measurement of refractive index and data analysis.

III M. Mogensen, B. M. Nürnberg, J. L. Forman, J. B. Thomsen, L. Thrane, G. B. E. Jemec, *“In vivo thickness measurement of basal cell carcinoma and actinic keratosis with optical coherence tomography and 20 Mhz ultrasound”*, British Journal of Dermatology (2009)

I prepared the system used for the measurements and participated in the data analysis.

IV M. Mogensen, T. M. Jørgensen, B. M. Nürnberg, H. Morsy, J. B. Thomsen, L. Thrane, G. B. E. Jemec, *“Assessment of Optical Coherence Tomography imaging in the diagnosis of non-melanoma skin cancer and benign lesions vs. normal skin: Observer blinded evaluation by dermatologists and pathologists”*, Dermatologic Surgery (2009)

I prepared the system used for the measurements and participated in the data analysis.

V L. Thrane, H. E. Larsen, K. Norozi, F. Pedersen, J. B. Thomsen, M. Trojer, T. M. Yelbuz, *“Field programmable gate-array-based real-time optical Doppler tomography system for in vivo imaging of cardiac dynamics in the chick embryo”*, Opt. Eng. (2009)

I performed the flow phantom measurements and the following data analysis. Wrote the part of the paper concerning this issue.

Acknowledgements

Many persons have been involved in this project in one or another way. First of all my supervisors at Risø National Laboratory (now Danish Technical University) Peter E. Andersen and Lars Thrane. I want to thank both of them for contributing to the project and for cooperation in the last part finishing writing the thesis. At Risø National Laboratory, a number of persons have been employed and I want to thank them all for cooperation and company. I want to thank Thomas Martini Jørgensen for valuable discussions during the project and for being the "door to reality". I also want to express my thanks to the hard working technicians Finn Pedersen and Henning Engelbrecht for help with Labview, electronics and practical issues etc.

Even though the every day life during the project has mainly been in Denmark, I have always felt very welcome at the Atomic Physics Department in Lund. Thanks to my supervisors Stefan Andersson-Engels for advice and planning of the project. My clinical supervisor Katarina Svanberg contributed with advice and suggestions regarding the clinical tests attempted in Lund. During clinical measurements in Lund I mainly cooperated with Niels Bendsøe to whom I'm very thankful for letting me getting in to the clinic and for answering a lot of questions. In addition, thanks for a nice trip to Jena back in 2007. Gregor Jemec and Mette Mogensen from Roskilde Amtssygehus has been very much entangled in this project and participated with clinical trials and ideas. It has been challenging to work in this interdisciplinary environment but also an experience. I also want to thank Mette Mogensen for feedback regarding the dermatology part of the first chapter of the thesis, Lars Thrane for the biological part and Birgit Sander for providing relevant ophthalmologic images. Finally, my family deserves a big thanks for listening to all my complaints and still offering great support during these years.

References

[1] D. Huang et al, *"Optical Coherence Tomography"*, Science, **254**, 1178-1181 (1991)

[2] W. Drexler, *"Ultrahigh-resolution optical coherence tomography"*, J. of Biomed. Opt., **9**(1), 47-74 (2004)

[3] I. Hartl et al, *"Ultrahigh-resolution optical coherence tomography using continuum generation in air-silica microstructure optical fiber"*, Opt. Lett., **26**(9), 608-610 (2001)

[4] B. Povazay et al, *"Submicrometer axial resolution optical coherence tomography"*, Opt. Lett., **27**(20), 1800-1802 (2002)

[5] B. E. Bouma, G. J. Tearney, *"Handbook of Optical Coherence Tomography*, Marcel Dekker Inc. (2002)

[6] M. Brezinski, *"Optical Coherence Tomography - Principles and Applications"*, Elsevier Inc. (2006)

[7] A. F. Fercher et al, *"Optical coherence tomography - principles and applications"*, Rep. Prog. Phys., **66**, 239-303 (2003)

[8] A. F. Fercher et al, *"Measurement of intraocular distances by backscattering spectral interferometry"*, Opt. Comm., **117**, 43-48 (1995)

[9] M. A. Choma et al, *"Sensitivity advantage of swept source and Fourier domain optical coherence tomography"*, Opt. Expr., **11**(18), 2183-2189 (2003)

[10] B. Liu, M. Brezinski, *"Theoretical and practical considerations on detection performance of time domain, Fourier domain, and swept source optical coherence tomography"*, J. of Biomed. Opt., **12**(4), 044007 (2007)

[11] K. Zheng et al, *"Experimental confirmation of potential swept source optical coherence tomography performance limitations"*, Appl. Opt., **47**(33), 6151-6158 (2008)

[12] D. Choi et al, *"Fourier domain optical coherence tomography using optical demultiplexers imaging at 60.000 lines/s"*, Opt. Lett., **33**(12), 1318-1320 (2008)

[13] W. Wieser et al, *"Multi-Megahertz OCT: High quality 3D imaging at 20 million A-scans and 4.5 GVoxels per second"*, Opt. Expr., **18**(14), 14685-14704 (2010)

[14] M. Hangai et al, *"Three-dimensional imaging of macular holes with high-speed optical coherence tomography"*, Ophthalmology, **114**(4), 763-773 (2007)

[15] L. Thrane et al., *"Analysis of optical coherence tomography systems based on the extended Huygens-Fresnel principle"*, J. Opt. Soc. Am. A, **17**, 484-490 (2000)

[16] R.A. Leitgeb et al, *"Fourier domain optical coherence microscopy with extended focus depth"*, Opt. Lett., **31**(16), 2450-52 (2006)

[17] J. A. Izatt et al, *"Optical coherence tomography and microscopy in gastrointestinal tissues"*, IEEE J. of selected top. in quant. elect., **4**, 1017-1028 (1996)

[18] T. R. Hillman et al, *"The effect of water dispersion and absorption on axial resolution in ultrahigh-resolution optical coherence tomography"*, Opt. Expr., **13**(6), 1860-1874 (2005)

[19] W. Drexler et al, *"Investigation of dispersion effects in ocular media by multiple wavelength partial coherence interferometry"*, Exp. Eye Res., **66**(1), 25-33 (1998)

[20] V. M. Kodach et al, *"Quantitative comparison of the OCT imaging depth at 1300 nm and 1600 nm"*, Biomed. Opt. Expr., **1**(1), 176-185 (2010)

[21] G. M. Hale et al, *"Optical Constants of Water in the 200 nm to 200 micrometer Wavelength Region"*, Appl. Opt., **12**(3), 555-563 (1973)

[22] M Boulton et al, *"Age-related changes in the morphology, absorption and fluorescense of melanosomes and lipofuscin granules of the retinal pigment epithelium"*, Vision Res. , **30**(9), 1291-1303 (1990)

[23] Z. Chen et al, *"Optical Doppler tomographic imaging of fluid flow velocity in highly scattering media"*, Opt. Lett., **22**(1), 64-66 (1997)

[24] J. A. Izatt et al, *"In vivo bidirectional color Doppler flow imaging picoliter blood volumes using optical coherence tomography"*, Opt. Lett., **22**(18), 1439-1441 (1997)

[25] Y. Zhao et al, *"Phase-resolved optical coherence tomography and optical Doppler tomography for imaging blood flow in human skin with fast scanning speed and high velocity sensitivity"*, Opt. Lett., **25**(2), 114-116 (2000)

[26] M. Stucker et al, *"High-resolution laser Doppler perfusion imaging aids in differentiating benign and malignant melanocytic skin tumors"*, Acta Dermato-venereologica, **82**(1), 25-29 (2002)

[27] A. Mirampillai et al, *"Doppler optical cardiogram gated 2D color flow imaging at 1000 fps and 4D in vivo visualization of embryonic heart at 45 fps on a swept source OCT system"*, Opt. Expr., **15**(4), 1627-1638 (2007)

[28] L. Wu, *"Simultaneous measurement of flow velocity and Doppler angle by the use of Doppler optical coherence tomography"*, Opt. and Lasers in Eng., **42**, 303-313 (2004)

[29] Y. Wang et al, *"Measurement of total blood flow in the normal humn retina using Doppler Fourier-domain optical coherence tomography"*, Br. J. Ophtahalmol., **93**, 634-637 (2009)

[30] M. E. J. van Velthoven et al, *"Recent developments in optical coherence tomography for imaging the retina"*, Prog. in Retinal and Eye Res., **26**, 57-77 (2007)

[31] E. Hecht, *"Optics"*, Addison Wesley Longman Inc. (1998)

[32] M. R. Hee et al, *"Polarization-sensitive low-coherence reflectometer for birefringence characterization and ranging"*, J. of Opt. Soc. Am. B, **9**(6), 903-908 (1992)

[33] C. E. Saxer et al, *"High-speed fiber-based polarization-sensitive optical coherence tomography of in vivo human skin"*, Opt. Lett., **25**(18), 1355-1357 (2000)

[34] B. Cense et al, *"Thickness and birefringence of healthy retinal nerve fiber layer tissue measured with polarization-sensitive optical coherence tomography"*, Inv. Opth. and Vis. Scien., **45**(8), 2606-2612 (2004)

[35] C. Ahlers et al, *"Imaging of Retinal Pigment Epithelium in Age-Related Macular Degeneration Using Polarization-Sensitive Optical Coherence Tomography"*, Inv. Opth. Vis. Scien., **51**(4), 2149-2157 (2010)

[36] U. Morgener et al, *"Spectroscopic optical coherence tomography"*, Opt. Lett., **25**(2), 111-113 (2000)

[37] D. J. Faber et al, *"Toward assessment of blood oxygen saturation by spectroscopic optical coherence tomography"*, Opt. Lett., **30**(9), 1015-1017 (2005)

[38] F. Spöler et al, *"Simultaneous dual-band ultra-high resolution optical coherence tomography"*, Opt. Expr., **15**(17), 10832-10841 (2007)

[39] J. S. Bredfeldt et al, *"Molecularly sensitive optical coherence tomography"*, Opt. Lett., **30**(5), 495-497 (2005)

[40] C. A. Patil et al, *"Integrated system for combined Raman spectroscopy-spectral domain optical coherence tomography"*, J. of Biomed. Opt., **16**(11), 011007 (2011)

[41] J. Park et al, *"A dual-modality optical coherence tomography and fluorescence lifetime imaging microscopy system for simultanous morphological and biochemical tissue characterization"*, Biomed. Opt. Expr., **1**(1), 186-200 (2010)

[42] K. König et al, *"Clinical optical coherence tomography combined with multiphoton tomography of patients with skin diseases"*, J. Biophot., **2**(6-7), 389-397 (2009)

[43] S. Jiao et al, *"Simultaneous multimodal imaging with integrated photoacoustic microscopy and optical coherence tomography"*, Opt. Lett., **34**(19), 2961-2963 (2009)

[44] L. Li et al, *"Three dimensional combined photoacoustic and optical coherence microscopy for in vivo microcirculation studies"*, Opt. Expr., **17**(19), 16450-16455 (2009)

[45] C. Huang et al, *"Ultrasound-enhanced optical coherence tomography: improved penetration and resolution"*, J. Opt. Soc. Am. A, **25**(4), 938-946 (2008)

[46] www.zeiss.ca

[47] J. S. Schuman et al, *"Reproducibility of nerve fiber layer thickness measurements using optical coherence tomography"*, Opth., **103**(11), 1889-1898 (1996)

[48] F. A. Medeiros et al, *"Evaluation of retinal nerve fiber layer, optic nerve head, and macular thickness measurements for glaucoma detection using optical coherence tomography"*, Am. J. of Opth., **139** (1), 44-55 (2005)

[49] M. R. Hee et al, *"Optical coherence tomography of age-related macular degeneration and choroidal neovascularization"*, Opth., **103**(8), 1260-1270 (1996)

[50] C. A. Puliafito et al, *"Imaging of macular diseases with optical coherence tomography"*, Opth., **102**(2), 217-229 (1995)

[51] T. H. Ko et al, *"Comparison of ultrahigh- and standard-resolution optical coherence tomography for imaging macular hole pathology and repair"*, Opth., **111**(11), 2033-2043 (2004)

[52] B. Hermann et al, *"Adaptive-optics ultrahigh-resolution optical coherence tomography"*, Opt. Lett., **29**(18), 2142-2144 (2004)

[53] Y. Zhang et al, *"Adaptive optics parallel spectral domain optical coherence tomography for imaging the living retina"*, Opt. Expr, **13**(12), 4792-4811 (2005)

[54] R. J. Zawadzki et al, *"Adaptive-optics optical coherence tomography for high-resolution and high-speed 3D retinal in-vivo imaging"*, Opt. Expr., **13**(21), 8532-8546 (2005)

[55] B. Povazay et al, *"Minimum distance mapping using three-dimensional optical coherence tomography for glaucoma diagnosis*, J. of Biomed. Opt., **12**(4), 041204 (2007)

[56] A. Unterhuber et al, *"In vivo retinal optical coherence tomography at 1040 nm-enhanced penetration into the choroid"*, Opt. Expr., **13**(9), 3252-3258 (2005)

[57] B. Sander et al, *"Enhanced optical coherence tomography imaging by multiple scan averaging"*, Br. J. of Opth., **89**, 207-212 (2005)

[58] T. M. Jorgensen et al, *"Enhancing the signal-to-noise ratio in ophthalmic optical coherence tomography by image registration - method and clinical examples"*, J. of Biomed Opt., **12**(4), 041208 (2007)

[59] B. Cense et al, *"In vivo depth-resolved birefringence measurements of the human retinal nerve fiber layer by polarization-sensitive optical coherence tomography"*, Opt. Lett., **27**(18), 1610- 1612 (2002)

[60] B. R. White et al, *"In vivo dynamic human retinal blood flow imaging using ultra-high-speed spectral domain optical Doppler tomography"*, Opt. Expr., **11**(25), 3490-3497 (2003)

[61] R. K. Wang et al, *"Three dimensional optical angiography"*, Opt. Expr., **15**(7), 4083-4097 (2007)

[62] L. An et al, *"High-resolution wide-field imaging of retinal and choroidal blood perfusion with optical microangiography"*, J. of Biomed. Opt., **15**(2), 026011 (2010)

[63] K. Bizheva et al, *"Depth-resolved probing of retinal physiology with functional ultrahigh-resolution optical coherence tomography"*, Proc. Nat. Acad. Sci. US, **103**, 5066-5071 (2006)

[64] J. A. Neville et al, *"Management of nonmelanoma skin cancer in 2007"*, Nat. Clin. Pract. Oncol., **4**, 462-469 (2007)

[65] J. Welzel, *"Optical coherence tomography in dermatology: a review"*, Skin Res. and Techn., **7**, 1-9 (2001)

[66] M. Mogensen et al, *"In vivo thickness measurement of basal cell carcinoma and actinic keratosis with optical coherence tomography and 20 Mhz ultrasound"*, Br. J. of Derm., **160**(5), 1026-1033 (2009)

[67] R. Steiner et al, *"Optical coherence tomography: clinical applications in dermatology"*, Med. Laser Appl., **18**, 249-259 (2003)

[68] G. V de Giorgi et al, *"Possible histopathologic correlates of dermoscopic features in pigmented melanocytic lesions identified by means of optical coherence tomography"*, Exp. Dermatol., **14**, 56-59 (2005)

[69] T. Gambichler et al, *"Characterization of benign and malignant melanocytic skin lesions using optical coherence tomography in vivo"*, J. Am. Acad. Dermatol, **57**(4), 629-637 (2007)

[70] T. Gambichler et al, *"A comparative pilot study on ultraviolet-induced skin changes assessed by noninvasive imaging techniques in vivo"*, Photochem. and Photobio., **82**(4), 1103-1107 (2006)

[71] T. Gambichler et al, *"In vivo data of epidermal thickness evaluated by optical coherence tomography: Effects of age, gender, skin type, and anatomic site"*, J. of Derm. Sci., **44**(3), 145-152 (2006)

[72] F. G. Bechara et al, *"Histomorphologic correlation with routine histology and optical coherence tomography"*, Skin Res. and Techn., **10**, 169-173 (2004)

[73] J. M. Olmedo et al, *"Optical coherence tomography for the characterization of basal cell carcinoma in vivo: A pilot study"*, J. Am. Acad. Derm., **55**(3), 408-412 (2006)

[74] T. Gambichler et al, *"In vivo optical coherence tomography of basal cell carcinoma"*, J. of Dermatol. Sci., **45**(3), 167-173 (2007)

[75] J. M. Olmedo et al, *"Correlation of thickness of basal cell carcinoma by optical coherence tomography in vivo and routine histologic findings: A pilot study"*, Dermatol. Surg., **33**, 421-426 (2007)

[76] A. Tycho et al, *"Machine-learning classification of non-melanoma skin cancers from image features obtained by optical coherence tomography"*, Skin res. and Techn. (in press, 2008)

[77] V. R. Korde et al, *"Using optical coherence tomography to evaluate skin sun damage and precancer"*, Las. in Surg. and Med., **39**, 687-695 (2007)

[78] M. Khandwala et al, *"Imaging of periocular basal cell carcinoma using en face optical coherence tomography: a pilot study"*, Br. J. Ophthalmol., **94**, 1332-1336 (2010)

[79] J. Strasswimmer et al, *"Polarization-sensitive optical coherence tomography of invasive basal cell carcinoma"*, J. of Biomed. Opt., **9**(2), 292-298 (2004)

[80] S. J. Lin et al, *"Discrimination of basal cell carcinoma from normal dermal stroma by quantitative multiphoton imaging"*, Opt. Lett., **31**(18), 2756-2758 (2006)

[81] A. Nijssen et al, *"Discriminating Basal cell carcinoma from its surrounding tissue by Raman spectroscopy"*, J. of Invest. Derm., **119**(1), 64-69 (2002)

[82] M. C. Pierce et al, *"Collagen denaturation can be quantified in burned human skin using polarization-sensitive optical coherence tomography"*, Burns, **30**, 511-517 (2004)

[83] S. M. Srinivas et al, *"Determination of burn depth by polarization-sensitive optical coherence tomography"*, J. of Biomed. Opt., **9**(1), 207-212 (2004)

[84] M. Todorovic et al, *"In vivo burn imaging using Mueller optical coherence tomography"*, Opt. Expr., **16**(14), 10279-10284 (2008)

[85] J. Welzel, *"Optical coherence tomography in contact dermatitis and psoriasis"*, Arch. Dermatol. Res., **295**, 50-55 (2003)

[86] Z. Hamdoon, *"Optical coherence tomography-guided photodynamic therapy for skin cancer: Case study"*, Photodiag. and Photodyn. Therapy, **8**, 49-52 (2011)

[87] www.who.int

[88] I. K. Jang et al, *"Visualization of coronary atherosclerotic plaques in patients using optical coherence tomography: Comparison with intravascular ultrasound"*, J. of the Am. Coll. of Cardiology, **39**(4), 604-609 (2002)

[89] A. F. Low et al, *"Technology insight: optical coherence tomography - current status and future development"*, Nat. Clin. Pract. Cardiovas. Med., **3**(3), 154-162 (2006)

[90] G. J. Tearney et al, *"Optical coherence tomography for imaging the vulnerable plaque"*, J. of Biomed. Opt., **11**(2), 021002 (2006)

[91] G. J. Tearney et al, *"Quantification of macrophage content in atherosclerotic plaques by optical coherence tomography"*, Circulation, **107**(1), 113-119 (2003)

[92] D. Levitz et al, *"Determination of optical scattering properties of highly-scattering media in optical coherence tomography images"*, Opt. Expr., **12**(2),249-259 (2004)

[93] H. Yabushita et al, *"Characterization of human atherosclerosis by optical coherence tomography"*, Circulation, **106**(13), 1640-1645 (2002)

[94] I. K. Jang et al, *"In vivo characterization of coronary atherosclerotic plaque by use of optical coherence tomography"*, Circulation, **111**(12), 1551-1555 (2005)

[95] M. E. Brezinsky, *"Applications of optical coherence tomography to cardiac and musculoskeletal diseases: bench to bedside?"*, J. of Biomed. Opt., **12**(5), 051705 (2007)

[96] S. D. Giattina et al, *"Assessment of coronary plaque collagen with polarization sensitive optical coherence tomography (PS-OCT)"*, Int. J. of Card., **107**(3), 400-409 (2006)

[97] B. E. Bouma et al, *"Evaluation of intracoranary stenting by intravscular optical coherence tomography"*, Heart, **89**(3), 317-320 (2003)

[98] G. J. Tearney et al, *"Three-dimensional Coronary Artery Microscopy by Intracoronary Optical Frequency Domain Imaging"*, Jacc-Cardiovasc. Im., **1**(6), 752-761 (2008)

[99] D. Matsumoto et al, *"Neointimal coverage of sirolimus-eluting stents at 6-month follow-up: evaluated by optical coherence tomography"*, Eur. Heart Jour., **28**(8), 961-967 (2007)

[100] G. Unal et al, *"Stent implant follow-up in intravascular optical coherence tomography images"*, Int. J. of Cardiovasc. Im., **26**(7), 809-816 (2010)

[101] www.lightlabimaging.com

[102] I. Waxman et al, *"High-frequency probe ultrasonography has limited accuracy for detecting invasive adenocarcinoma in patients with Barrett's esophagus and high-grade dysplasia or intramucosal carcinoma: A case series"*, Am. J. of Gastroent., **101**(8), 1773-1779 (2006)

[103] Y. Chen et al, *"Ultrahigh resolution optical coherence tomography of Barrett's esophagus: preliminary descriptive clinical study correlating images with histology"*, Endoscopy, **39**(7), 599-605 (2007)

[104] G. Isenberg et al, *"Accuracy of endoscopic optical coherence tomography in the detection of dysplasia in Barrett's esophagus: a prospective, double-blinded study"*, Gastrointest. Endos., **62**(6), 825-831 (2005)

[105] C. A. Jesser et al, *"High resolution imaging of transitional cell carcinoma with optical coherence tomography: feasibility for the evaluation of bladder pathology"*, Br. J. of Radiology **72**(864), 1170-1176 (1999)

[106] E. V. Zagayniva et al, *"In vivo optical coherence tomography feasibility for bladder disease"*, J. of Urology, **167**(3), 1492-1496 (2002)

[107] M. J. Manyak et al, *"Evaluation of superficial bladder transitional-cell carcinoma by optical coherence tomography"*, J. of Endourologi, **19**(5), 570-574 (2005)

[108] S. C. Whiteman et al, *"Optical coherence tomography: Real-time imaging of bronchial airways microstructure and detection of inflammatory/neoplastic morphologic changes"*, Clin. Can. Res., **12**(3), 813-818 (2006)

[109] Y. Yang et al, *"Use of optical coherence tomography in delineating airways microstructure: comparison of OCT images to histopathological sections"*, Phys. in Med. and Bio., **49**(7), 1247-1255 (2004)

[110] C. Zhou et al, *"Integrated optical coherence tomography and microscopy for ex vivo multiscale evaluation of human breast tissue"*, Cancer Res., **70**(24), 10071-10079 (2010)

[111] R. A. McLaughlin et al, *"Imaging of human lymph nodes using optical coherence tomography: potential for staging cancer"*, Cancer Res., **70**(7), 2579-2584 (2010)

[112] B. A. Standish et al, *"Interstitial Doppler Optical Coherence Tomography as a Local Tumor Necrosis Predictor in Photodynamic Therapy of Prostatic Carcinoma: An in vivo Study"*, Cancer Res., **68**, 9987-9995 (2008)

[113] M. L. Onozato et al, *"Optical coherence tomography of human kidney"*, J. Urol., **183**(5), 1669-1670 (2010)

[114] S. A. Boppart et al, *"Noninvasive assessment of the developing Xenopus cardiovascular system using optical coherence tomography"*, Proc. Natl. Acad. Sci., **94**, 4256-4261 (1997)

[115] S. A. Boppart et al, *"Investigation of developing embryonic morphology using optical coherence tomography"*, Dev. Biol., **177**, 54-63 (1996)

[116] B. B. Keller, *“Embryonic cardiovascular function, coupling, and maturation: a species view”* in Development of Cardiovascular Systems, W. W. Burggren, and B. B. Keller, eds. (University Press, 1998), pp. 65-87.

[117] J. I. Hoffman, *“Incidence of congenital heart disease, I: postnatal incidence”* Pediatr. Cardiol., **16**, 103-113 (1995).

[118] T. M. Yelbuz et al, *“Optical coherence tomography: a new high-resolution imaging technology to study cardiac development in chick embryos”*, Circulation, **106**, 2771-2774 (2002)

[119] M. A. Choma et al, *“Images in cardiovascular medicine: in vivo imaging of the adult Drosophila melanogaster heart with real-time optical coherence tomography”*, Circulation, **114**, e35-6 (2006)

[120] M. W. Jenkins et al, *“Ultrahigh-speed optical coherence tomography imaging and visualization of the embryonic avian heart using a buffered Fourier domain mode locked laser”*, Opt. Expr., **15**, 6251-6267 (2007)

[121] W. Luo et al, *“Three-dimensional optical coherence tomography of the embryonic murine cardiovascular system”*, J. Biomed. Opt., **11**, 021014 (2006)

[122] K. Norozi et al., *“In vivo visualisation of coronary artery development by high-resolution optical coherence tomography”*, Heart, **94**, 130 (2008)

[123] A. Gerger et al, *“Sensitivity and specificity of confocal laser-scanning microscopy for in vivo diagnosis of malignant skin tumors”*, Cancer, **107**(1), 193-200 (2006)

[124] G. J. Tearney et al, *“High-speed phase- and group-delay scanning with a grating-based phase control delay line”*, Opt. Lett., **22**(23), 1811-1813 (1997)

[125] NANO UB-SOURCES, see www. nano-ub-sources.org

[126] M. Blazek et al, *“ Intensity noise of ultrabroadband Quantum Dot light emitting diodes and lasers at 1.3 µm”*, Conference on Noise and Fluctuations in Photonics, Quantum Optics, and Communications, **6603**, Y6031-Y6031 (2007)

[127] A. M. Rollins et al, *“In vivo video rate optical coherence tomography”*, Opt. Expr., **3**(6), 219-229 (1998)

[128] S. Borquin et al, *"Ultrahigh resolution real time OCT imaging using a compact femtosecond Nd:Glass laser and a nonlinear fiber"*, Opt. Expr., **11**(24), 3290-3297 (2003)

[129] B. C. Wilson et al, *"The physics, biophysics and technology of photodynamic therapy"*, Phys. Med. Biol., **53**, R61-R109 (2008)

[130] I Wang et al, *"Superficial blood flow following photodynamic therapy of malignant non-melanoma skin tumours measured by laser Doppler perfusion imaging"*, Br. J. of Derm.,**136**, 184-189 (1997)

[131] H. Li et al, *"Feasibility og interstitial Doppler optical coherence tomography for* in vivo *detection of microvascular changes during photodynamic therapy"*, Lasers in Surg. and Med., **38**, 754-761 (2006)

[132] S. Paalsson et al, *"Kinetics of superficial perfusion and temperature in connection with photodynamic therapy of basal cell carcinomas using esterified and non-esterified 5-aminolaevulinic acid"*, Br. J. of Derm., **148**, 1179-1188 (2003)

[133] T. L. Becker et al, *"Monitoring blood flow responses during topical ALA-PDT"*, Biomed. Opt. Expr., **2** (1), 123-130 (2011)

[134] J. F. de Boer et al, *"Stable carrier generation and phase-resolved digital data processing in optical coherence tomography"*, Appl. Opt., **40**(31), 5787-5790 (2001)

[135] C. Kasai et al, *"Real-time two-dimensional blood flow imaging using an autocorrelation technique"*, IEEE Transactions on Sonics and Ultrasonics, **32**(3), 458-464 (1985)

[136] V. X. D. Yang et al, *"Improved phase-resolved optical Doppler tomography using the Kasai velocity estimator and histogram segmentation"*, Opt. Comm. **208**, 209-214 (2002)

[137] N. T. S. Evans et al, *" The spatial correlation of fluctuations of the blood flow in forearm skin"*, Br. J. of Derm. **96**(6), 609-614 (1977)

[138] I. Fredriksson et al, *"Optical microcirculatory skin model: assessed by Monte Carlo simulations paired with in vivo laser Doppler flowmetry"*, J. of Biomed. Opt., **13**(1), 014015 (2008)

[139] A. Mariampillai et al, *"Doppler optical cardiogram gated 2D color flow imaging at 1000 fps and 4D in vivo visualization of embryonic heart at 45 fps on a swept source OCT system"*, Opt. Expr. **15**, 1627-1638 (2007)

Paper I

Imaging of cutaneous larva migrans by optical coherence tomography

Travel Medicine and Infectious Disease (2007) **5**, 243–246

Available at www.sciencedirect.com

ScienceDirect

journal homepage: www.elsevierhealth.com/journals/tmid

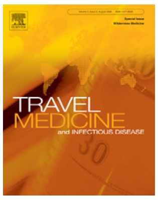

Imaging of cutaneous larva migrans by optical coherence tomography

Hanan Morsy[a,*], Mette Mogensen[a], Jakob Thomsen[b], Lars Thrane[b], Peter E. Andersen[b], Gregor B.E. Jemec[a]

[a]*Department of Dermatology, University of Copenhagen, Roskilde Hospital DK-4000 Roskilde, Denmark*
[b]*Department of Optics and Plasma Research, Risoe National Laboratory, Denmark*

Received 30 September 2006; received in revised form 27 November 2006; accepted 7 December 2006
Available online 15 February 2007

KEYWORDS
Optical coherence tomography;
Optical imaging;
Ultrasound;
Cutaneous larva migrans;
Creeping eruption

Summary
Background: Cutaneous larva migrans is a parasitic skin eruption caused by migration of larvae of various nematodes. Diagnosis of cutaneous larva migrans is currently based on the clinical signs of the creeping eruption. We are investigating a new diagnostic technology called optical coherence tomography (OCT) , which is potentially able to visualize structures in the skin with an 8 μm resolution. This technology could therefore potentially allow rapid, non-invasive, in vivo diagnosis of infestations.
Method: Clinical cases of cutaneous larva migrans ($n = 3$) were studied. All patients had a characteristic itching, serpinginous eruption typical of cutaneous larva migrans. The parasites were acquired on beach holidays in Thailand and Malaysia. All skin lesions were imaged by an OCT system developed at Risoe National Laboratory, Denmark.
Result: Two out of three patients showed a round to oval structure (diameter 0.3–0.5 mm) in the epidermis, Thus distinct OCT morphology in skin areas affected by cutaneous larva migrans was demonstrated. The larvae were not visualized in any of the patients.
Conclusion: This study demonstrates that OCT a novel optical imaging technology, can image the larva tunnel in the skin with adequate spatial resolution, but not the larvae itself. OCT has a potential in imaging of skin infestations.

Introduction

Cutaneous larva migrans is referring to the creeping eruption due to human skin invasion by animal hookworm larvae.[1] In cutaneous larva migrans the parasitic skin

---

[*] Corresponding author. Tel.: +45 47322116; fax: +45 47322128.
E-mail address: rsmmog@ra.dk (H. Morsy).

1477-8939/$ - see front matter
doi:10.1016/j.tmaid.2006.12.004

eruption is caused by migration of larvae of various nematodes, most commonly dog and cat hook worms (*Ancylostoma caninum* and *A. braziliense*), also gnasthostoma species can manifest as cutaneous larva migrans if it reaches the subcutaneous tissue after oral ingestion. The infestation of cutaneous larva migrans occurs after contact with contaminated soil or animal products, and is the most frequent disease in travelers returning from tropical countries.[2] The majority (95%) of cutaneous larva migrans patients have a history of exposure to the beach.[3] Clinically cutaneous larva migrans is characterized by the presence of an allergic reaction to the products of the larva in the epidermis and less often the upper dermis.[4] This allergic reaction takes the form of an erythematous linear or serpiginous dermatitis, with special predilection to buttocks and lower limbs.[5,6] There are no specific diagnostic tests for all larva infestations, but enzyme-linked immunosorbent assays (ELISA) are available for the diagnosis of some nematodes and helminthes.[7]

We report three clinical cases of cutaneous larva migrans imaged by a novel non-invasive optical imaging technology called optical coherence tomography (OCT) to explore the possible role of OCT as a diagnostic tool[8–11] for selected cases of cutaneous larva migrans.

Materials and methods

OCT is a novel non-invasive optical imaging technology. It provides cross-sectional tomographic real-time images of tissue pathology in situ with an axial resolution as high as 1–3 μm.[12–14] OCT images are generated when an optical beam is scanned across the tissue and echo time delay and intensity of backscattered light is measured. Velocity of light is extremely high and optical echoes cannot be measured directly, therefore OCT is based on low-coherence interferometry, correlating backscattered light from tissue with light that has travelled a known reference path. Hence, OCT is analogue to B-mode ultrasound pulse-echo imaging with an optical rather than acoustical reflectivity being measured.

The OCT-system used in this study was developed at Risoe National Laboratory, Denmark. Our OCT-probe is hand-held light-weight fiber-based and easy to handle. The probe is applied directly to the skin, after applying ultrasound gel to the skin. Due to the easy applicability of the probe the entire skin surface can be examined with our OCT-system. The scanning lasts a few seconds, and has not caused any discomfort to patients in earlier studies.[10,15] The light source used is a superluminescent diode with a center wavelength of 1318 nm, and a FWHM bandwidth of 66 nm. Axial resolution is 8 μm (in tissue), and the lateral resolution is 24 μm. The image data are displayed by assigning gray scales to each reflection according to the measured signal strength. The optical fiber-based handheld OCT probe sends infrared light onto the skin at optical power densities in compliance with ANSI safety regulations.

Ultrasound examinations were done with a dedicated 20 MHz scanner (Dermascan C 3.1, Cortex Technology, Denmark). The scanner has an axial resolution of 50 μm and lateral 350 μm. Ultrasound provides objective, accurate, noninvasive and easy measurements of several parameters of skin morphology and enables visualization of subclinical and deep lesions. Ultrasound imaging allows the identification of diameters and the depth of pathology such as inflammation, neoplasm and infestations.[16]

The study population consists of all patients diagnosed clinically with cutaneous larva migrans in our Department in the period of March 2006–July 2006. Patients agreed to participate in accordance with Helsinki guidelines.

Case reports

Patient 1

A 9-year-old girl returned from a beach holiday in Thailand, where she was playing with cats. The creeping eruption started in Thailand in April 2006, numerous pustular and erythematous serpiginous lesions developed on her left foot, and measured 0.3–1 cm in width and 10 cm in total length (see Fig. 1) when the patient was referred. The patient was referred to our department after systemic antibiotic and local antiseptic treatment, which was prescribed in order to control the bacterial super infection and accompanying fever. General examinations as well as laboratory investigations were normal. The patient was successfully treated with oral ivermictin (200 μg/kg).

Patient 2

A 51-year-old woman returned from beach holiday in Malaysia July 2006, 1 week later the patient was admitted to the hospital due to headache, myalgia and malaise. She presented with fever (39.6 °C) and a rash. Laboratory tests showed low natrium 134 mmol/l (137–145 mmol/l) and low platelets: 102×10^9($145–390 \times 10^9$), normal eosinophils, normal IgE. All other tests were also normal, including tests for Malaria and Dengue fever. An erythematous serpiginous

Figure 1 Clinical presentation of cutaneous larva migrans in Patient 1 with pustular, linear and serpiginous lesions on her foot. The black marks show some sites of Optical coherence tomography scanning. Black arrows indicate where OCT imaging was also done in search of the larva and delineation of the tunnel.

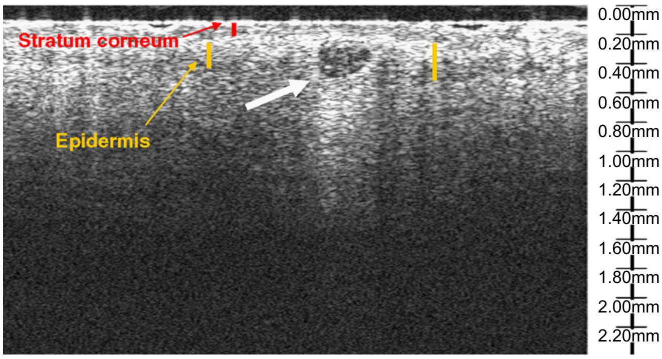

Figure 2 Optical coherence tomography imaging of cutanous larva migrans. OCT image from Patient 1. The dark oval structure represents the cross-section of the empty cutaneous larva migrans larva tunnel, thus the larva is not present in the tunnel. The red arrow indicates the stratum corneum , the yellow arrows demarcate the epidermis and the white arrow points out the larger penetration depth in the dermis.

and pruritic rash appeared located to the lower abdomen, pubic region and left thigh. Cryotherapy was attempted before admission to our department, but due to ongoing activity the patient was treated successfully with oral ivermictin (200 μg/kg).

Patient 3

A 48-year-old woman with a serpiginous eruption that appeared on the abdomen 2 weeks after she had returned from a beach holiday in Thailand February 2006, where she recalled sunbathing on a dirty straw mat. The size of the eruption was 0.3–0.5 cm in width and 2 cm in length and was associated with severe pruritus. The eruption was no longer creeping when we saw the patient, and was therefore presumed treated successfully with cryotherapy by the office-based dermatologist.

Results

All patients were diagnosed clinically. OCT -imaging was done over the serpiginous lesions in their entirety in all patients. In patient 1 OCT-imaging demonstrated the boundaries of the cross-section of the larva tunnel located in the epidermis. The OCT-image (Fig. 2) shows an oval air filled structure (diameter 0.3–0.5 mm) interestingly a larger penetration depth is seen below the track due to the low signal attenuation in the track compared to the surrounding skin tissue. Ultrasonography of the larva tunnel was done for comparison with the optical coherence tomography images (see Fig. 3). Ultrasound images did not reveal the delineation of neither the tunnel nor the larva, only an epidermal, hypoechogenic infiltrate representing inflammation could be demonstrated.

In patient 2 OCT-images of the lesions showed a characteristic cross-section of the larva tunnel, but the delineation of the tunnel was not as clear as in Patient 1.

In patient 3 OCT imaging did not reveal a cross-section of the larva tunnel similar to OCT image from Patient 1, only a non-specific disruption of the layered structure of epidermis and dermis could be identified.

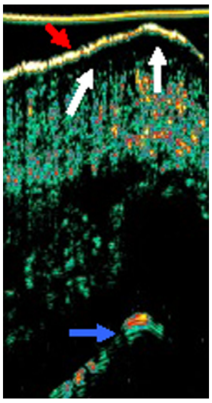

Figure 3 Twenty MHz ultrasonography image of cutaneous larva migrans tunnel on foot of Patient 1. Red arrow is the entrance echo, white arrows are pointing towards epidermis with a low echogenic signal due to inflammation; the delineation of the larva tunnel is not obvious. Blue arrow is metatarsal structures. The larva is not present in the tunnel.

Discussion

In most cases of cutaneous larva migrans the diagnosis is made by identifying the characteristic clinical presentation, although atypical presentations such as the bullous cutaneous larva migrans or cutaneous larva migrans with folliculitis occur.[17] Differential diagnosis includes scabies, erythema chronicum migrans, herpes zoster, lichen striatus, phytophotodermatitis and superficial thrombophlebitis.[1,5] Laboratory tests are not essential for diagnosis, but detection of eosinophilia of the peripheral blood may support the diagnosis. In some cases it may be necessary to biopsy for histopathological examination from the suspected skin lesion, although histopathology is often not helpful in the diagnosis particularly because it is difficult to localize the most appropriate place from where to take the biopsy.[5] Histopathology typically shows the larva tunnel situated in the epidermis or below, surrounded by an infiltrate of eosinophilic cells. Spongiotic dermatitis with spongiotic vesicles containing neutrophils and eosinophils and a mixed-cell dermal infiltrate with numerous eosinophils can also be seen.[18] The tunnel is usually circular and air filled.[19]

In the present study, OCT imaging of three patients with cutaneous larva migrans demonstrated potential of this novel non-invasive investigative tool for imaging of skin infestations, in accordance with an earlier pilot study where a scabies mite was imaged by optical coherence tomography.[20]

An obvious larva tunnel could only be identified by OCT-imaging in Patient 1. OCT imaging showed the presence of a dark circular structure in the epidermis which is most probably the boundary of the cross-section of the larva tunnel, but no imaging of the larvae itself. OCT images of patient 2 showed the similar cross-section of a presumed larva tunnel, but the delineation of the tunnel was not as clear as in Patient 1, probably due to collapse of the tunnel. In neither case was a possible larvae identified. A weakness of this study is that we did not biopsy the larva tunnels, which were however in good agreement with the known histology of this disease. Furthermore, the imaging of tissue with OCT does not necessarily simply reflect morphological changes visible in histopathological sections, but also reflects changes in tissue density, mechanics and optics, which are not visualized by histochemistry. The OCT images therefore describe additional and unique tissue characteristics.

OCT is analogue to B-mode ultrasound pulse-echo imaging with an optical rather than acoustical reflectivity being measured. However, OCT has a 10–100 fold higher resolution than ultrasound. In ultrasound the penetration depth goes down on behalf of increasing resolution, this is also the case in OCT, but importantly the resolution is also dependant on wavelength and bandwidth of the light source, opening new ways for improving high-resolution imaging of tissue. In our case, ultrasound imaging of the larva tunnel in Patient 1 did not reveal the larva tunnel, but demonstrated pathological changes in the epidermis. The two methods therefore appear to be complementary, rather than mutually exclusive.[21]

The larvae were not visualized in any of the patients, suggesting that the optical and ultrasonographical characteristics of the larval tissue mimic the optical properties of the skin closely. It is speculated that the optical properties of the parasite preclude positive identification of the animal in the skin.

References

1. Caumes E, Danis M. From creeping eruption to hookworm-related cutaneous larva migrans. *Lancet Infect Dis* 2004;**4**(11):659–60.
2. Habif TP. *Infestations and bites. Clinical dermatology—a color guide to diagnosis and therapy*, 4th ed. Philadelphia, USA: Mosby; 2004. p. 537.
3. Jelinek T, Maiwald H, Nothdurft HD, Loscher T. Cutaneous larva migrans in travelers: synopsis of histories, symptoms, and treatment of 98 patients. *Clin Infect Dis* 1994;**19**(6):1062–6.
4. Hotez PJ, Narasimhan S, Haggerty J, Milstone L, Bhopale V, Schad GA, et al. Hyaluronidase from infective Ancylostoma hookworm larvae and its possible function as a virulence factor in tissue invasion and in cutaneous larva migrans. *Infect Immun* 1992;**60**(3):1018–23.
5. Blackwell V, Vega-Lopez F. Cutaneous larva migrans: clinical features and management of 44 cases presenting in the returning traveller. *Br J Dermatol* 2001;**145**(3):434–7.
6. Elder D, Elenitsas R, Johnson Jr B, Jaworsky C. *Parasitic infestations of the skin*. Philadelphia, USA: Lippincott–Raven; 1997.
7. Sakai S, Shida Y, Takahashi N, Yabuuchi H, Soeda H, Okafuji T, et al. Pulmonary lesions associated with visceral larva migrans due to Ascaris suum or Toxocara canis: imaging of six cases. *Am J Roentgenol* 2006;**186**(6):1697–702.
8. Gambichler T, Moussa G, Sand M, Sand D, Altmeyer P, Hoffmann K. Applications of optical coherence tomography in dermatology. *J Dermatol Sci* 2005;**40**(2):85–94.
9. Pierce MC, Strasswimmer J, Park BH, Cense B, de Boer JF. Advances in optical coherence tomography imaging for dermatology. *J Invest Dermatol* 2004;**123**(3):458–63.
10. Olmedo JM, Warschaw KE, Schmitt JM, Swanson DL. Optical coherence tomography for the characterization of basal cell carcinoma in vivo: a pilot study. *J Am Acad Dermatol* 2006;**55**(3):408–12.
11. Tycho A, Andersen P, Thrane L, Jemec GBE. *Optical coherence tomography in dermatology. non-invasive methods and the skin*, 2nd ed. Boca Raton: CRC Press, Taylor & Francis Group; 2006 [Chapter 31].
12. Fujimoto JG. Optical coherence tomography for ultrahigh resolution in vivo imaging. *Nat Biotechnol* 2003;**21**(11):1361–7.
13. Gladkova ND, Petrova GA, Nikulin NK, Radenska-Lopovok SG, Snopova LB, Chumakov YP, et al. In vivo optical coherence tomography imaging of human skin: norm and pathology. *Skin Res Technol* 2000;**6**(1):6–16.
14. Welzel J. Optical coherence tomography in dermatology: a review. *Skin Res Technol* 2001;**7**(1):1–9.
15. Gambichler T, Kunzlberger B, Paech V, Kreuter A, Boms S, Bader A, et al. UVA1 and UVB irradiated skin investigated by optical coherence tomography in vivo: a preliminary study. *Clin Exp Dermatol* 2005;**30**(1):79–82.
16. Jemec GB, Gniadecka M, Ulrich J. Ultrasound in dermatology. Part I. High frequency ultrasound. *Eur J Dermatol* 2000;**10**(6): 492–7.
17. Veraldi S, Bottini S, Carrera C, Gianotti R. Cutaneous larva migrans with folliculitis: a new clinical presentation of this infestation. *J Eur Acad Dermatol Venereol* 2005;**19**(5):628–30.
18. Balfour E, Zalka A, Lazova R. Cutaneous larva migrans with parts of the larva in the epidermis. *Cutis* 2002;**69**(5):368–70.
19. Case 191. Spiruroid nematode larva migrans (creeping disease) [computer program]. 1012-6 Fukuda, Okayama 702-8021, Japan: Kurashiki Seminar of Diagnostic Pathology; 2006.
20. Welzel J, Lankenau E, Birngruber R, Engelhardt R. Optical coherence tomography of the skin. *Curr Probl Dermatol* 1998;**26**:27–37.
21. Holm EA, Wulf HC, Thomassen L, Jemec GB. Instrumental assessment of atopic eczema: validation of transepidermal water loss, stratum corneum hydration, erythema, scaling, and edema. *J Am Acad Dermatol* 2006;**55**(5):772–80.

Paper II

Nail thickness measurements using optical coherence tomography and 20-MHz ultrasonography

CLINICAL AND LABORATORY INVESTIGATIONS DOI 10.1111/j.1365-2133.2007.08118.x

Nail thickness measurements using optical coherence tomography and 20-MHz ultrasonography

M. Mogensen, J.B. Thomsen,* L.T. Skovgaard† and G.B.E. Jemec

Department of Dermatology, Roskilde Hospital, Koegevej 7-13, DK-4000 Roskilde, Denmark
Optics and Plasma Research Department, Risoe National Laboratory, Technical University of Denmark, Roskilde, Denmark
†*Department of Biostatistics, University of Copenhagen, Copenhagen, Denmark*

Correspondence
Mette Mogensen.
E-mail: rsmmog@ra.dk

Accepted for publication
24 May 2007

Key words
nail imaging, nail thickness, optical coherence tomography, ultrasound

Conflicts of interest
None declared.

Summary

Background Nail diseases are often troubling to the patient and may present a diagnostic challenge to the dermatologist. Biopsies from the nail may be required although often perceived uncomfortable by the patient and potentially scarring. Noninvasive technologies are therefore of particular interest in the study of nails. Optical coherence tomography (OCT) is an optical imaging modality which may provide improved data.

Objectives This study evaluates nail morphology and thickness in OCT images in comparison with high-frequency ultrasound (HFUS) imaging of the nail.

Methods Ten healthy volunteers were recruited for imaging and nail measurements; OCT and HFUS images were compared qualitatively. Nail thickness measurements with four different techniques were compared: ultrasound, OCT, polarization-sensitive (PS) OCT and callipers. The OCT system was developed at Risoe National Laboratory, Denmark. A commercially available 20-MHz ultrasound system (Dermascan; Cortex Technology, Hadsund, Denmark) was used.

Results In standard OCT the nail plate appeared as a layered structure containing a varying number of horizontal homogeneous bands of varying intensity and thickness. PS-OCT images of the nail plate also showed a layered structure. The refractive index of the nail was 1·47 ± 0·09. OCT and PS-OCT had low coefficients of variation, 6·31 and 6·53, respectively, compared with other methods: HFUS 12·70 and callipers 14·03.

Conclusion PS-OCT has to our knowledge not been applied to OCT analysis of the nail, and offers some advantages in separation of the nail bed from the nail plate.

Currently, nail disease diagnosis is based mainly on clinical examination although biopsies and scrapings can also provide significant information.[1–4] The nail bed can be inspected visually only partially, and pathologies of the nail bed may be either indistinct or hidden by the nail plate. In some cases a biopsy of the nail and underlying skin is therefore required. Nail biopsies, however, may be unpleasant to the patient, time-consuming and leave scarring and potentially permanent disfigurement of the nail. Objective and noninvasive assessment is therefore of particular interest in the study of nails.[5]

Pathology of the matrix is often reflected clinically as a deformation or change of colour of the nail plate. Noninvasive imaging technologies may facilitate differential diagnosis of pathologies in the nail unit and may delineate tumours.[5–15] It is well established that high-frequency ultrasound (HFUS) can be used for measuring nail thickness.[2,16–19] Other technologies such as magnetic resonance imaging (MRI),[9,12,13] confocal microscopy[20,21] and optical coherence tomography (OCT)[22,23] have also demonstrated potential in nail research. MRI has gained some ascendancy over the other methods.[13] The nail plate can be visualized with MRI if it is covered with, for example, petrolatum.

The aim of this pilot study was to investigate OCT characteristics of the nail as well as the potential of OCT for studies of the nail in comparison with 20-MHz HFUS and actual thickness measured with callipers.

Materials and methods

In this pilot study 10 healthy volunteers with no clinical signs or history of nail disease were recruited in accordance with the Helsinki II guidelines.

All 10 fingernails from the volunteers were examined clinically and by OCT, HFUS and calliper. The nails were photographed with a digital camera and the built-in camera of the OCT probe.

For refractive index calculation, nail samples were collected and imaged on a glass plate immediately after clipping to avoid drying and corresponding change in refractive index.

The OCT system was developed at Risoe National Laboratory, Denmark. OCT is a noninvasive optical imaging technology that provides cross-sectional, tomographic images of tissue *in situ* and in real time.[24] OCT can provide images of tissue pathology *in situ* with a high axial resolution.[24–26] The light source in our OCT system is a superluminescent diode with a centre wavelength of 1318 nm, and a bandwidth of 66 nm. Axial resolution of the system is 9 μm (in tissue), lateral resolution is 24 μm. OCT works in analogy to ultrasound; the reflection of infrared light (instead of acoustical waves) from the skin is measured and the intensity is imaged as a function of position. A low-power infrared light illuminates the tissue, and the signal obtained from the scan is amplified, demodulated and stored in a digital form. The image data are displayed by assigning colour or grey scales to each reflection according to the measured signal strength. Due to speed of light the optical echoes cannot be measured directly, therefore OCT is based on low-coherence interferometry, correlating backscattered light from tissue with light that has travelled a known reference path. The OCT probe sends infrared light onto the skin at optical power densities in compliance with American National Standards Institute safety regulations. The OCT probe is applied directly to the nail. The OCT scanning lasts only a few seconds, and does not cause discomfort to the subject studied.[27–29]

Characteristics other than the intensity of backscattered and reflected light can be imaged by OCT. Some tissues such as nail matrix, muscle and collagen are birefringent. In polarization-sensitive (PS) OCT images the characteristic birefringence of tissue is clear. In our OCT system PS-OCT images are recorded in parallel with standard OCT images.

Ultrasound examinations were carried out with a dedicated 20-MHz scanner (DermaScan Version C 3.1; Cortex Technology, Hadsund, Denmark) in B-mode scan. The scanner has an axial resolution of 50 μm, lateral 350 μm. Ultrasound has been shown to provide objective, accurate, noninvasive and easy measurements of several parameters of skin morphology and enables visualization of subclinical and deep lesions, and thus allows the identification of diameters and the depth of pathology such as inflammation, neoplasms and infestations.[30] Measurement of nail thickness was made by the integrated measurement menu in A-mode scan. Thickness was estimated using the system software. Ultrasound gel was applied to the nail prior to imaging.

Images of each nail were recorded with OCT and ultrasound. A cross-sectional scanning at the centre of the nail plate with OCT and ultrasonography was used for thickness measurements. Three cross-sectional thickness measurements were performed on each image; one in the centre of the image and two other measurements in the centre of a line drawn from the central measurement to the lateral nail border on the right and left side of the image (Fig. 1).

To determine absolute nail thicknesses using OCT, the refractive index of the nail has to be known. This is similar to ultrasound which requires knowledge of the speed of sound in the nail.[1,17,31] To measure the refractive index using the OCT system, the 'optical length shift method' was employed.[32,33] The method requires two OCT images of each clipped nail. An OCT image of the nail placed on top of a glass plate is compared with an OCT image of the

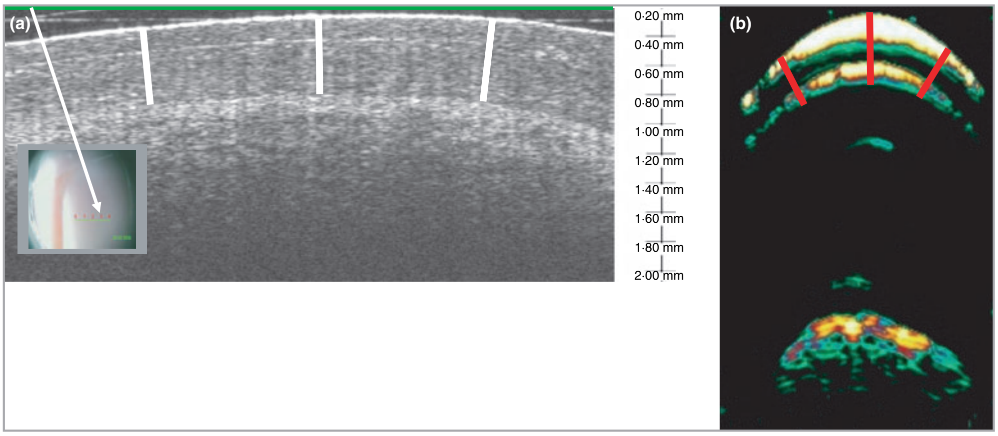

Fig 1. (a) Optical coherence tomography (OCT) image of a normal nail. Inserted image shows the video image of the nail from the probe. The green bar indicates the area on the skin where the OCT scan is recorded (white arrow). The green bar in OCT image reflects the small green bar. The white bars indicate where the measurements were made. (b) A 20-MHz ultrasound (UL) image of the same nail as in (a). Red bars indicate where the measurements were made. The intense signal below the nail is the distal phalangeal bone.

glass plate without the nail. By registration of the optical thickness of the nail and the displacement of the glass plate between the two images it is possible to extract the refraction index of the nail.

Software for determination of nail thickness using OCT images was developed.

We used a digital calliper (LiMit, Auckland, New Zealand). Three thickness measurements were performed at the distal, free end of the nail plate on each finger. Measurements with a calliper were made at the centre of the free nail plate and approximately 3–4 mm to the left and to the right of the centre.

Statistics

We analysed each method separately, using a variance component model on the logarithmically transformed measurements. The model included a systematic difference between the 10 fingers as well as random variation between individuals, between fingers of the same individual and between measurements on the same finger. The variance components corresponding to these sources of random variation were subsequently used for calculation of coefficients of variation, in particular the reproducibility of each method. SAS 9.1 statistical software was used.

Results

The volunteers were all white, three men and seven women, mean age 35·4 years (range 26–51). All measurements were performed by the same doctor (M.M.), and were carried out consecutively during 2 weeks in March 2006.

Nail morphology in optical coherence tomography images

OCT provided images of the nail plate, the nail bed and the matrix to a depth of 2 mm. Images were 4 mm wide. In standard OCT the nail plate appeared as a layered structure containing a varying number of horizontal homogeneous bands of varying intensity and thickness. The lunula and leuconychia contained distinct horizontal white bands: at the deep end of the nail plate, and within the nail plate, respectively. These parts of the nail are strongly reflective/backscattering; this also explains the white colour seen with the naked eye. OCT and PS-OCT images of a leuconychia, lunula and normal nail are demonstrated in Figure 2.

In general the nail plate was not easy to distinguish from the nail bed in OCT images. We defined the border between nail plate and nail bed as the first change in OCT image intensity after the entrance signal. Nail OCT images showed a very

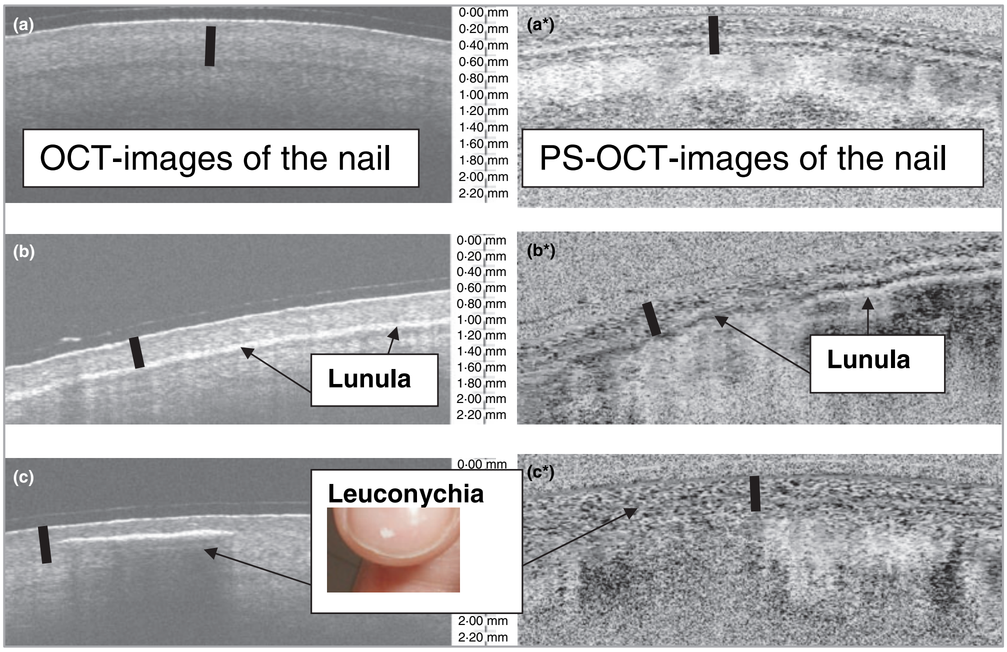

Fig 2. The left hand side shows optical coherence tomography (OCT) images of a normal nail (a), the lunula (b) and a leuconychia (c); a small photograph of the nail with leuconychia is inserted. On the right hand side are the structures reflected as polarization-sensitive (PS) OCT images, marked by an asterisk. The black bars indicate the thickness of the nail.

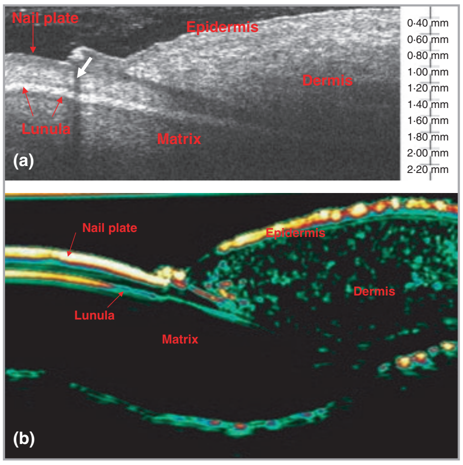

Fig 3. (a) Optical coherence tomography (OCT) image of the matrix; the layered structure of the nail plate is seen. The lunula is reflected as a white band that fades away in the matrix. The overlying epidermis and dermis decreases the signal from the matrix. Under the cuticle a black shadow is seen (white arrow) due to the hyper-reflective quality of a hyperkeratosis. In the ultrasound image (b) the matrix is hypoechoic. The ventral and dorsal nail plates are separated, and the epidermis is more echogenic than the dermis.

characteristic structure in PS images due to the arrangement of the dorsal and ventral nail plates containing birefringent collagen structures. PS-OCT imaging separated the nail structure more clearly from the nail bed due to the change in polarization from nail plate to nail bed. Figure 1 illustrates the nail morphology in OCT and ultrasound images. The nail thickness measurements are indicated by bars. The matrix is shown by OCT and ultrasound in Figure 3.

Nail morphology in ultrasound images

In ultrasound images the nail is separated into two overlaying plates. The dorsal and ventral nail plates can be seen as laminar hyperechoic (white) parallel bands with a virtual hypoechoic (black) space between them. The nail bed appears as the hypoechoic region under the plates. Below the two nail plates the distal phalanx is seen. Just as in OCT imaging the matrix can be visualized as a more signal-intense (echoic) area.

Refractive index

We included finger nails from four human volunteers and carried out five measurements on each nail and five measurements of the glass plate without the nail. By comparing the optical thickness of the nail and the displacement of the glass plate between the two images the refraction index of the nail was calculated to be 1·47 ± 0·09. This method itself can measure the refractive index with an uncertainty of 1–2%.

Nail thickness

Thickness average from identical fingers in all 10 persons ranges from 0·63 ± 0·10 mm with OCT and 0·52 ± 0·08 mm with PS-OCT (finger 1) to 0·41 ± 0·07 mm with OCT and 0·38 ± 0·05 mm with PS-OCT (finger 5). Thickness measurements for fingers 1 and 4 are shown in Table 1. Due to limited space data are not shown from all 10 fingers.

Nail thickness statistical analysis

The various measurement methods are linearly related, but the differences between them cannot be described either as a constant difference or as a proportionality factor. We have therefore focused on a comparison between their reproducibility as well as their ability to discriminate between different fingers and/or persons. The reproducibility is quantified as the coefficient of variation between the three measurements on the same nail, and a small coefficient of variation means that the method has a high reproducibility. The figures are reported in Table 2 and show that OCT and PS-OCT both have low coefficients of variation, 6·31 and 6·53, respectively, whereas the calliper has the highest coefficient of variation, 14·03.

The coefficients of variation between persons are shown in the second column of Table 2. These have to be high, corresponding to a good ability to detect actual differences. However, they will be influenced by the coefficient of variation due to reproducibility, so we have also added a column with hypothetical coefficients of variation between subjects, had there been no measurement error whatsoever. This column shows the OCT method to be superior to the others.

Discussion

We have found OCT imaging of the nail easy to apply. OCT images of the nail reflect the anatomical architecture of the nail unit: the layered structure of the nail plate, the upper 1–2 mm of the epidermis and dermis and the structure of the matrix below the proximal nail plate. These structures can also be imaged by HFUS, but because OCT has higher resolution than HFUS, it has an ability to discriminate subtle changes not detected by ultrasound, and thus provide more information about the nail unit. The optical contrast of the skin and the nail unit may, however, also be more prominent using infrared light rather than sound waves, and thereby contribute to better resolution imaging. We have also shown the ability of OCT imaging to visualize the lunula and leuconychia clearly because of increased reflection/backscattering of these areas.

It was possible to measure nail plate thickness using OCT, although some variation was seen in nail thickness measurements between different methods (Table 1).

Both OCT and PS-OCT have low coefficients of variation between measurements on the same nail compared with HFUS and digital calliper. OCT furthermore appears to have the highest ability to distinguish nail thickness in the thumb compared

Table 1 Data from measurements of nail thickness in fingers 1 and 4 with all four methods presented as the range of measurements in mm. Data from fingers 2, 3 and 5 are not shown. The corresponding author will provide the full data material on demand

	Finger 1	Finger 1	Finger 1	Finger 1	Finger 4	Finger 4	Finger 4	Finger 4
Individual no.	Calliper	HFUS	OCT	PS-OCT	Calliper	HFUS	OCT	PS-OCT
1 dex	0·36	0·47	0·48	0·48	0·35	0·37	0·30	0·34
1 sin	0·52	0·43	0·57	0·37	0·33	0·38	0·35	0·36
2 dex	0·56	0·46	0·55	0·57	0·46	0·29	0·27	0·28
2 sin	0·80	0·45	0·55	0·44	0·45	0·37	0·32	0·32
3 dex	0·73	0·55	0·71	0·67	0·60	0·46	0·45	0·42
3 sin	0·54	0·52	0·73	0·61	0·64	0·49	0·48	0·38
4 dex	0·69	0·46	0·58	0·53	0·69	0·36	0·57	0·55
4 sin	0·67	0·46	0·58	0·55	0·56	0·37	0·38	0·35
5 dex	0·72	0·39	0·57	0·43	0·62	0·41	0·33	0·38
5 sin	0·67	0·42	0·78	0·38	0·56	0·34	0·44	0·37
6 dex	0·88	0·41	0·72	0·62	0·46	0·44	0·49	0·36
6 sin	0·83	0·43	0·53	0·46	0·54	0·41	0·47	0·43
7 dex	0·70	0·56	0·75	0·60	0·54	0·42	0·67	0·50
7 sin	0·66	0·49	0·86	0·61	0·52	0·41	0·55	0·51
8 dex	0·56	0·47	0·63	0·57	0·51	0·42	0·49	0·43
8 sin	0·55	0·47	0·59	0·54	0·57	0·41	0·45	0·42
9 dex	0·58	0·47	0·55	0·46	0·61	0·39	0·42	0·39
9 sin	0·46	0·46	0·55	0·56	0·48	0·39	0·43	0·38
10 dex	0·44	0·43	0·65	0·46	0·53	0·39	0·42	0·38
10 sin	0·39	0·43	0·62	0·48	0·63	0·39	0·42	0·43
Range	0·36–0·88	0·39–0·56	0·48–0·86	0·37–0·67	0·33–0·69	0·29–0·49	0·27–0·67	0·28–0·55

dex, dexter; sin, sinister; HFUS, high-frequency ultrasound; OCT, optical coherence tomography; PS, polarization-sensitive.

Table 2 Coefficients of variation. All numbers are percentages of the thickness measurements. Percentage variation is variation other than the systematic thickness difference between nails

		Hypothetical	
Method	Residual–s	Person–s	Person–s-mod
1 OCT	6·3103	15·6563	14·3283
2 PS-OCT	6·5261	12·2674	10·3875
3 Ultrasound	12·6965	14·5647	7·1365
4 Calliper	14·0250	18·0278	11·3270

Residual–s, same finger, repeated measurements. A low number means advantage over other methods. Person–s, same finger type in different persons. Person–s-mod, like person–s it represents variation between persons, but modified to an ideal situation without variation between measurements. A high number means advantage over other methods. OCT, optical coherence tomography; PS, polarization sensitive.

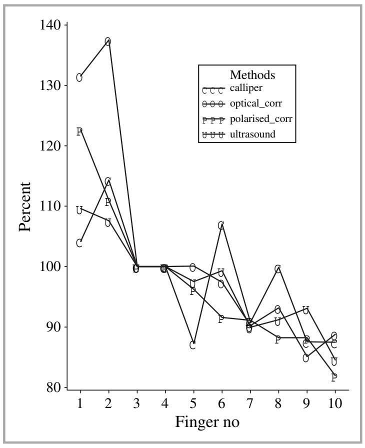

Fig 4. Percentage variation of all measurement methods compared with finger 2. Numbers 1–10 correspond to 1 = finger 1 dexter (dex); 2 = finger 1 sinister (sin); 3 = finger 2 dex; 4 = finger 2 sin, etc. O, optical coherence tomography; P, polarization-sensitive OCT; U, ultrasound; C, calliper.

with the other methods. In the statistical analysis it has been considered that measurements are performed on different scales. However, a good reproducibility is not enough; if the method results in the same value even if used on different fingers or persons, it will be worthless. Therefore, we also estimated the ability of each method to detect differences between different finger types (e.g. difference between thumb and ring finger) as well as the coefficients of variation corresponding to measurements on the same type of finger (e.g. right thumb) but on different persons (Table 2). Figure 4 shows the estimated percentage thickness of all finger nails compared with finger 2. We note that all methods differentiate almost equally well except for the thumb where the OCT method detects a larger discrepancy than any of the other methods. This may be explained by the higher resolution of OCT.

Ultrasound images of the nail and thickness measurements were in accordance with other studies on nail anatomy and nail thickness in healthy nails. Using HFUS ($n = 10$) we measured a nail thickness of 0·46 ± 0·04 mm (thumb). Jemec[3] ($n = 15$) found a nail thickness of 0·593 ± 0·118 mm (thumb), and in another study[17] ($n = 21$) 0·56 mm (range 0·42–0·80) and Wollina *et al.*[18] ($n = 34$) reported nail thicknesses of 0·481 mm (thumb) and 0·397 mm (left fifth finger). Finlay *et al.* found similar results.[1,16] The refractive index of the nail was 1·47 ± 0·09 which is in accordance with the refractive index and standard deviation measured by Ohmi *et al.*[34]

Ultrasound measures a slightly broader area of the nail, which will tend to increase variation in measurements. The calliper probably has the highest coefficient of variation because it tends to randomly grip the hyponychium, and thereby falsely increases nail thickness.[3] Our results are promising for the use of OCT in nail anatomy and thickness measurements as it seems to have some benefits over ultrasound, i.e. better ability to differentiate morphological details and nail thickness. This is most likely because of the increased resolution of OCT. PS-OCT seems to offer some advantages in separation of the nail bed from the nail plate. PS-OCT has to our knowledge not been applied to OCT analysis of the nail before. However the coefficient of variation is similar to OCT, and not higher as could be expected.

In differentiation of tumours of the nail unit, both OCT and PS-OCT may also have a special potential, because of the ability of PS-OCT to distinguish birefringent tissue. Skin tumours, for example, have been shown to have less birefringence than normal tissue.[29,35,36] Doppler OCT may in the future add useful new information about vascular tumours in the nail apparatus. Doppler ultrasound has been demonstrated useful in differentiating subungual glomus tumours.[6,14] Likewise MRI has been demonstrated to have a potential in differentiating various tumours of the nail unit.[13] OCT has a resolution approximately 20-times higher than MRI, but a lower penetration depth; hence, OCT and MRI are not always mutually exclusive.

OCT is well established in ophthalmology, which to our knowledge is the only field where OCT has been compared with HFUS for thickness measurements.[37–39] Thickness of the cornea was studied in central corneal grafts ($n = 41$);[38] the values obtained with OCT were similar to those obtained with a contact ultrasound pachymeter. The average coefficient of variation of the central corneal graft thickness was low with both pachymeters. In some cases of lamellar keratoplasty, the corneal refractive index could change at the interface level that could affect OCT measurements. In our case, changes of the refractive index in a normal nail were not suspected. In general the studies comparing OCT with HFUS find that the methods are comparable with low coefficients of variation. The ultrasound system (pachymeters) applied however had a higher resolution than in this study. This may explain why we found a lower coefficient of variation for OCT and PS-OCT.

In conclusion, the use of a noninvasive method such as OCT for the study of the human nail offers several advantages over existing research methodology. Quantitative OCT allows more precise assessment of biological changes in the nail unit, it allows for longitudinal studies, quantification of subsurface structures and has a high resolution.

References

1 Finlay AY, Western B, Edwards C. Ultrasound velocity in human fingernail and effects of hydration: validation of *in vivo* nail thickness measurement techniques. *Br J Dermatol* 1990; **123**:365–73.

2 Jemec GB, Serup J. Ultrasound structure of the human nail plate. *Arch Dermatol* 1989; **125**:643–6.

3 Jemec G. Measurement of nail thickness. In: *Handbook of Non-Invasive Methods and the Skin* (Serup J, Jemec J, Grove G, eds), 2nd edn. Boca Raton, FL: CRC Press, 2006; 923–5.

4 de Berker D. Methods for nail assessment: an overview. In: *Handbook of Non-Invasive Methods and the Skin* (Serup J, Jemec J, Grove G, eds), 2nd edn. Boca Raton, FL: CRC Press, 2006; 911–18.

5 Wortsman X, Jemec GB. Ultrasound imaging of nails. *Dermatol Clin* 2006; **24**:323–8.

6 Chen SH, Chen YL, Cheng MH *et al.* The use of ultrasonography in preoperative localization of digital glomus tumors. *Plast Reconstr Surg* 2003; **112**:115–19.

7 Drape JL. Imaging of the tumors of the perionychium. *Hand Clin* 2002; **18**:655–70.

8 Drape JL. Imaging of tumors of the nail unit. *Clin Podiatr Med Surg North Am* 2004; **21**:493–511.

9 Goettmann S, Drape JL, Idy-Peretti I *et al.* Magnetic resonance imaging: a new tool in the diagnosis of tumours of the nail apparatus. *Br J Dermatol* 1994; **130**:701–10.

10 Kaufman SC, Beuerman RW, Greer DL. Confocal microscopy: a new tool for the study of the nail unit. *J Am Acad Dermatol* 1995; **32**:668–70.

11 Ogino T, Ohnishi N. Ultrasonography of a subungual glomus tumour. *J Hand Surg (Br)* 1993; **18**:746–7.

12 Opdenakker G, Gelin G, Palmers Y. MR imaging of a subungual glomus tumor. *AJR Am J Roentgenol* 1999; **172**:250–1.

13 Richert B, Baghaie M. Medical imaging and MRI in nail disorders: report of 119 cases and review of the literature. *Dermatol Ther* 2002; **15**:159–64.

14 Takemura N, Fujii N, Tanaka T. Subungual glomus tumor diagnosis based on imaging. *J Dermatol* 2006; **33**:389–93.

15 Theumann NH, Goettmann S, Le VD *et al.* Recurrent glomus tumors of fingertips: MR imaging evaluation. *Radiology* 2002; **223**:143–51.

16 Finlay AY, Moseley H, Duggan TC. Ultrasound transmission time: an *in vivo* guide to nail thickness. *Br J Dermatol* 1987; **117**:765–70.

17 Jemec GB, Agner T, Serup J. Transonychial water loss: relation to sex, age and nail-plate thickness. *Br J Dermatol* 1989; **121**:443–6.

18 Wollina U, Berger M, Karte K. Calculation of nail plate and nail matrix parameters by 20 MHz ultrasound in healthy volunteers and patients with skin disease. *Skin Res Technol* 2001; **7**:60–4.

19 Wortsman XC, Holm EA, Wulf HC *et al.* Real-time spatial compound ultrasound imaging of skin. *Skin Res Technol* 2004; **10**:23–31.

20 Gupta AK, Ryder JE, Summerbell RC. Onychomycosis: classification and diagnosis. *J Drugs Dermatol* 2004; **3**:51–6.

21 Hongcharu W, Dwyer P, Gonzalez S *et al.* Confirmation of onychomycosis by *in vivo* confocal microscopy. *J Am Acad Dermatol* 2000; **42**:214–16.

22 Vogt M, Knuttel A, Hoffmann K *et al.* Comparison of high frequency ultrasound and optical coherence tomography as modalities for high resolution and non invasive skin imaging. *Biomed Tech (Berl)* 2003; **48**:116–21.

23 Welzel J, Lankenau E, Birngruber R *et al.* Optical coherence tomography of the human skin. *J Am Acad Dermatol* 1997; **37**:958–63.

24 Fujimoto JG. Optical coherence tomography for ultrahigh resolution *in vivo* imaging. *Nat Biotechnol* 2003; **21**:1361–7.

25 Gladkova ND, Petrova GA, Nikulin NK *et al. In vivo* optical coherence tomography imaging of human skin: norm and pathology. *Skin Res Technol* 2000; **6**:6–16.

26 Welzel J. Optical coherence tomography in dermatology: a review. *Skin Res Technol* 2001; **7**:1–9.

27 Gambichler T, Moussa G, Sand M *et al.* Applications of optical coherence tomography in dermatology. *J Dermatol Sci* 2005; **40**:85–94.

28 Olmedo JM, Warschaw KE, Schmitt JM *et al.* Optical coherence tomography for the characterization of basal cell carcinoma *in vivo*: a pilot study. *J Am Acad Dermatol* 2006; **55**:408–12.

29 Pierce MC, Strasswimmer J, Park BH *et al.* Advances in optical coherence tomography imaging for dermatology. *J Invest Dermatol* 2004; **123**:458–63.

30 Jemec GB, Gniadecka M, Ulrich J. Ultrasound in dermatology. Part I. High frequency ultrasound. *Eur J Dermatol* 2000; **10**:492–7.

31 Johnson M, Shuster S. Determinants of nail thickness and length. *Br J Dermatol* 1994; **130**:195–8.

32 Kim YL, Walsh JT Jr, Goldstick TK *et al.* Variation of corneal refractive index with hydration. *Phys Med Biol* 2004; **49**:859–68.

33 Wang X, Zhang C, Zhang L *et al.* Simultaneous refractive index and thickness measurements of bio tissue by optical coherence tomography. *J Biomed Opt* 2002; **7**:628–32.

34 Ohmi M, Ohnishi Y, Yoden K, Haruna M. *In vitro* simultaneous measurement of refractive index and thickness of biological tissue by the low coherence interferometry. *IEEE Trans Biomed Eng* 2000; **47**:1266–70.

35 Strasswimmer J, Pierce MC, Park B *et al.* Characterization of basal cell carcinoma by multifunctional optical coherence tomography. *J Invest Dermatol* 2003; **121**:0156 [Abstr.].

36 Strasswimmer J, Pierce MC, Park BH *et al.* Polarization-sensitive optical coherence tomography of invasive basal cell carcinoma. *J Biomed Opt* 2004; **9**:292–8.

37 Airiani S, Trokel SL, Lee SM *et al.* Evaluating central corneal thickness measurements with noncontact optical low-coherence reflectometry and contact ultrasound pachymetry. *Am J Ophthalmol* 2006; **142**:164–5.

38 Gaujoux T, Borderie VM, Yousfi H *et al.* Comparison of optical low-coherence reflectometry and ultrasound pachymetry in measuring corneal graft thickness. *Cornea* 2007; **26**:185–9.

39 Much MM, Haigis W. Ultrasound and partial coherence interferometry with measurement of central corneal thickness. *J Refract Surg* 2006; **22**:665–70.

Paper III

In vivo thickness measurement of basal cell carcinoma and actinic keratosis with optical coherence tomography and 20-MHz ultrasound

DERMATOPATHOLOGY BJD British Journal of Dermatology

In vivo thickness measurement of basal cell carcinoma and actinic keratosis with optical coherence tomography and 20-MHz ultrasound

M. Mogensen, B.M. Nürnberg,* J.L. Forman,† J.B. Thomsen,‡ L. Thrane‡ and G.B.E. Jemec

*Departments of Dermatology, *Pathology and †Biostatistics, Faculty of Health Sciences, University of Copenhagen, Roskilde Hospital, Koegevej 7–13, DK-4000 Roskilde, Denmark*
‡DTU Fotonik, Department of Photonics Engineering, Technical University of Denmark, Copenhagen, Denmark

Correspondence
Mette Mogensen.
E-mail: mmg@regionsjaelland.dk

Accepted for publication
21 October 2008

Key words
actinic keratosis, basal cell carcinoma, diagnostic imaging, high-frequency ultrasound, optical coherence tomography, tumour thickness

Conflicts of interest
None declared.

DOI 10.1111/j.1365-2133.2008.09003.x

Summary

Background Accurate assessment of tumour size is important when planning treatment of nonmelanoma skin cancer (NMSC). Imaging with optical coherence tomography (OCT) has the potential to diagnose and measure depth of NMSC.

Objectives To compare accuracy of mean tumour thickness measurement in NMSC tumours < 2 mm of depth using OCT and 20-MHz high-frequency ultrasound (HFUS). In addition, OCT morphology of NMSC was studied in OCT images and the influence of histological and colorimetric values on the quality and penetration depth in OCT images was estimated.

Methods In total, 93 patients were scanned and 34 lesions [23 basal cell carcinoma (BCC) and 11 actinic keratosis (AK) lesions] < 2 mm thick and easily identified in OCT images were studied. OCT and HFUS were compared with biopsies. The influence of skin pigmentation and infiltration analgesia on OCT image quality was studied. Skin colour was measured with a colorimeter.

Results OCT presented narrower limits of agreement than HFUS. Both methods overestimated thickness but OCT was significantly less biased (0·392 mm vs. 0·713 mm). No relation between OCT penetration depth and skin colour was found.

Conclusions OCT appears more precise and less biased than HFUS for thickness measurement in AK and BCC lesions < 2 mm, but both OCT and especially HFUS tended to overestimate tumour thickness.

Nonmelanoma skin cancer (NMSC) is the most prevalent cancer in light-skinned populations.[1] In addition to other NMSC prognostic factors such as tumour diameter and perineural invasion,[2,3] tumour thickness has been speculated to have a prognostic role in NMSC as is the case in malignant melanoma.[4,5] The introduction of noninvasive treatments for superficial basal cell carcinoma (BCC) and actinic keratosis (AK) with, for example, 5-fluorouracil,[6] imiquimod,[7–9] 3% diclofenac gel[10] and photodynamic therapy (PDT)[11–13] has further highlighted the need for pretherapeutic tumour thickness assessments, as these treatments may be most suitable for thin lesions. Clinical thickness, atypia and lesion depth were significant predictors of the response at 3 months to methylaminolaevulinate-based PDT in a study of 112 lesions of squamous cell carcinoma (SCC) and Bowen's disease.[14] Another study also demonstrated that BCC thickness measured with high-frequency ultrasound (HFUS) before PDT predicted the probability of local recurrence 1 year after PDT treatment.[15] Yet another study emphasized the difficulty of aminolaevulinic acid (ALA) penetration into hyperkeratotic AK lesions, and demonstrated that sufficient ALA penetration to a depth of 1·0 mm was possible using patch-based delivery methods, further emphasizing the role of tumour thickness in NMSC treatment.[16] Imaging may also be useful in the lateral delineation which is important in surgery, PDT or radiotherapy of NMSC.

Clinically this can be difficult, and two studies[17,18] found an overall rate of incomplete excision of 11·2% in BCC and 6·3% in SCC, indicating a potential application for noninvasive imaging techniques. In the case of field cancerization, neither vertical nor horizontal clinical delineation is possible. At the same time, it is exactly in these cases where an accurate noninvasive diagnostic technique capable of easy bedside assessment would assist treatment planning, especially for AK[19] and superficial BCC.[20,21]

Improved imaging of skin tumours is therefore of clinical interest. Two methods have the necessary penetration depth of tissue to be potentially useful in the diagnosis, delineation and monitoring of NMSC noninvasively.[22] Optical coherence tomography (OCT) has been applied in several studies of NMSC[23–31] with promising results. A study compared OCT measurement of maximal depth in superficial BCC with histological depth and found excellent agreement in 20 lesions.[20] HFUS is another noninvasive tool for measurement of skin morphology, capable of identification and quantification of pathology such as inflammation and neoplasms.[32–34] A potential for NMSC delineation and diagnosis has been shown in several studies.[33,35,36]

The primary aims of this study were to compare accuracy of mean tumour thickness measurements in AK and BCC lesions < 2 mm of depth using 20-MHz HFUS and OCT. In addition, the role of skin pigmentation and infiltration analgesia on OCT image quality was studied.

Materials and methods

Patients

This study included 93 patients scanned by OCT and HFUS with histologically verified BCC and AK with one lesion each (31 AK, 62 BCC). Patients comprised 49 women and 44 men, were caucasian, and had a mean age of 70·6 years (range 37–90). All OCT and HFUS scans and measurements were performed by the same investigator (M.M.), and the OCT measurements (on the same images) were repeated by J.B.T. The study was conducted in accordance with Helsinki II and was approved by the Local Ethics Committee (ref. no. 2005–1–41). Biopsy, OCT and HFUS imaging of NMSC lesions were performed in a previously marked area of the lesion and imaging was also done on adjacent normal skin.

Optical coherence tomography system

OCT is an optical method analogous to ultrasound. It measures reflection of infrared radiation from the skin, instead of acoustic waves, and the signal strength is mapped as a function of position.[37] The OCT system used was developed at the Technical University of Denmark. The OCT probe is applied directly to the skin, using ultrasound gel as an optical coupling medium to improve image quality.[38] Infrared radiation used by OCT lies in the 'optical window'[39] where the radiation is least scattered and absorbed compared with other wavelengths. The radiation source is a super luminescent diode with a centre wavelength of 1318 nm. Axial resolution is 8 μm, and lateral resolution is 24 μm. The maximal penetration depth in skin is 2·0–2·5 mm, and therefore only NMSCs with thickness < 2 mm were included. The scanning lasts a few seconds and the probe records a digital photograph of the lesion simultaneously.

Only 34 of 93 (37%) of OCT-scanned NMSC lesions, 23 BCC and 11 AK lesions, were < 2 mm in depth in histology sections and could easily be identified in OCT images. In the 34 OCT images tumour depth was measured twice with the integrated software tool. The two thickness measurements were performed at the deepest point of the OCT image where an obvious shift in intensity from NMSC lesion to normal epidermis/dermis was identified. Maximal OCT penetration depth was defined as the lowest level of intense OCT signal in the image. Only OCT images without motion artefacts, hyperintense surface reflection or hairs creating large shadow artefacts were used. We included only OCT images that were imaged exactly where the subsequent biopsy was taken. In total, 22 of 93 (24%) images were discarded due to artefact or misalignment. In the remaining 37 of 93 (40%) NMSC lesions the lower border or general delineation could not be identified, or lesions exceeded 2 mm in maximal vertical tumour thickness, leaving 34 of 93 lesions for the study. The definition of the lower tumour border can be vague, and to study the subjectivity of thickness measurement using OCT we estimated interobserver agreement.

Optical coherence tomography morphology of nonmelanoma skin cancer

All 93 lesions were included in the morphological description of OCT images. In previous studies OCT images of BCC and AK generally demonstrated loss of normal layered skin architecture. Features like dark lobules surrounded by white stroma in BCC, and thickening of as well as dark bands in epidermis (AK)[26–28] have been described. We studied the morphology of BCC and AK in OCT images, and it was speculated that the swelling of the tissue following infiltration analgesia would affect the OCT image quality negatively.

High-frequency ultrasound imaging of nonmelanoma skin cancer

In HFUS images skin tumours generally appear as a homogeneous echo-poor area in comparison with the surrounding echo-rich dermis. We used a 20-MHz scanner (DermaScan Ver. C 3.1; Cortex Technology, Hadsund, Denmark) in B-mode scan. The scanner has an axial resolution of 50 μm, lateral 350 μm. Tumour depth measurement from HFUS images is done using the integrated ruler based on A-scans, and was performed twice in each lesion.

Colour measurement

Skin colour was measured in L*a*b* values using a tristimulus colorimeter: Chroma Meter CR-400 M (Minolta, Osaka, Japan). L* represents brightness, a* redness and b* colour on a blue and yellow scale. Skin colour was measured on the inner aspect of the upper arm and centrally on the cheek, carefully avoiding inclusion of pigmented lesions in the scan. We studied 76 patients with facial lesions (76 of the 93 patients included). The potential predictors were: age, sex, skin colour and the L*a*b* values: L* inner arm, L* cheek, a* inner arm and a* cheek were used. It was hypothesized that intense skin pigmentation could affect the OCT images due to high absorption/scattering, leading to a more shallow penetration depth in OCT images of dark skin. Fitzpatrick skin type was recorded for all patients.

Histopathology

Immediately after scanning a 3–4 mm punch biopsy was taken from the previously marked area. All biopsy specimens were stained with haematoxylin and eosin. Maximal vertical thickness was measured from the top of the stratum corneum to the deepest identifiable tumour cell aggregates.

Statistics

All tumours were measured in micrometres. Summary statistics for the HFUS, OCT and histology measurements are reported in Table 1. Agreement between histology and

Table 1 Summary of tumour thickness measurement from 34 tumours using optical coherence tomography (OCT), 20-MHz high-frequency ultrasound (HFUS) and histopathology

Measurement method	Mean ± SD thickness (μm)	Lower limit of agreement (μm)	Upper limit of agreement (μm)	P-value
Histology	821 ± 470	NA	NA	NA
OCT	1096 ± 352	−522·9	1072·1	0·0003
20-MHz HFUS	1552 ± 722	−719·4	2180·6	0·0000

Limits of agreement are given as 95% prediction intervals for the difference between OCT or HFUS and the reference, histology. NA, not applicable.

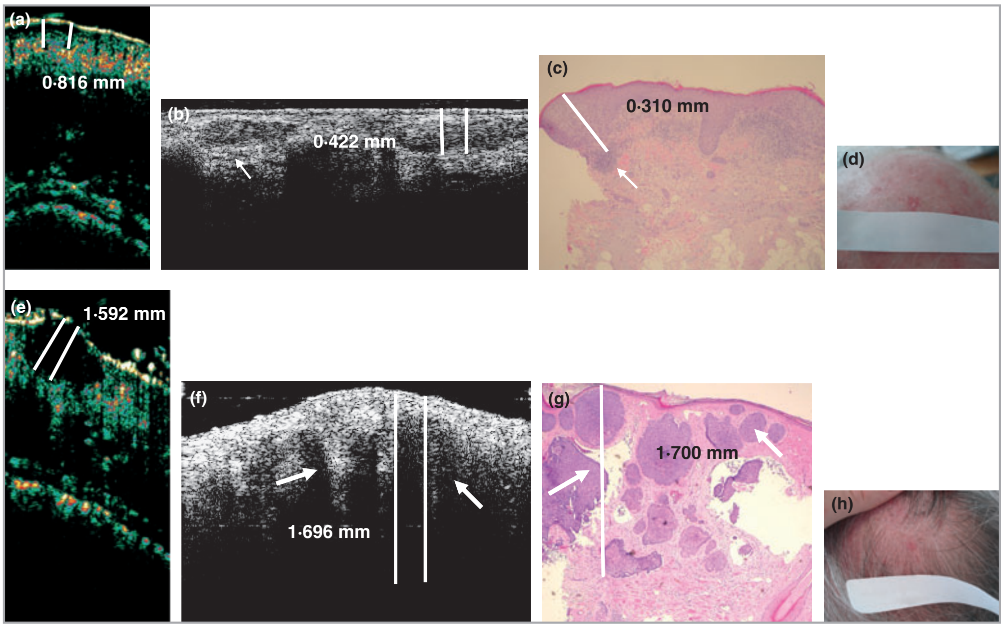

Fig 1. Agreement between optical coherence tomography (OCT), 20-MHz high-frequency ultrasound (HFUS) imaging and histology in two lesions from the study: an actinic keratosis (AK, a–d) and a basal cell carcinoma (BCC, e–h). The repeated thickness measurements performed are indicated by white lines. The actual thickness measure is shown next to the lines. In HFUS the AK lesion appears hypoechogenic (a). (b) An OCT image of the same AK. This particular AK lesion is surrounded by a white core (thin arrow), which is more commonly seen in BCC lesions. In this case it represents inflammation, seen in (c), the histopathology image of the lesion (haematoxylin and eosin, HE). (d) Clinical photograph of the same lesion. Break-up of layering is seen in both OCT images of lesions. (e) The BCC lesion appears well defined and hypoechogenic. (f) An OCT image of the BCC; the dark areas represent the basaloid cells (white arrows), and the same areas are indicated in (g), the histopathology image of the lesion (HE stain). (h) Clinical photograph of the same lesion.

HFUS/OCT was analysed in Bland–Altman plots and reported as limits of agreement (i.e. prediction intervals, which adjust the normal region for the parameter uncertainty caused by the small sample size). Interobserver agreement was estimated by the intratumour thickness correlation coefficient. Multiple regression analysis was applied to skin colour and OCT penetration depth data. $P < 0{\cdot}05$ was considered statistically significant. Fractal diagrams (QQ plots) were used to assess normal distribution of data. The statistical analysis was performed in Excel and in SAS version 9.1 (SAS Institute, Cary, NC, U.S.A.).

Results

Optical coherence tomography morphology of nonmelanoma skin cancer

In OCT images of BCC we identified the carcinoma cell clusters as well-defined dark (grey to black) rounded areas (Figs 1f, 2a, b). These areas were sometimes surrounded by a white border representing the tumour stroma (Fig. 2a, b). Focal disruptions of epidermis were common, and in OCT images of AK white dots and streaks were demonstrated in the upper epidermis (Figs 1b, 2c). The histological equivalents of white dots and streaks were dense, hyperkeratotic areas. OCT images of normal skin reflected the well-known layered architecture of the skin (not shown). In Figure 1 the OCT and HFUS morphology and thickness measurement of a BCC and an AK are presented with histopathology images (Fig. 1c, g) and clinical photographs (Fig. 1d, h). Figure 2 shows how two nodular BCC lesions (Fig. 2a, b) can look perfectly well defined in the OCT image, but come out much thicker in histology. A characteristic AK lesion that was overestimated by OCT is shown in Figure 2c. Figure 3 shows blurring of the outline of a BCC after the injection of 1% lignocaine with adrenaline making thickness measurements impossible.

High-frequency ultrasound morphology of nonmelanoma skin cancer

In HFUS images both AK and BCC lesions were identified as hyporeflective, round to oval structures (Fig. 1a, e), and a sharp border between the base of the hyporeflective tumour and the surrounding echo-rich dermis was identified in most lesions. In all HFUS images there was a strong entrance echo often tending to obscure the epidermis.

Mean tumour thickness

The 34 lesions (23 BCC and 11 AK lesions) were measured twice with OCT, twice with 20-MHz HFUS and once in histology. The two repeated thickness measurements using OCT and HFUS, respectively, were highly concordant (correlation coefficients 0·9929 and 0·9930) and thus their means were compared with histology. OCT and in particular HFUS appeared to overestimate tumour thickness as shown in Figure 4 where the mean thickness measurements from each tumour using HFUS (Fig. 4a) and OCT (Fig. 4b) are plotted against histology thickness. In both cases a statistically significant difference were found; see Table 1 for tumour thickness data and P-values. When HFUS was compared with histology it presented wider limits of agreement than OCT, as is illustrated in the Bland–Altman plots in Figure 5. The bias was significantly lower when OCT was compared with histology (Fig. 5b) than when HFUS was compared with histology (Fig. 5a), with bias 0·392 mm vs. 0·713 mm ($P < 0{\cdot}001$).

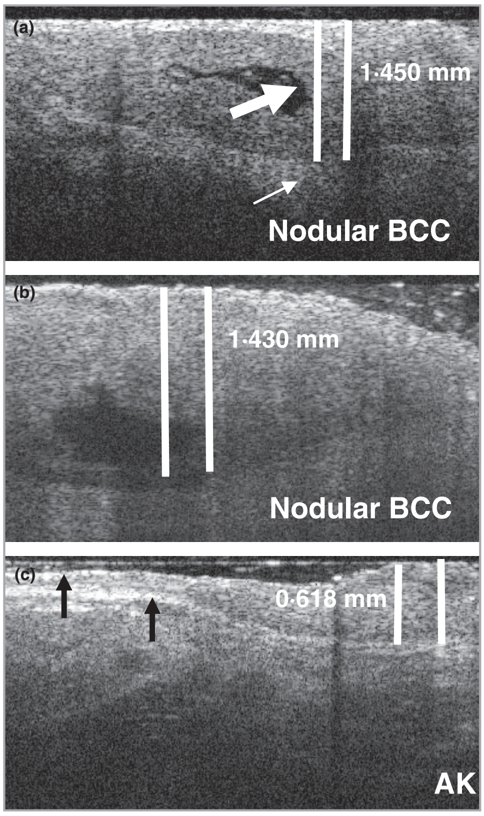

Fig 2. Characteristic optical coherence tomography (OCT) images of two nodular basal cell carcinomas (BCCs, a, b) and an actinic keratosis (AK, c). Thickness measurements using both OCT and 20-MHz high-frequency ultrasound underestimated thickness in both nodular BCCs. White bars indicate thickness measurements. (a) A black necrotic centre is indicated by a fat arrow. The thin arrow indicates the white stroma surrounding the BCC. (b) A similar OCT image from a nodular BCC is seen also with a necrotic centre. In both lesions the depth seems well defined in the OCT image but on histology the BCC thickness was measured to be 5·500 mm (a) and 2·330 mm (b). (c) OCT image of an AK. The white streaks in the epidermis are easily seen (black arrows). The histological depth was 0·330 mm.

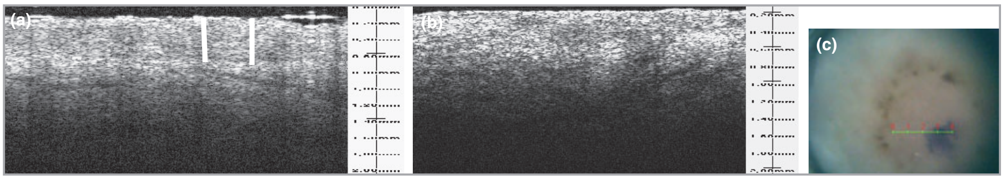

Fig 3. Optical coherence tomography (OCT) images before and after local analgesia. OCT image of BCC lesion prior to local analgesia (a); maximal tumour depth is marked by a white line. (b) OCT image of the same lesion after injection of 10% lidocaine with adrenaline; note the blurred delineation of the BCC. (c) Image from the probe; the green line indicates where the biopsy was performed.

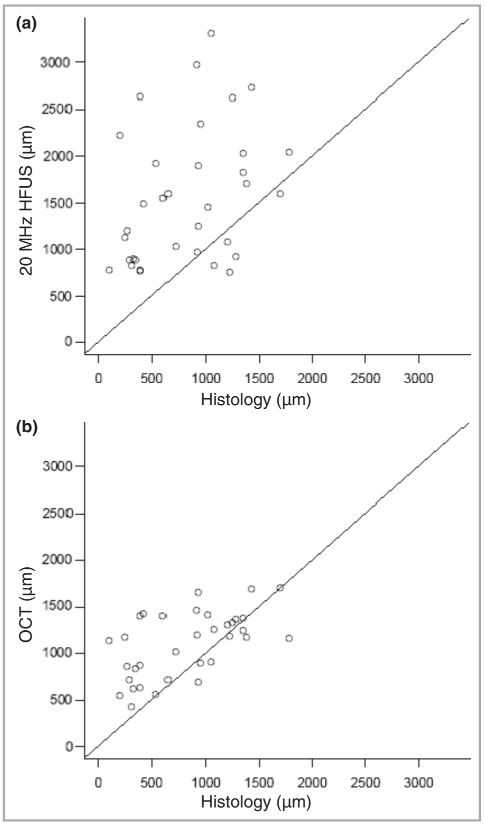

Fig 4. Thickness measured by 20-MHz high-frequency ultrasound (HFUS) (a) and optical coherence tomography (OCT) (b) plotted against histological tumour thickness. Both imaging methods overestimate thickness compared with histopathology, but OCT measurements differ less than ultrasound.

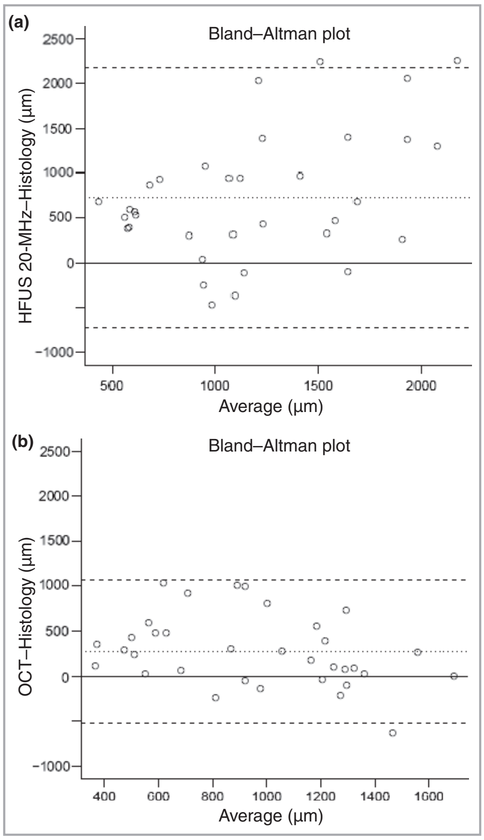

Fig 5. Two Bland–Altman plots showing differences between thickness measured by 20-MHz high-frequency ultrasound (HFUS) (a) and optical coherence tomography (OCT) (b) and thickness measured with light microscopy plotted against the mean thickness measurement of OCT and HFUS, respectively. The solid line represents zero bias (no difference between the imaging technique and histopathology). The dashed lines show the 95% limits of agreement and the dotted line represents bias.

The two observers agreed on thickness (± 0·2 mm) in 12 of 34 (35%) cases using OCT. Interobserver variation reflected by the intratumour correlation coefficient was estimated to be 0·34, which indicates less than moderate agreement between observers. Mean ± SD thickness was 1·096 ± 0·352 mm and 1·271 ± 0·615 mm, respectively. A paired t-test showed no significant difference between measurements (P = 0·09). However, the less skilled observer tended to overestimate

Table 2 Relationship between penetration depth in optical coherence tomography (OCT) images and selected predictors (age, sex, skin colour and skin type) by multiple regression analysis

	Patient data (n = 76)	P-value
OCT penetration depth (µm), mean ± SD	1112·1 ± 187·9	
Predictors		
Age (years), mean ± SD	70·2 ± 11·2	0·916
L* cheek, mean ± SD	59·7 ± 4·3	0·398
A* cheek, mean ± SD	14·4 ± 3·5	0·274
L* arm, mean ± SD	68·2 ± 3·2	0·348
A* arm, mean ± SD	7·4 ± 2·5	0·575
Sex	54% female	0·605
Fitzpatrick skin type	3/76 type I	0·952
	35/76 type II	
	34/76 type III	
	4/76 type IV	

thickness in OCT images, and his measurements were discarded when comparing OCT with histology.

Penetration depth of optical coherence tomography

In BCC this was generally higher compared with normal skin and AK, but in nodular BCC lesions where the main tumour burden was located at the upper 1 mm of the lesion the penetration was more shallow. Multiple linear regression was performed in order to identify predictors of OCT penetration depth in the normal facial skin. No obvious relation between OCT penetration depth and the individual predictors was found when performing univariate regression, and all the postulated predictors taken together explained less than 5% of the variation in the data. The OCT penetration depth in all 76 patients and its relation to skin colour and type are shown in Table 2.

Discussion

In accordance with other studies, we identified morphological features in OCT images that correspond to histopathology: disruption of layering[24,26,28,40] (demonstrated in both AK and BCC), focal changes including thickening of epidermis (AK),[24,27] and dark rounded areas, sometimes surrounded by a white core, representing BCC islands and surrounding stroma.[25,28,41] All NMSC lesions appeared hyporeflective in HFUS. This is in accordance with other studies.[33,35,36,41,42] Importantly, it has been shown that all skin tumours appear hyporeflective, suggesting that HFUS alone is not always suitable for differential diagnosis.[43] This is in good agreement with our finding that AK and BCC appear similar in HFUS, as both lesions appear hypoechogenic in HFUS.

We found that OCT is more precise than 20-MHz HFUS for mean maximal thickness measurement in AK and BCC lesions thinner than 2 mm. This is in accordance with another study using OCT to measure tumour thickness in BCC lesions < 1·2 mm in depth, where OCT measurements correlated well with histology.[20]

Both OCT and especially HFUS, however, tend to overestimate tumour depth compared with histology. This is illustrated in the Bland–Altman plots in Figure 5. By determining the prediction interval, rather than simple correlations, we estimated the agreement reported as a numerical value. This is important in tumour depth measurement, because we were interested not only in estimating agreement between methods, but also in quantifying how well the methods agreed. Simple correlations may be high even though the absolute differences between methods may be large.

The smaller bias of OCT is attributed mainly to better resolution, but may also be caused by the ability of BCC and AK to provide better contrast from backscattered infrared radiation than the contrast provided by the acoustic characteristics of the tissue. An important factor that may explain some of the difference between *in vivo* (OCT and HFUS) and *ex vivo* (microscopy) tumour depth estimation is the well-known shrinkage of the skin that occurs during the process of staining. Another potential bias is that the OCT software uses the average refractive index (RI) of 1·4 for distance calculation in OCT images and does not adjust for potentially different RI in normal skin and NMSC. A similar bias occurs in HFUS.

Gambichler *et al.*[42] compared 20- and 100-MHz ultrasound in a study of superficial malignant melanoma thickness and also found a systematic overestimation of thickness. They demonstrated larger limits of agreement for 20-MHz ultrasound imaging compared with 100-MHz. Only a few studies have compared OCT and HFUS imaging of skin tumours and normal skin. One study was concerned with tumours related to the eye and included 38 periocular lesions, including four BCC and one AK. OCT was able to show small cystic structures more distinctly and HFUS appeared superior in assessing the margins of the tumours.[44] The other study that compared OCT and HFUS of normal skin found that the dermoepidermal junction was more well defined in OCT compared with 100-MHz HFUS.[45]

Several factors may influence the accuracy of OCT measurements. Infiltrative analgesia appears to blur OCT images, and it is therefore suggested that these are recorded prior to any injection. A certain level of operator dependency also appears to be present. We found a less than moderate interobserver agreement for measuring thickness with OCT, and the subjectivity in thickness estimation using OCT should therefore not be neglected.

Our study, however, suggests that skin colour does not affect penetration depth of OCT in normal skin, and the hypothesis that age, sex and skin colour predict OCT penetration depth was not supported. The varying penetration depth and image quality may therefore be due to local anatomical variation, e.g. hair follicles and sebaceous glands that tend to make OCT images more heterogeneous and layering less distinct.[46]

Monitoring of treatment is an interesting potential for imaging methods such as OCT and HFUS. BCC thickness measured with HFUS before PDT has been shown to predict the probability of local recurrence 1 year after treatment.[15] The ability to monitor regression of a BCC after 5-fluorouracil treatment using HFUS has also been demonstrated.[35] Conclusively, for thickness measurement in superficial tumours this systematic comparison between mean OCT and HFUS tumour thickness demonstrates that OCT is more accurate and less biased than HFUS.

Acknowledgments

M.M. and J.B.T. were funded by a grant from The National Technical-Scientific Board in Denmark (BIOLASE 26-02-0020, now BIOPHOT).

References

1 Diepgen TL. [Epidemiology of chronic UV-damage]. *J Dtsch Dermatol Ges* 2005; **3** (Suppl. 2):S32–5.

2 Rowe DE, Carroll RJ, Day CL Jr. Prognostic factors for local recurrence, metastasis, and survival rates in squamous cell carcinoma of the skin, ear, and lip. Implications for treatment modality selection. *J Am Acad Dermatol* 1992; **26**:976–90.

3 Cherpelis BS, Marcusen C, Lang PG. Prognostic factors for metastasis in squamous cell carcinoma of the skin. *Dermatol Surg* 2002; **28**:268–73.

4 Garbe C, Eigentler TK. Diagnosis and treatment of cutaneous melanoma: state of the art 2006. *Melanoma Res* 2007; **17**:117–27.

5 Tejera-Vaquerizo A, Mendiola-Fernandez M, Fernandez-Orland A *et al.* Thick melanoma: the problem continues. *J Eur Acad Dermatol Venereol* 2008; **22**:575–9.

6 Krawtchenko N, Roewert-Huber J, Ulrich M *et al.* A randomised study of topical 5% imiquimod vs. topical 5-fluorouracil vs. cryosurgery in immunocompetent patients with actinic keratoses: a comparison of clinical and histological outcomes including 1-year follow-up. *Br J Dermatol* 2007; **157** (Suppl. 2):34–40.

7 Tillman DK Jr, Carroll MT. A 36-month clinical experience of the effectiveness of curettage and imiquimod 5% cream in the treatment of basal cell carcinoma. *J Drugs Dermatol* 2008; **7**:S7–14.

8 Wagstaff AJ, Perry CM. Topical imiquimod: a review of its use in the management of anogenital warts, actinic keratoses, basal cell carcinoma and other skin lesions. *Drugs* 2007; **67**:2187–210.

9 Ulrich C, Busch JO, Meyer T *et al.* Successful treatment of multiple actinic keratoses in organ transplant patients with topical 5% imiquimod: a report of six cases. *Br J Dermatol* 2006; **155**:451–4.

10 Ulrich C, Hackethal M, Ulrich M *et al.* Treatment of multiple actinic keratoses with topical diclofenac 3% gel in organ transplant recipients: a series of six cases. *Br J Dermatol* 2007; **156** (Suppl. 3):40–2.

11 Surrenti T, De Angelis L, Di Cesare A *et al.* Efficacy of photodynamic therapy with methyl aminolevulinate in the treatment of superficial and nodular basal cell carcinoma: an open-label trial. *Eur J Dermatol* 2007; **17**:412–15.

12 Lehmann P. Methyl aminolaevulinate–photodynamic therapy: a review of clinical trials in the treatment of actinic keratoses and nonmelanoma skin cancer. *Br J Dermatol* 2007; **156**:793–801.

13 Braathen LR, Szeimies RM, Basset-Seguin N *et al.* Guidelines on the use of photodynamic therapy for nonmelanoma skin cancer: an international consensus. International Society for Photodynamic Therapy in Dermatology, 2005. *J Am Acad Dermatol* 2007; **56**:125–43.

14 Calzavara-Pinton PG, Venturini M, Sala R *et al.* Methylaminolaevulinate-based photodynamic therapy of Bowen's disease and squamous cell carcinoma. *Br J Dermatol* 2008; **159**:137–44.

15 Moore JV, Allan E. Pulsed ultrasound measurements of depth and regression of basal cell carcinomas after photodynamic therapy: relationship to probability of 1-year local control. *Br J Dermatol* 2003; **149**:1035–40.

16 McLoone N, Donnelly RF, Walsh M *et al.* Aminolaevulinic acid diffusion characteristics in '*in vitro*' normal human skin and actinic keratosis: implications for topical photodynamic therapy. *Photodermatol Photoimmunol Photomed* 2008; **24**:183–90.

17 Su SY, Giorlando F, Ek EW *et al.* Incomplete excision of basal cell carcinoma: a prospective trial. *Plast Reconstr Surg* 2007; **120**:1240–8.

18 Tan PY, Ek E, Su S *et al.* Incomplete excision of squamous cell carcinoma of the skin: a prospective observational study. *Plast Reconstr Surg* 2007; **120**:910–16.

19 Ulrich M, Maltusch A, Rowert-Huber J *et al.* Actinic keratoses: non-invasive diagnosis for field cancerisation. *Br J Dermatol* 2007; **156** (Suppl. 3):13–17.

20 Olmedo JM, Warschaw KE, Schmitt JM *et al.* Correlation of thickness of basal cell carcinoma by optical coherence tomography *in vivo* and routine histologic findings: a pilot study. *Dermatol Surg* 2007; **33**:421–5.

21 Gonzalez S, Swindells K, Rajadhyaksha M *et al.* Changing paradigms in dermatology: confocal microscopy in clinical and surgical dermatology. *Clin Dermatol* 2003; **21**:359–69.

22 Mogensen M, Jemec GB. Diagnosis of nonmelanoma skin cancer/keratinocyte carcinoma: a review of diagnostic accuracy of nonmelanoma skin cancer diagnostic tests and technologies. *Dermatol Surg* 2007; **33**:1158–74.

23 Abuzahra F, Marquardt Y, Spoeler F *et al.* Sub-cellular high resolution optical coherence tomography: a novel non-invasive diagnostic tool in dermatology. *J Invest Dermatol* 2004; **122**:A41.

24 Barton JK, Gossage KW, Xu W *et al.* Investigating sun-damaged skin and actinic keratosis with optical coherence tomography: a pilot study. *Technol Cancer Res Treat* 2003; **2**:525–35.

25 Bechara FG, Gambichler T, Stucker M *et al.* Histomorphologic correlation with routine histology and optical coherence tomography. *Skin Res Technol* 2004; **10**:169–73.

26 Gambichler T, Orlikov A, Vasa R *et al.* *In vivo* optical coherence tomography of basal cell carcinoma. *J Dermatol Sci* 2007; **45**:167–73.

27 Korde VR, Bonnema GT, Xu W *et al.* Using optical coherence tomography to evaluate skin sun damage and precancer. *Lasers Surg Med* 2007; **39**:687–95.

28 Olmedo JM, Warschaw KE, Schmitt JM *et al.* Optical coherence tomography for the characterization of basal cell carcinoma *in vivo*: a pilot study. *J Am Acad Dermatol* 2006; **55**:408–12.

29 Steiner R, Kunzi RK, Scharffetter KK. Optical coherence tomography: clinical applications in dermatology. *Med Laser Appl* 2003; **18**:249–59.

30 Strasswimmer J, Pierce MC, Park BH *et al.* Polarization-sensitive optical coherence tomography of invasive basal cell carcinoma. *J Biomed Opt* 2004; **9**:292–8.

31 Welzel J, Lankenau E, Birngruber R, Engelhardt R. Optical coherence tomography of the human skin. *J Am Acad Dermatol* 1997; **37**:958–63.

32 Jemec GB, Gniadecka M, Ulrich J. Ultrasound in dermatology. Part I. High frequency ultrasound. *Eur J Dermatol* 2000; **10**:492–7.

33 Desai TD, Desai AD, Horowitz DC *et al.* The use of high-frequency ultrasound in the evaluation of superficial and nodular basal cell carcinomas. *Dermatol Surg* 2007; **33**:1220–7.
34 Wortsman XC, Holm EA, Wulf HC *et al.* Real-time spatial compound ultrasound imaging of skin. *Skin Res Technol* 2004; **10**:23–31.
35 Gupta AK, Turnbull DH, Foster FS *et al.* High frequency 40-MHz ultrasound. A possible noninvasive method for the assessment of the boundary of basal cell carcinomas. *Dermatol Surg* 1996; **22**:131–6.
36 Harland CC, Bamber JC, Gusterson BA *et al.* High frequency, high resolution B-scan ultrasound in the assessment of skin tumours. *Br J Dermatol* 1993; **128**:525–32.
37 Fujimoto JG. Optical coherence tomography for ultrahigh resolution *in vivo* imaging. *Nat Biotechnol* 2003; **21**:1361–7.
38 Andersen P, Thrane L, Tycho A, Jemec GBE. Optical coherence tomography in dermatology. In: *Handbook of Non-invasive Methods and the Skin* (Serup J, Jemec GBE, Grove GL, eds), 2nd edn. Boca Raton: CRC Press, 2006; 257–66.
39 Anderson RR, Parrish JA. The optics of human skin. *J Invest Dermatol* 1981; **77**:13–19.
40 Welzel J. Optical coherence tomography in dermatology: a review. *Skin Res Technol* 2001; **7**:1–9.
41 Lassau N, Spatz A, Avril MF *et al.* Value of high-frequency US for preoperative assessment of skin tumors. *Radiographics* 1997; **17**:1559–65.
42 Gambichler T, Moussa G, Bahrenberg K *et al.* Preoperative ultrasonic assessment of thin melanocytic skin lesions using a 100-MHz ultrasound transducer: a comparative study. *Dermatol Surg* 2007; **33**:818–24.
43 Ruocco E, Argenziano G, Pellacani G *et al.* Noninvasive imaging of skin tumors. *Dermatol Surg* 2004; **30**:301–10.
44 Buchwald HJ, Müller A, Kampmeier J, Lang GK. [Optical coherence tomography versus ultrasound biomicroscopy of conjunctival and eyelid lesions]. *Klin Monatsbl Augenheilkd* 2003; **220**:822–9.
45 Vogt M, Knuettel A, Hoffmann K *et al.* Comparison of high frequency ultrasound and optical coherence tomography as modalities for high resolution and non invasive skin imaging. *Biomed Tech (Berl)* 2003; **48**:116–21.
46 Mogensen M, Morsy HA, Thrane L *et al.* Morphology and epidermal thickness of normal skin imaged by optical coherence tomography. *Dermatology* 2008; **217**:14–20.

Paper IV

Assessment of Optical Coherence Tomography Imaging in the Diagnosis of Non-Melanoma Skin Cancer and Benign Lesions Versus Normal Skin: Observer-Blinded Evaluation by Dermatologists and Pathologists

Assessment of Optical Coherence Tomography Imaging in the Diagnosis of Non-Melanoma Skin Cancer and Benign Lesions Versus Normal Skin: Observer-Blinded Evaluation by Dermatologists and Pathologists

METTE MOGENSEN, MD,* THOMAS MARTINI JOERGENSEN, MSCEE, PHD,†
BIRGIT MEINCKE NÜRNBERG, MD,‡ HANAN AHMAD MORSY, MD,* JAKOB B. THOMSEN, MSCI,†
LARS THRANE, MSCI, PHD,† AND GREGOR B. E. JEMEC, MD, DMSC*

BACKGROUND Optical coherence tomography (OCT) is an optical imaging technique that may be useful in diagnosis of non-melanoma skin cancer (NMSC).

OBJECTIVES To describe OCT features in NMSC such as actinic keratosis (AK) and basal cell carcinoma (BCC) and in benign lesions and to assess the diagnostic accuracy of OCT in differentiating NMSC from benign lesions and normal skin.

METHODS AND MATERIALS OCT and polarization-sensitive (PS) OCT from 104 patients were studied. Observer-blinded evaluation of OCT images from 64 BCCs, 1 baso-squamous carcinoma, 39 AKs, two malignant melanomas, nine benign lesions, and 105 OCT images from perilesional skin was performed; 50 OCT images of NMSC and 50 PS-OCT images of normal skin were evaluated twice.

RESULTS Sensitivity was 79% to 94% and specificity 85% to 96% in differentiating normal skin from lesions. Important features were absence of well-defined layering in OCT and PS-OCT images and dark lobules in BCC. Discrimination of AK from BCC had an error rate of 50% to 52%.

CONCLUSION OCT features in NMSC are identified, but AK and BCC cannot be differentiated. OCT diagnosis is less accurate than clinical diagnosis, but high accuracy in distinguishing lesions from normal skin, crucial for delineating tumor borders, was obtained.

The authors have indicated no significant interest with commercial supporters.

Non-melanoma skin cancer (NMSC) is the most common malignancy in the Western world.[1] The majority of tumors are of low-grade malignancy, but misdiagnosis, suboptimal therapy, or underestimation of the biological potential of the primary tumor can cause serious morbidity. Early diagnosis is a critical factor in overall prognosis. Diagnostic accuracy in clinical diagnosis of NMSC ranges from 56% to 90% in sensitivity and 75% to 90% in specificity.[2,3] The diagnostic reference standard is histopathology, and biopsies are routinely taken to confirm or determine the diagnosis. A diagnostic technology to assist diagnosis could therefore potentially increase accuracy and lower morbidity associated with NMSC.

Optical coherence tomography (OCT) is an optical imaging technology that offers real-time imaging with micrometer resolution.[4,5] Skin is imaged by measuring the backscatter and reflection of infrared light directed toward the skin. It has been suggested that it might be useful in diagnosis of NMSC[6–10] and for in vivo delineation of tumor borders in NMSC.[7,11]

Unfortunately, technological zeal may lead many diagnostic techniques to be introduced into a clinical

*Department of Dermatology, Roskilde Hospital, Faculty of Health Sciences, University of Copenhagen, Roskilde, Denmark; †DTU Fotonik, Department of Photonics Engineering, Technical University of Denmark, Denmark; ‡Department of Pathology, Roskilde Hospital, Faculty of Health Sciences, University of Copenhagen, Roskilde, Denmark

• Published by Wiley Periodicals, Inc. •
ISSN: 1076-0512 • Dermatol Surg 2009;35:1–8 • DOI: 10.1111/j.1524-4725.2009.01164.x

setting without the necessary prior estimation of their diagnostic accuracy. Studies of new diagnostic tests and technologies should be performed following the internationally recognized set of guidelines called Standards for Reporting of Diagnostic Accuracy published in 2003.[12] Only a few formal diagnostic studies have been conducted in the field of OCT imaging of NMSC;[9,13,14] and more are required to establish the accuracy and clinical usefulness of OCT in NMSC diagnosis.

In previous studies, OCT images of basal cell carcinomas (BCCs) and actinic keratosis (AK) generally demonstrated loss of normal layered skin architecture and features like dark lobules (BCC) and thickening of and dark bands in epidermis (AK). These features correlate well with histopathology.[6,9,10] OCT studies on squamous cell carcinomas have been performed mainly on mucosal surfaces.[15,16] No studies have assessed the ability of combined OCT features to differentiate NMSC from normal skin in a clinical setting. The ability of OCT to differentiate NMSC lesions from normal skin is crucial for its potential use in delineation of skin tumors. The aims of this study are to describe morphological OCT features in NMSC and in benign lesions initially misdiagnosed as NMSC and to assess the diagnostic accuracy of OCT in differentiating NMSC from normal skin and AK from BCC.

Materials and Methods

Patients

One hundred four patients with 176 lesions were recruited consecutively from March 2006 to July 2007. Mean age was 69.3 (range 37–90); 57% were female. The study conformed to the Helsinki II declaration and was approved by the local Ethics Committee (Ref no. 2005-1-41). The OCT scanning was performed on the intended target population for OCT diagnosis: NMSC patients in a university hospital setting.[17] Each lesion was identified clinically and marked with a black pen before OCT scanning and a 2- to 3-mm punch biopsy was taken in the OCT-scanned spot. Normal adjacent skin was also OCT imaged. For histopathology, AK diagnostic criteria were epidermal dysplasia involving the intra-adnexal epidermis to varying degrees and elastoid degeneration of dermis, which may contain a lymphohistiocytic infiltrate.

OCT System

OCT is a noninvasive optical imaging technology that can provide cross-sectional tomographic images of tissue in situ and in real-time with high axial resolution.[4,8,18] The OCT system used was developed at the Technical University of Denmark. The light source was a superluminescent diode with a center wavelength of 1,318 nm and a bandwidth of 66 nm. Axial resolution of the system was 8 μm and lateral resolution 24 μm. OCT works analogously to ultrasound; the reflection of infrared light (instead of acoustical waves) from the skin is measured, and the signal strength is imaged as a function of position. The image data are displayed by assigning color or gray scales to each reflection according to the measured signal strength. The OCT probe is applied directly after application of ultrasound gel to the skin. Some tissues, such as muscle and collagen, are birefringent. In polarization-sensitive OCT (PS-OCT) the birefringence of tissue can be measured.[19] In our OCT system, PS-OCT images are recorded in parallel with standard OCT images. Acquisition time for an OCT image is 3 seconds. The OCT probe has a built-in camera. A video image of the particular skin surface scanned accompanies each OCT scan.

The data set was selected from good quality images. Good quality OCT images were defined as images that were scanned on the exact predetermined area with no or minimum motion or other artifacts.

OCT Images

A minimum of two OCT and two PS-OCT images were recorded from each lesion. A total of 425 OCT images and 425 PS-OCT images were recorded from 176 lesions in 104 patients. The quality of the images was assessed according to defined quality criteria. Only 250 of 425 (59%) of OCT images fulfilled the criteria. Discarded images mainly had large entrance artifacts (too little gel) or shadow artifacts (hyperkeratotic lesions) and motion artifacts, often due to mismatch of the probe and skin. In more than 50 images, good quality OCT scans were discarded because they did not represent the exact spot where the biopsy was taken as determined from the OCT probe video image. The 250 optimal quality OCT images represented scans from 101 lesions in 63 patients. Because PS-OCT images are recorded in parallel with OCT images, all 250 good quality OCT images had a correspondingly good PS-OCT image. OCT scanning was also performed in normal adjacent skin approximately 3 cm from the lesion. A total of 390 good quality OCT and PS-OCT images were recorded from normal skin. No biopsies were taken from normal skin.

NMSC Morphology and Features in OCT Images

A break-up of the characteristic layering in normal skin[20] is found in OCT images of NMSC and malignant melanoma (MM)[21] lesions, but this break-up is also seen in various benign lesions such as seborrheic keratosis[8] and benign melanocytic nevi.[21] We chose to have observers examine five key OCT image features selected from earlier studies and according to our own experience: disruption of layering[6,8,10,13] (demonstrated in AK and BCC); white streaks and dots in epidermis (hyperkeratosis in AK); other focal changes including thickening of the epidermis (AK);[9,13] dark rounded areas, sometimes surrounded by a white area (BCC basaloid island cell clusters and surrounding stroma);[6,10,22] and presence of a nonbirefringent, homogeneous band[23] in the upper part of PS-OCT images, which is approximately 200 μm in normal images corresponding to epidermis and papillar dermis. The change in collagen architecture identifies the border between papillary dermis and reticular dermis in PS-OCT images from normal skin. Absence or break-up of this band has been described in invasive BCC.[24]

Observer Variation

The data set was randomly selected from the 250 good quality OCT and 250 good quality PS-OCT images of lesions and 390 OCT and PS-OCT images from normal skin.

Training Set

The independent observers (four dermatologists and two surgical pathologists) received a standardized 30-minute instructional presentation of 50 OCT images that pointed out the characteristic OCT and PS-OCT features in NMSC and normal skin.

Study Set

Because of observer time limitation, only 115 OCT and matched PS-OCT images from lesions and 105 OCT and PS-OCT images from normal skin were studied. The 115 OCT images clinically diagnosed as NMSC on referral consisted of 64 BCCs, one basosquamous carcinoma, 39 AKs, two malignant melanomas, one neurofibroma, one hemangioma, two seborrheic keratosis, one perifolliculitis, one planopapullar papilloma, and three severe solar elastosis. All OCT images were presented to observers projected onto a board to standardize image presentation. See Figure 1 for an image set from the observer-blinded study. Each observer filled out a standardized questionnaire during each session. One author (MM), who did not participate in the observer-blinded evaluation, made all presentations. Only two doctors had prior experience with OCT images. All observers were blinded with respect to patient identity and clinical and histopathological diagnosis of the lesion in OCT images. Two observers examined the same images twice with a 4-week interval to determine intra-observer differences.

Statistics

Sample size calculation for each OCT image session was performed using the equation described by Simel and colleagues[25] from an expected sensitivity of 79% and specificity 75%: sample size was 52 images. Sensitivity and specificity data and paired *t*-tests were calculated in Excel, Microsoft Office 2003. $P < .05$ was considered statistically significant. Interobserver and intra-observer reproducibility

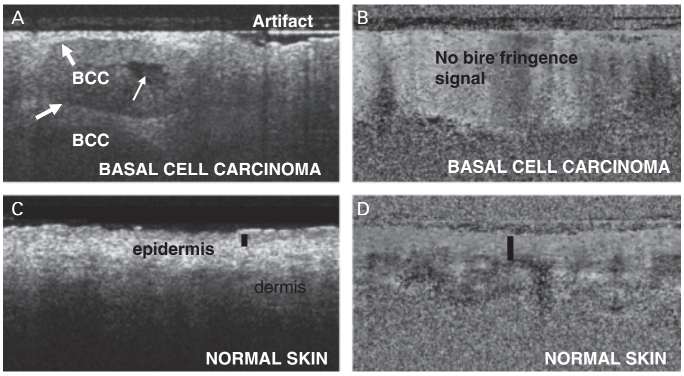

Figure 1. An original set of optical coherence tomography (OCT) images from the observer-blinded evaluation of differentiating actinic keratosis (AK) from basal cell carcinoma (BCC). (A) BCC lesion, thin white arrow points to the necrotic center, fat arrows to basaloid tumor cell island borderline. (B) Corresponding polarization-sensitive (PS)-OCT image. Compared with normal PS-OCT image (D), there is no homogeneous, upper horizontal band. (C) Normal adjacent skin. (D) PS-OCT image from normal skin. The upper, homogeneous band corresponds to epidermis and papillary dermis (black bar).

were calculated from the questionnaires completed during the observer-blinded OCT image sessions. Kappa statistics were calculated in MATLAB and interpreted as 0.00 = poor, 0.01 to 0.20 = slight, 0.21 to 0.40 = fair, 0.41 to 0.60 = moderate, 0.61 to 0.80 = good, and 0.81 to 1.00 = excellent.

Results

OCT Morphology

Clinically, NMSC can be differentiated from normal skin with a high degree of accuracy. In our diagnostic OCT imaging study, a number of confounding anatomical features were revealed that influenced the interpretation of the image. Some anatomical structures may affect the image in the same way (e.g., hair follicles can mimic basophilic island cell clusters or vice versa). For an outline of OCT features in NMSC, benign lesions, and normal skin, see Table 1. A break-up of the characteristic layering in normal skin was found in OCT images of NMSC but also in benign lesions previously clinically misdiagnosed as NMSC. We found that the basophilic island cell clusters in BCC can often be visualized in OCT images as dark (gray to black) rounded areas. A white border previously demonstrated to represent the tumor stroma sometimes surrounded these dark areas (Figure 2).[6,10] In most OCT images of AK, white dots and streaks were demonstrated in the upper epidermis. The histological equivalents were dense, hyperkeratotic areas. Focal disruptions in epidermis were common; small and elongated white and dark areas were identified. Thick AK lesions tended to look more like BCC lesions with gray to dark rounded areas in epidermis but slightly more homogeneous than BCC.

Absence of a broad upper homogeneous band in PS-OCT images of NMSC was demonstrated in most NMSC lesions but also in the benign lesions. No distinct layering was identified between papillary dermis and reticular dermis in PS-OCT images of lesions. This border was identified in most PS-OCT images of adjacent normal skin.

Successive OCT images of the same area of the skin presented a stable, recognizable image pattern, indicating high reproducibility.

Observer-Blinded Evaluation

Differentiating skin diagnosed as NMSC from OCT images of normal skin was performed with a sensitivity of 58% to 94% and a specificity of 43% to 96%. Only two of the six observers evaluated all

TABLE 1. Optical Coherence Tomography (OCT) Morphology of Non-Melanoma Skin Cancer (NMSC), Benign Lesions, and Normal Skin

OCT Feature	*Distinct Layering*	*Focal Changes in Epidermis*	*Lobular Changes*	*Distinct Layering in Polarization-Sensitive OCT*
Normal skin	Present	Hairs create shadow artifacts; bright entrance signal is common	Hair follicles and sebaceous units look dark	Present
Benign lesions	Absent	White streaks seen in seborrheic keratosis and perifolliculitis	Seborrheic keratosis showed bright round areas	Absent
AK	Varies	White streaks and dots in most lesions	Some lesions with gray areas	Some lesions with intact epidermis in regular OCT have disruption of the upper layer
BCC	Absent in superficial BCC; Some nodular BCC have intact upper layering	White streaks and dots in some lesions	Gray to black areas sometimes surrounded by a white border	Absent

BCC, basal cell carcinoma.

OCT images. These observers, the two most experienced in OCT image interpretation, differentiated normal from lesional skin more accurately than OCT novices: sensitivity 79% to 94% and specificity 85% to 96%, with moderate interobserver agreement (kappa = 0.52). Sensitivity increased significantly for all participants between the first and second evaluations of OCT images ($p = .01$).

Discrimination of AK from BCC had an error rate of 52% (AK) and 50% (BCC) (kappa = 0.62). Specificity was 76% and sensitivity was 42% when differentiating AK from BCC for two observers. BCC was more difficult to diagnose, and the two observers classified BCC as AK in 75% and 83% of misdiagnosed cases.

The strongest diagnostic features of OCT in terms of agreement between the two observers were absence of well-defined layering (kappa = 0.80, overall agreement 0.90) and absence of distinct layering in PS-OCT images of lesions (kappa = 0.72, overall

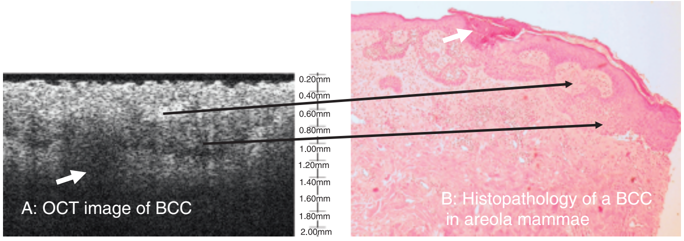

Figure 2. Basal cell carcinoma in areola mammae. (A) optical coherence tomography (OCT) image of the lesion. (B) Corresponding histopathology (hematoxylin and eosin stain, magnification × 40) from the same area as (A). Black arrows point to similar morphologies in the images. White arrow indicates a shadow in the OCT image and corresponding hyperkeratosis in (B).

agreement 0.86). There was also excellent to good agreement on focal changes, black areas, and white streaks and dots.

Generally, OCT features in NMSC were more easily differentiated from normal skin than when AK was compared with BCC, with kappa values and overall agreement decreasing from the differentiation of normal skin from NMSC to the differentiation of AK from BCC.

The only PS-OCT feature evaluated was presence of a homogeneous band in the upper part of the PS-OCT image. Changes in most PS-OCT images of NMSC lesions were identified as thinning, thickening, or disappearance of the upper homogeneous band. The two observers identified absence of a broad upper homogeneous band in 100% and 79% of lesions, respectively, but PS-OCT did not improve overall diagnostic accuracy; one observer changed in sensitivity from 94% to 93%, whereas specificity increased from 86% to 100%; the other observer decreased in sensitivity from 79% to 70% and in specificity from 96% to 75%.

The two observers evaluated OCT images of NMSC and normal skin and had good (kappa = 0.78) to slight (kappa = 0.31) intra-observer agreement, with an overall agreement of 0.88 and 0.66, respectively.

Discussion

We demonstrated a characteristic OCT morphology of AK, BCC, and normal adjacent skin in accordance with other studies,[6,10,11,14,20,26–28] and we discovered the OCT morphology matches well-known histopathology of NMSC. When OCT images from the same lesions were compared, they looked similar, in concordance with the high reproducibility of OCT images demonstrated in earlier studies of epidermis and nail thickness measurements.[20,29,30]

Korde and colleagues[9] studied OCT images of sun-damaged skin and AK and described the accuracy of dark elongated bands in the epidermis for diagnosis of AK. These bands correspond to keratin deposits in a thickened stratum corneum. Dark bands enabled detection of AK with a sensitivity of 86% and a specificity of 83% in their study. We did not evaluate dark bands specifically, but we identified them in some of our OCT images, suggesting that they may not be a general feature. Some OCT images from normal skin in our study displayed characteristics of solar damage, not surprisingly, given the age and risk group studied. The problem in differentiating AK from sun-damaged skin in OCT images[9] may explain the difficulty we also met in separating some lesions from normal skin. The decreased penetration depth of OCT in AK that we identified is attributed to the optical properties of hyperkeratosis in AK.

A break-up of the characteristic layering of normal skin is found in OCT and PS-OCT images of NMSC and benign lesions; this finding complicates differentiation of malignant from benign lesions and indicates that break-up of layering does not have the diagnostic effect that would be expected if the study included only NMSC. Therefore, we specifically included benign lesions in the study set. Differentiation of skin lesions using OCT is not as straightforward as would be expected given the high accuracy of differentiating normal skin from NMSC lesions clinically. Our data suggest that the OCT features described in this study and earlier studies[6–10] are not sufficiently accurate to differentiate NMSC from normal skin, which is crucial if OCT is to be used in delineation of NMSC borders and tumor depth measurement. However, it is encouraging that OCT can differentiate normal skin from lesions in general. Although experienced observers obtained high accuracy, images did not appear to be easy to interpret by inexperienced observers. A weakness of this study was that not all six observers examined all images, so we focused on accuracy data from the two of six observers who examined all OCT images. Intra-observer agreement was only slight to good between these two observers, suggesting that some features described are too subtle and difficult to recognize. Based on our results from the interobserver study, we suggest that OCT comes with a learning curve that may be steeper than in confocal laser microscopy[31,32] but is still encouraging. Another weakness was that, because of poor image quality, we were able to use only 250 of 425 OCT images recorded. This is primarily because of the design of the custom-built probe and would be significantly ameliorated by a simple redesign of the probe housing. It was mostly the first images recorded that had many artifacts, due to limited use of ultrasound gel and motion artifacts. More than 50 of 425 images were excluded because they were not scanned exactly where the biopsy was performed. A potential consequence of excluding some OCT images is an overestimation of the diagnostic accuracy. The sensitivity and specificity data reported here are therefore of a preliminary character, but once image quality and resolution are improved, future diagnostic accuracy studies on OCT and skin cancer may elucidate the diagnostic potential of OCT imaging.

The diagnostic performance of OCT that we have estimated in NMSC is comparable with that assessed in endoscopic OCT diagnosis of dysplasia in Barrett's esophagus: sensitivity 68% and specificity 82%.[33] These authors suggest, as we do, that refining the OCT morphological diagnostic criteria and improving image quality and resolution of OCT images could increase diagnostic accuracy.

We cannot conclude that the information within PS-OCT images presented in our study enhances diagnostic accuracy of OCT imaging, although this was suggested in an earlier study that examined two single invasive BCC lesions with PS-OCT.[24] Our study indicates that normal skin[30] is easily recognized in PS-OCT images. The changes that we identify in PS-OCT images from NMSC lesions are attributed to the changes in collagen content and rearrangement of collagen fibers.[11,23]

Conclusively, the naked eye is currently superior to OCT for diagnosis of NMSC, but we suggest that refinement of diagnostic criteria through evaluation of larger case series, including various types of NMSC lesions and benign lesions in combination with improvement in OCT image quality and resolution, can in the future establish the diagnostic potential of OCT in NMSC.

Acknowledgments We thank Dr. Michael Heidenheim, Dr. Lars Erik Bryld, Dr. Preben Løvgreen, Dr. Thomas Norman Dam, and Dr. Tove Agner for valuable feedback and participation in OCT image evaluation in Department of Dermatology, Roskilde Hospital, Denmark. Dr. Mogensen's salary was funded by a grant from The National Technical-Scientific Board in Denmark (BIOLASE 26-02-0020, now BIOPHOT).

References

1. Neville JA, Welch E, Leffell DJ. Management of nonmelanoma skin cancer in 2007. Nat Clin Pract Oncol 2007;4:462–9.
2. Mogensen M, Jemec GB. Diagnosis of nonmelanoma skin cancer/keratinocyte carcinoma: a review of diagnostic accuracy of nonmelanoma skin cancer diagnostic tests and technologies. Dermatol Surg 2007;33:1158–74.
3. Jemec GB. The diagnostic accuracy of Danish GPs in the diagnosis of pigmented skin lesions. Fam Pract 1999;16:619–20.
4. Fujimoto JG. Optical coherence tomography for ultrahigh resolution in vivo imaging. Nat Biotechnol 2003;21:1361–7.
5. Huang D, Swanson EA, Lin CP, et al. Optical coherence tomography. Science 1991;254:1178–81.
6. Olmedo JM, Warschaw KE, Schmitt JM, et al. Optical coherence tomography for the characterization of basal cell carcinoma in vivo: a pilot study. J Am Acad Dermatol 2006;55:408–12.
7. Olmedo JM, Warschaw KE, Schmitt JM, et al. Correlation of thickness of basal cell carcinoma by optical coherence tomography in vivo and routine histologic findings: a pilot study. Dermatol Surg 2007;33:421–5.
8. Welzel J. Optical coherence tomography in dermatology: a review. Skin Res Technol 2001;7:1–9.
9. Korde VR, Bonnema GT, Xu W, et al. Using optical coherence tomography to evaluate skin sun damage and precancer. Lasers Surg Med 2007;39:687–95.
10. Gambichler T, Orlikov A, Vasa R, et al. In vivo optical coherence tomography of basal cell carcinoma. J Dermatol Sci 2007;45:167–73.
11. Pierce MC, Strasswimmer J, Park BH, et al. Advances in optical coherence tomography imaging for dermatology. J Invest Dermatol 2004;123:458–63.
12. Bossuyt PM, Reitsma JB, Bruns DE, et al. Toward complete and accurate reporting of studies of diagnostic accuracy. The STARD initiative. Am J Clin Pathol 2003;119:18–22.

13. Barton JK, Gossage KW, Xu W, et al. Investigating sun-damaged skin and actinic keratosis with optical coherence tomography: a pilot study. Technol Cancer Res Treat 2003;2:525–35.
14. Petrova GA, Derpalyek E, Gladkova N, et al. Optical coherence tomography using tissue clearing for skin disease diagnosis. Optical Coherence Tomography and Coherence Techniques. Proc of SPIE 5140. 2003. p. 168–186.
15. Wilder-Smith P, Krasieva T, Jung WG, et al. Noninvasive imaging of oral premalignancy and malignancy. J Biomed Opt 2005;10:051601.
16. Armstrong WB, Ridgway JM, Vokes DE, et al. Optical coherence tomography of laryngeal cancer. Laryngoscope 2006;116: 1107–13.
17. Knottnerus JA. The Evidence Base of Clinical Diagnosis. Spain: BMJ Books; 2002.
18. Gladkova ND, Petrova GA, Nikulin NK, et al. In vivo optical coherence tomography imaging of human skin: norm and pathology. Skin Res Technol 2000;6:6–16.
19. Hee MR, Huang D, Swanson EA, et al. Polarization-sensitive low-coherence reflectometer for birefringence characterization and ranging. J Opt Soc Am 1992;B9:903–8.
20. Gambichler T, Matip R, Moussa G, et al. In vivo data of epidermal thickness evaluated by optical coherence tomography: effects of age, gender, skin type, and anatomic site. J Dermatol Sci 2006;44:145–52.
21. Gambichler T, Regeniter P, Bechara FG, et al. Characterization of benign and malignant melanocytic skin lesions using optical coherence tomography in vivo. J Am Acad Dermatol 2007.
22. Bechara FG, Gambichler T, Stucker M, et al. Histomorphologic correlation with routine histology and optical coherence tomography. Skin Res Technol 2004;10:169–73.
23. Strasswimmer J, Pierce MC, Park B, et al. Characterization of basal cell carcinoma by multifunctional optical coherence tomography. J Invest Dermatol 2003;121:0156.
24. Strasswimmer J, Pierce MC, Park BH, et al. Polarization-sensitive optical coherence tomography of invasive basal cell carcinoma. J Biomed Opt 2004;9:292–8.
25. Simel DL, Samsa GP, Matchar DB. Likelihood ratios with confidence: sample size estimation for diagnostic test studies. J Clin Epidemiol 1991;44:763–70.
26. Steiner R, Kunzi RK, Scharffetter KK. Optical coherence tomography: clinical applications in dermatology. Med Laser Appl 2003;18:249–59.
27. Welzel J, Lankenau E, Birngruber R, et al. Optical coherence tomography of the human skin. J Am Acad Dermatol 1997;37: 958–63.
28. Welzel J, Lankenau E, Birngruber R, et al. Optical coherence tomography of the skin. Curr Probl Dermatol 1998;26:27–37.
29. Mogensen M, Thomsen JB, Skovgaard LT, et al. Nail thickness measurements using optical coherence tomography and 20-MHz ultrasonography. Br J Dermatol 2007;157:894–900.
30. Mogensen M, Morsy HA, Thrane L, et al. Morphology and epidermal thickness of normal skin imaged by optical coherence tomography. Dermatology 2008;217:14–20.
31. Gerger A, Koller S, Weger W, et al. Sensitivity and specificity of confocal laser-scanning microscopy for in vivo diagnosis of malignant skin tumors. Cancer 2006;107:193–200.
32. Nori S, Rius-Diaz F, Cuevas J, et al. Sensitivity and specificity of reflectance-mode confocal microscopy for in vivo diagnosis of basal cell carcinoma: a multicenter study. J Am Acad Dermatol 2004;51:923–30.
33. Isenberg G, Sivak MV Jr., Chak A, et al. Accuracy of endoscopic optical coherence tomography in the detection of dysplasia in Barrett's esophagus: a prospective, double-blinded study. Gastrointest Endosc 2005;62:825–31.

Address correspondence and reprint requests to:
Mette Mogensen, MD, Department of Dermatology,
Roskilde Hospital, Koegevej 7-13, DK-4000 Roskilde,
Denmark, or e-mail: mmg@regionsjaelland.dk

Paper V

Field programmable gate-array-based real-time optical Doppler tomography system for in vivo imaging of cardiac dynamics in the chick embryo

Optical Engineering 48(2), 023201 (February 2009)

Field programmable gate-array-based real-time optical Doppler tomography system for *in vivo* imaging of cardiac dynamics in the chick embryo

Lars Thrane[*,§]
Henning E. Larsen[*]
Technical University of Denmark
Department of Photonics Engineering
DTU Fotonik
P.O. Box 49
DK-4000 Roskilde, Denmark
E-mail: lars.thrane@risoe.dk

Kambiz Norozi[†]
Hannover Medical School
Department of Pediatric Cardiology and Intensive Care Medicine
Carl Neuberg Strasse 1
D-30625 Hannover, Germany

Finn Pedersen
Jakob B. Thomsen
Technical University of Denmark
Department of Photonics Engineering
DTU Fotonik
P.O. Box 49
DK-4000 Roskilde, Denmark

Maja Trojer
Lund Institute of Technology
Department of Physics
P.O. Box 118
SE-221 00 Lund, Sweden

Talât Mesud Yelbuz[‡]
Hannover Medical School
Department of Pediatric Cardiology and Intensive Care Medicine
Carl Neuberg Strasse 1
D-30625 Hannover, Germany

Abstract. We demonstrate a field programmable gate-array-based real-time optical Doppler tomography system. A complex-valued bandpass filter is used for the first time in optical coherence tomography signal processing to create the analytic signal. This method simplifies the filter design, and allows efficient and compact implementation by combining the conversion to an analytic signal with a pulse shaping function without the need for extra resources as compared to the Hilbert transform method. The conversion of the analytic signal to amplitude and phase is done by use of the coordinate rotation digital computer (CORDIC) algorithm, which is an efficient algorithm that maps well to the field programmable gate array. Flow phantom experiments, and the use of this system for *in vivo* imaging of cardiac dynamics in the chick embryo, are presented. We demonstrate the visualization of blood flow in the early embryonic heart as well as in the aorta, small peripheric vitelline vessels, and coronary arteries of fully formed chick hearts. [DOI: 10.1117/1.3081062]

Subject terms: optical coherence tomography; optical Doppler tomography; digital signal processing; field programmable gate array; complex-valued bandpass filter.

Paper 080513R received Jun. 27, 2008; revised manuscript received Dec. 19, 2008; accepted for publication Jan. 5, 2009;

1 Introduction

The heart is the first organ to *form* and *function* in vertebrates and undergoes simultaneous *structural* and *functional* maturation as it transforms in a dynamic process from a straight tube to a four-chambered heart.[1,2] Altered development, which possibly occurs at various stages of cardiogenesis, can result in various groups of congenital heart malformations in a stage and region-dependent manner.[3,4] Congenital malformations of the heart are among the most common birth defects, and are the leading cause of birth-defect-related deaths.[5,6] However, the cause of most congenital heart defects still remains unknown.

Several studies that have been conducted with microcinephotography and Doppler ultrasound have suggested that hemodynamic changes in blood flow and pressure are critical factors for the embryonic heart at earliest stages, and that these hemodynamic changes can precede heart defects.[7–9] Unfortunately, a precise understanding of how flow disruptions lead to cardiovascular defects has been hampered by the inadequacy of existing analytical tools for noninvasive *in vivo* imaging of the embryonic heart with sufficient depth penetration and resolution.

Optical coherence tomography (OCT), a noncontact, noninvasive, and nondestructive high-resolution imaging modality based on broadband near-infrared light for sample illumination, was introduced to developmental biology in

---

[*] These two authors contributed equally to this work.

[†] Present address: Department of Pediatrics/Pediatric Cardiology, University of Western Ontario, 800 Commissioners Rd E, London, ON, Canada, N6A 5W9.

[‡] Present address: Division of Pediatric Cardiology, McMaster Children's Hospital, McMaster University, 1200 Main St W, HSC-3A, Hamilton, ON L8S 3Z5, Canada.

[§] Author to whom all correspondence should be addressed.

1997 by Boppart et al.,[10] and is well suited for anatomical and functional imaging of the developing cardiovascular system, as it has been demonstrated by various groups in recent years for different species.[11–24] OCT allows *ex vivo* and *in vivo* imaging of the embryonic heart in two and three dimensions at resolutions of 2 to 30 μm and up to a depth of 1 to 2 mm,[25–27] and is thus superior to other imaging tools that are used such as confocal microscopy and ultrasound.

Several functional extensions of OCT have been developed, including Doppler OCT.[28,29] Doppler OCT extracts the flow-induced Doppler shift imparted on back-reflected sample light by the motion of small particles, e.g., erythrocytes in a capillary. Because this Doppler shift is proportional to flow velocity, Doppler OCT can image blood flow. To realize real-time Doppler OCT imaging whether in time- or frequency-domain OCT, fast advanced signal processing is needed. Digital signal processing in general, i.e., using either a software-based approach or external dedicated hardware, has previously been shown to provide this capability.[30–34]

We present a real-time optical Doppler tomography system, where the signal processing is entirely based on a field programmable gate array (FPGA). The advantage of an FPGA implementation relative to a pure PC software implementation is a more compact system, because the interface to the computer can be a standard serial bus such as USB, which means a portable computer can be used. An FPGA implementation also has important advantages over a general purpose digital signal processor (DSP) due to the fact that the processing elements operate in parallel, as opposed to the DSP, which is primarily a sequential processor, as discussed in detail in Ref. 35. In Ref. 35, the first implementation of Doppler OCT signal processing entirely based on a single FPGA was demonstrated for a slow speed system. Here, flow phantom experiments and *in vivo* imaging of cardiac dynamics in the chick embryo are presented using a much faster FPGA-based real-time time-domain optical Doppler tomography system. We demonstrate the visualization of blood flow in the early embryonic heart as well as in the aorta, small peripheric vitelline vessels, and coronary arteries of fully formed chick hearts.

A complex bandpass filter is used to create the analytic signal. To the best of our knowledge, this has not been demonstrated before in OCT signal processing. This method simplifies the filter design, and allows an efficient and compact implementation by combining the conversion to an analytic signal with a pulse shaping function without the need for extra resources, as compared to the Hilbert transform method.

The processing scheme is mapped to the FPGA resources by use of the coordinate rotation digital computer (CORDIC) algorithm, which is an iterative algorithm for calculating trigonometric functions. It is well suited to hardware implementations, such as FPGAs, because it does not require large storage or any multiplication operations, i.e., only the operations addition, subtraction, and shifting are needed. In addition, this implementation has the important feature that calculation of the phase in addition to the amplitude only requires few additional resources.

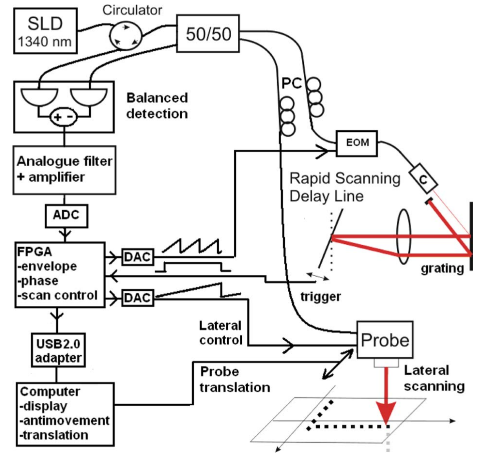

Fig. 1 Overall block diagram of the Doppler OCT system. PC: polarization control. SLD: superluminescent diode. ADC: analog-to-digital converter. DAC: digital-to-analog converter. C: collimator. EOM: electro-optic modulator. FPGA: field programmable gate array. 50/50: fiber optic 50/50 beamsplitter.

2 Field Programmable Gate-Array-Based Real-Time Optical Doppler Tomography System

The system configuration is shown in Fig. 1. The light source is a superluminescent diode with 1340-nm center wavelength, a power of 25 mW (ex fiber), and a full-width half maximum (FWHM) bandwidth of 61 nm (InPhenix IP-SDD1305, InPhenix, Livermore, California) corresponding to an axial resolution of ~9 μm in tissue. Light from the source is coupled into a fiber-based Michelson interferometer consisting of a 50/50 beamsplitter. In the reference arm, we use a rapid scanning optical delay line[36] employing a resonance scanner with a resonance frequency of 4 kHz equal to the A-scan rate. In the Doppler mode, an electro-optic modulator (EOM) sets the center frequency of the interferogram to 3.2 MHz.[37] Light directed to the sample is focused to a spot size of ~34 μm determining the lateral resolution. A lateral scan is provided by a galvanometer pivoting a mirror. An optical circulator is used in conjunction with balanced detectors (New Focus, San Jose, California, model 1817) to reject the high dc background and increase the signal-to-noise (SNR) ratio. The system sensitivity was measured to be 99 dB. Extraction of the phase shift of the interferogram is made by the sequential scan processing algorithm[38] using typically eight sequential A-scans at each lateral position on the sample. The phase shift due to block motion is attenuated by an antimotion correction algorithm (see Sec. 2.1.7). The envelope and phase information is calculated in an FPGA (Altera Corporation, San Jose, California, EP1S80) and transferred to the computer through an USB2.0 channel. The sequential scan processing algorithm ensures high velocity sensitivity, and the antimotion correction algorithm makes it possible to visualize blood flow inside the beating, i.e., moving chick

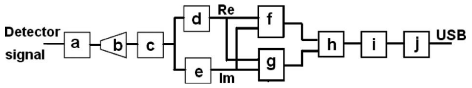

Fig. 2 OCT signal processing in FPGA. Data flow from left to right, where thin lines show analog signal, and thick lines show digital signals: (a) amplifier and bandpass filter, (b) analog-to-digital converter, (c) decimating by 8 low-pass filter, (d) complex bandpass filter cosinus part, (e) complex bandpass filter sinus part, (f) Kasai autocorrelation, (g) envelope estimation using CORDIC, (h) concatenation of Doppler and envelope data into one dataset, (i) buffer, frame marker, and microprocessor bus interface, and (j) Cypress CY7C68013 USB microcontroller. Elements (c) through (i) are all implemented in a single FPGA.

heart. The flow information is laid over the structural OCT image, generating so-called color Doppler OCT images.

2.1 *Signal Processing Unit*

In Fig. 2 is a block diagram of the signal processing chain from the detector to the USB interface. The detector signal is amplified and bandpass filtered (Krohn-Hite Corporation, model 3945, Fig. 2 block a) before being applied to the ADC (Fig. 2 block b). The purpose of the bandpass filter is two fold: antialiasing, and removal of low frequency interference. The antialiasing is required due to the subsequent sampling at discrete times, and according to the Nyquist criteria, it must have a cut-off frequency of less than half the sample rate. In this case, the sample rate is 120 MS/s. The analog signal from the detector has a high content of low frequency interference. If not removed before digitization, it will significantly restrict the obtainable dynamic range in the frequency band of interest. The ADC has a resolution of 12 bits.

Fourier-domain rapid scanning optical delay lines have been used in a number of high-speed OCT systems with the resultant OCT signal bandwidth $f_{\mathrm{OCT}}(t)$ varying sinusoidally as[39]

$$\Delta f_{\mathrm{OCT}}(t) = \frac{2\pi D \Delta\lambda f_a}{\lambda^2}\cos(2\pi f_a t), \tag{1}$$

where $D=2.7$ mm is the axial scan depth, $f_a=4$ kHz is the axial scan frequency, $\Delta\lambda=61$ nm is the light source 3-dB bandwidth, and λ is the light source center wavelength resulting in maximum signal bandwidths of 2.4 MHz.

The signal of interest from the detector has a bandwidth of 2.4 MHz centered on 3.2 MHz. No frequency translation is made before low-pass filtering, which means that we have to take account of the highest frequency component of the signal when evaluating the Nyquist sample rate, which here is $2\times(3.2+0.5\times 2.4)$ MS/s=9 MS/s. Sampling is, however, done at 120 MS/s. By oversampling 13 times, the requirement to the transition sharpness of the antialiasing is relaxed significantly because the Nyquist rate is now 60 MHz, but our signal bandwidth is still 5 MHz. The sharp filtering is thus relegated to the digital domain, where the implementation of a sharp and accurate digital filter is much simpler than an equivalent analog one.

2.1.1 *Decimating low-pass filter*

After digital low-pass filtering, the sample frequency f_s is lowered to 15 MHz by rejection of 7 out of 8 samples. This conserves processing power in the FPGA. Discarding samples can be done under the condition that the spectral content of the signals above the new Nyquist rate of 7.5 MHz is reduced below the noise floor of the original signal, because discarding 7 out of 8 samples folds the signal spectrum above 7.5 MHz down into the 0- to 7.5-MHz region.

Initially, the quantization noise from the ADC is spread out evenly over the entire bandwidth from 0 to $\frac{1}{2}f_s$ =60 MHz. However, as a consequence of the digital low-pass filtering, only the quantization noise within the filter passband will appear in the end result. Therefore, since the filter removes the out-of-band noise, there is an improvement in the signal-to-quantization-noise ratio relative to the case without low-pass filtering. Lower quantization noise is equivalent to an increased number of bits in the ADC converter. The equivalent effective number of bits is improved by $\frac{1}{2}\log 2[f_s/(2f_{lp})]$ bits, where f_s is the sample rate before decimation, and f_{lp} is the bandwidth of the signal after low-pass filtering.[40] In our case, this amounts to an improvement in the effective signal-to-quantization-noise ratio corresponding to $\frac{1}{2}\log 2[120/(2\times 5.0)]=1.8$ bits, or 10.8 dB. This is improving the dynamic range in the acquisition by 10.8 dB, but not the sensitivity, as this is given by the detector shot noise.

The decimating low-pass filter is implemented as a finite impulse response (FIR) filter. It has 19 taps, linear phase, and is realized in a fully parallel structure. Because it is decimating by 8, only every eighth input clock edge needs to give an output sample. This is exploited to make the architecture more efficient by use of the polyphase structure.[41]

2.1.2 *Conversion to an analytic signal*

Narrowband signals can be processed in a flexible manner when converted to an analytic signal. It is common practice to use a Hilbert transform to convert a real signal to a complex signal with only energy at positive frequencies. A Hilbert transform is noncausal, so in a flow-through architecture like the one implemented in the FPGA, it has to be transformed into a causal filter. This is done by delaying the impulse response of the filter and multiplying it with a window function that is zero for negative (noncausal) samples and for samples greater than some finite positive integer N. The output of this filter is the imaginary part of the analytic signal. But because of the introduced delay and applied window, a nonuniform frequency dependent response is introduced in the imaginary path. The real part of the signal needs to be delayed by the same amount. Ideally, it must also have the same amplitude response. This means that ideally, a shaping filter has to be employed in the real path as well; a simple delay is not sufficient in general, as this will not match the amplitude response of the truncated Hilbert response. The method described in the next section solves this problem, simplifies the filter design, and allows an efficient implementation by combining the conversion to

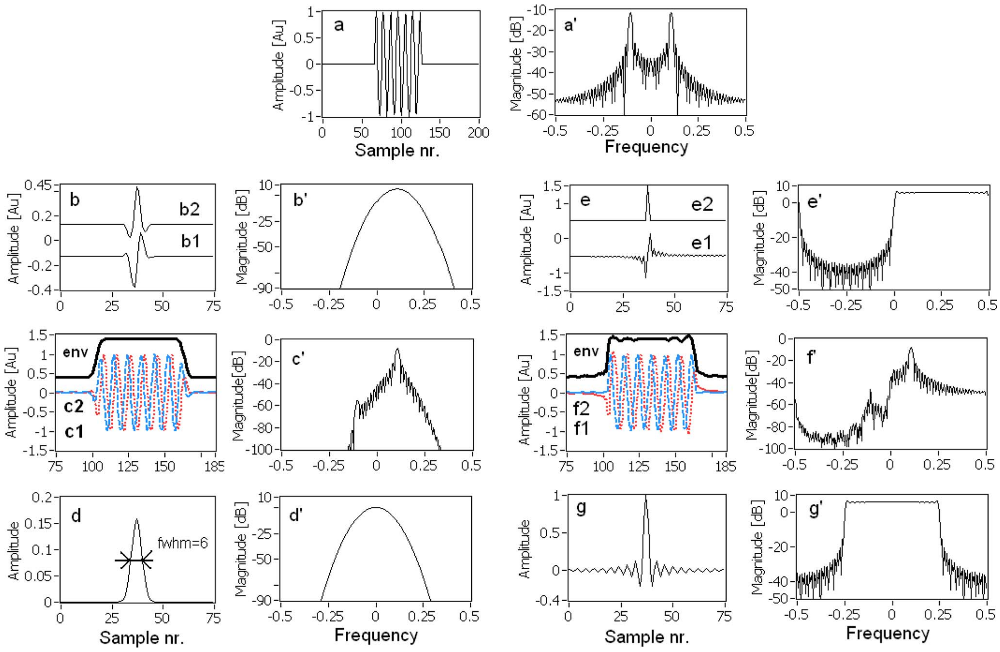

Fig. 3 Comparison of processing of an OCT signal [(a), top] using a complex filter (two left columns), and a Hilbert transform filter with delay matching (two right columns). Plots with quoted labels are the spectra of the nonquoted plots. (a) Simplified model of an OCT signal having a square envelope. (b1) Imaginary, and (b2) real part of the complex filter $h[n]\exp(j\omega_0)$. Dashed curve c2 (blue; leading) is (a) filtered through filter part b2, and dotted curve c1 (red; lagging) is (a) filtered through filter part b1. Envelope (env) is based on modulus of signals c1 and c2. A vertical offset is inserted to improve visibility. (d) Response of the prototype filter $h[n]$. (e1) Hilbert filter impulse response. (e2) Hilbert delay matching filter impulse response. Dashed curve f2 (blue; leading) is (a) filtered through e2, and dotted curve f1 (red; lagging) is (a) filtered through e1. (g) Hilbert filter frequency shifted by −0.25 to show equivalence with prototype filter in (d). (Color online only.)

an analytic signal with a pulse shaping function without requiring extra resources compared to the Hilbert transform method.

Complex bandpass filter used to create an analytic signal. The interferogram is filtered using a filter with a complex impulse response $h_{cpx}[n]$, which is discrete in time and implements a frequency-shifted version of a low-pass prototype filter $h[n]$.[42] The shifting is done by multiplying the impulse response of the prototype filter with a complex exponential, such that the impulse response can be written as

$$h_{cpx}[n] = h[n]\exp(j\omega_0 n)$$
$$= h[n]\left[\cos(\omega_0 n) + \exp\left(j\frac{\pi}{2}\right)\sin(\omega_0 n)\right], \qquad (2)$$

where n is the sample number, and $\exp(j\omega_0 n)$ is the complex exponential of radial frequency ω_0. As seen by the right part of Eq. (2), this filter has an exact phase difference of $\frac{1}{2}\pi$ between the real and the imaginary part, and is called a phase-splitting filter in Ref. 43.

The signals in the frequency and time domain are illustrated in Fig. 3, showing the filtering in both a Hilbert implementation and an implementation based on a complex frequency shifted filter. On top of Fig. 3 is a signal in the form of an OCT burst having a square envelope. The response of the two types of filters to this signal is shown in Figs. 3(b)–3(g). The left columns [Figs. 3(b)–3(d)] use the suggested complex filter, and in the two right columns [Figs. 3(e)–3(g)] use the Hilbert filter with delay matching. Figure 3(d) shows the impulse response of the prototype filter $h[n]$ with its equivalent spectrum in Fig. 3(d′). Its complex shifted version is illustrated in Figs. 3(b) and 3(b′), and the results from filtering Fig. 3(a) with b1 and b2 are shown in Fig. 3(c) (c1, c2 and c′). Similarly, Fig. 3(g) shows the impulse response of the combined Hilbert and its associated delay matching filter had it been shifted to be symmetric around 0 rad/s, and having a real-valued impulse response. The Hilbert implementation illustrated in Figs. 3(e) and 3(f) uses the filters that have their responses illustrated in e1 and e2 in Fig. 3. The results from filtering Fig. 3(a) with e1 and e2 are illustrated in f1 and f2 in Fig. 3, respectively.

The Hilbert implementation has significantly more ripples in the time response [Fig. 3(f) (env)] compared to the suggested complex filter implementation [Fig. 3(c) (env)]. Because the complex frequency shifted filter also removes the high frequency components that are outside the signal band, the signal-to-noise ratio is improved. It is possible to implement a Hilbert filter with less ripple using windowing or equiripple design methods, but it will result in further amplitude mismatch in the two paths outside of the passband because the delay path has a flat amplitude response. Using the method of a frequency-shifted low-pass filter has the advantage that the frequency or time response can be tailored to the system requirements.

The spectral components at the negative frequencies of the input signal are attenuated by using the suggested complex filter implementation. The resulting signal is analytic with only positive frequency components, which means that the envelope can be obtained by taking the vector magnitude. However, using the Hilbert transform method, one is obliged to incorporate an additional filter stage if pulse shaping and noise filtering are required. The advantage of using a filter as described in Eq. (2) is that it combines pulse shaping and noise filtering into the same filter, as is used to generate the analytic signal, thus conserving processing power.

The signal from the detector can be modeled as a modulated real-valued sinusoidal-wave signal with carrier frequency ω_c, and can be written as

$$\begin{aligned} x[n] &= a[n]\cos(\omega_C n + \phi[n]) \\ &= \mathrm{Re}[a[n]\exp(j\phi[n])\exp(j\omega_C n)] \\ &= \mathrm{Re}[g[n]\exp(j\omega_C n)], \end{aligned} \tag{3}$$

where $a[n]$ is the envelope, $\phi[n]$ is phase modulation, and $g[n]=a[n]\exp(j\phi[n])$. $G[\exp(j\omega)]$ and $H[\exp(j\omega)]$ are the Fourier transforms of $g[n]$ and $h[n]$, respectively. If $\omega_c \approx \omega_0$ and $h[n]$ is a low-pass filter with a bandwidth such that the spectra $G\{\exp[j(\omega+\omega_c)]\}$ and $H(\exp[j(\omega-\omega_0)])$ are nonoverlapping, it can be shown (see Appendix) that the result of filtering the time sequence in Eq. (3) through the filter described in Eq. (2) is approximately

$$\tilde{y}[n] = \frac{1}{2}\exp(j\omega_C n)\{g[n]*(h[n]\exp[j(\omega_0 - \omega_C)n])\}. \tag{4}$$

This shows that the filtered $\tilde{y}[n]$ output looks as if the modulation part $a[n]\exp(j\phi[n])$ of the interferogram is filtered through the frequency-shifted low-pass prototype filter $h[n]\exp[j(\omega_0-\omega_c)n]$ and subsequently multiplied with a complex sinusoid $\exp(j\omega_c n)$ with the original frequency of the carrier of $x[n]$.

To reliably reproduce the envelope and phase modulation, the filter $h[n][\exp j(\omega_0-\omega_c)n]$ should have sufficient bandwidth to pass the spectrum of $g[n]$, i.e., $H\{\exp[j(\omega-\omega_0)]\}$ should overlap $G\{\exp[j(\omega-\omega_c)]\}$. By making $h[n]$ a filter with linear phase, there will be no dispersion in the filter, and the phase of the output reproduces the phase of the interferogram apart from an offset.

2.1.3 *Envelope and phase calculation using the coordinate rotation digital computer algorithm*

To get the envelope $a[n]$ of the interferogram, the magnitude of the analytic signal is obtained, i.e.,

$$a[n] \approx |\tilde{y}[n]| = [\mathrm{Re}(\tilde{y}[n])^2 + \mathrm{Im}(\tilde{y}[n])^2]^{1/2}.$$

The proportionality gain in $h[n]$ can be ignored here, as it is constant in the passband. The phase is

$$\phi[n] = \varphi_0 + \angle\tilde{y}[n] = \arctan[\mathrm{Im}(\tilde{y}[n])/\mathrm{Re}(\tilde{y}[n])],$$

where φ_0 accounts for the constant phase shift in the filter, and in this application it can be ignored.

One way to implement these calculations is by use of a look-up table.[31] This approach has the drawback of requiring a table size that grows exponentially in size with increasing precision, because each additional bit doubles the storage requirement. In the present implementation, the coordinate rotation digital computer (CORDIC) algorithm is used.[44] The CORDIC algorithm calculates trigonometric functions using an iterative algorithm, and is here used in a mode where it converts vectors from Cartesian to polar coordinates covering the range $\pm\pi$. The iteration is made up of a series of successively smaller and smaller rotations of the original vector by a set of predetermined rotation angles, which are selected so that the required multiplications are powers of two, and with signs making the final vector argument approaching zero. This means that the multiplications can be replaced by shift operations. Shift operations require much less processing resources than general multiplications do. The only RAM storage required is for the intermediate results. Both multipliers and storage are expensive resources in an FPGA. Therefore, the CORDIC algorithm maps well to an FPGA implementation. An added benefit of the CORDIC algorithm is that the result consists of both the magnitude and the argument of the input vector, and this with only a marginally extra cost of processing. Another method to calculate amplitude and phase described in Ref. 45 and called the BKM algorithm is in many ways similar to the CORDIC algorithm in its shift-and-add iterative structure. However, the BKM algorithm requires more hardware and is well suited for redundant number systems. The presented system uses two-complement binary numbers and thus cannot benefit from the latter feature. The BKM algorithm has a built-in scaling factor of unity, whereas in the CORDIC algorithm it is a nonunity constant. In this application the scaling factor is of no concern, as it is simply a constant gain factor.

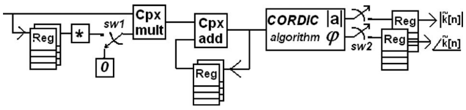

Fig. 4 Implementation details of block f in Fig. 2. Hardware for evaluation of the Kasai algorithm. "Reg" are storage of *M* locations. Two of them are complex-valued. Cpx-mult and Cpx-add are complex multiplier and adder, respectively. The block with $*$ is a complex conjugator. Switch sw1 is set at 0 for the first scan to ensure that this only contributes once to the sum in Eq. (6). Switch sw2 at the output ensures that only the final averaged result for a series of scans is sent downstream. Complex-valued $\tilde{k}[n]$, expressed in polar form, is the sum of products used to estimate the average phase shift.

2.1.4 *Sequential A-scan processing*

A series of M axial depth scans each consisting of N samples is performed at each transverse location. The analytic OCT signal is acquired. We describe it as $\tilde{y}_m[n]$ with an additional subindex m relative to Eq. (4). This is the scan number at a given lateral position, and n is the pixel number in the axial direction.

The mean flow velocity $\langle v[n]\rangle$ at a given pixel n can be calculated from the mean Doppler frequency shift $\langle f_D[n]\rangle$ as[46]

$$\langle v[n]\rangle = \frac{\lambda_0\langle f_D[n]\rangle}{2n_t\cos(\theta)}, \tag{5}$$

where n_t is the index of refraction of tissue or blood, θ is the Doppler angle, and λ_0 is the center optical wavelength.

A well-known method to evaluate $\langle f_D[n]\rangle$ is the Kasai autocorrelation algorithm, which compares and averages the phase change between sequential A-scans[47]

$$\langle f_D[n]\rangle = \frac{f_a}{2\pi}\angle\sum_{m=0}^{M-2}\tilde{y}_{m+1}[n]\tilde{y}_m^*[n], \tag{6}$$

where $\tilde{y}_m^*[n]$ is the complex conjugate of $\tilde{y}_m[n]$. Each term in the sum of products $\tilde{k}[n]=\Sigma_{m=0}^{M-2}\tilde{y}_{m+1}[n]\tilde{y}_m^*[n]$ is a complex vector with a modulus equal to $|\tilde{y}_{m+1}[n]||\tilde{y}_m[n]|$, i.e., the product of the modulus of two sequential vectors. The argument of such a term is $\angle\tilde{y}_{m+1}[n]-\angle\tilde{y}_m[n]$, which is the angle difference between scans. Summing these M vectors will give a resulting vector where individual scans give a contribution weighted by its amplitude. Each scan contributes to two terms in Eq. (6), except the first and the last, which only appear once. Therefore, a scan with low amplitude will contribute less than an equivalent high amplitude scan, thus giving a weighted average favoring large amplitude measurements. In our setup with $\theta\cong 80$ deg, and assuming $n_t=1.4$, the aliasing velocity equal to $\pm\langle v[n]\rangle$ is ± 5.6 mm/s.

The algorithm of Eq. (6) is implemented in the FPGA (block *f* in the diagram in Fig. 2). Figure 4 shows this implementation in further detail, one sample at a time, flowing from left to right. Each sample is associated with a sample number n and scan sequence number m as it flows through the processor.

Logic ensures that the switch (sw1) at the input to the complex multiplier is in position "0" at the first scan on a lateral position $(m=0)$, ensuring that the nonexisting scan $\tilde{y}_{-1}^*[n]$ is set to 0. The registers on Fig. 4 are implemented as dual-port RAMs, which allow writing and reading simultaneously. This is needed to implement a flow-through architecture without wait states, thus giving a processor that is fast and can process a sample on every clock cycle. This is necessary here because there is no data buffer upstream of this block. Data flow control is done by inserting idle scans, but only between sequential scans at a given transverse location, and not within a series of scans at one transverse location, as this would disrupt the estimate of the Doppler shift measurement.

Downstream from CORDIC algorithm in Fig. 4 a switch (sw2) is located, which only connects at the last scan, and the phase change estimate is then saved in a register. From there, it is transferred to the PC. The block with the CORDIC algorithm in Fig. 4 produces not only the phase of $\tilde{k}[n]$ but also the magnitude almost without further resources due to the nature of the CORDIC algorithm. The magnitude $|\tilde{k}[n]|$ can be used to calculate the variance of the flow velocity according to the formula[47]

$$\sigma^2 = f_a^2\left(1-\frac{\dfrac{1}{M-1}|\tilde{k}[n]|}{\dfrac{1}{M}\displaystyle\sum_{m=0}^{M-1}\tilde{y}_m[n]\tilde{y}_m^*[n]}\right), \tag{7}$$

where the denominator is the squared and averaged envelope.[46] However, in this implementation, the variance is not used.

2.1.5 *Envelope calculation*

As mentioned in a previous section, the envelope of the OCT signal is calculated using the CORDIC algorithm. The averaging over M consecutive scans is done according to Eq. (8),

$$\langle a[n]\rangle = \frac{1}{M}\sum_{m=0}^{M-1}|\tilde{y}_m[n]|, \tag{8}$$

where $\langle a[n]\rangle$ is the average value of the envelope at sample n. In practice, the hardware is implementing Eq. (8) recursively as in Eq. (9), where m is stepping from 0 to M-1,

$$a_{m+1}[n] = a_m[n] + |\tilde{y}_m[n]|$$

$$a_0[n] = 0 \quad \text{and } m = [0,\ldots,M-1]$$

$$\langle a[n]\rangle = \frac{1}{M}a_{M-1}. \tag{9}$$

This function is implemented in block g in Fig. 2 and detailed further in Fig. 5. Notice a similar sequential processing as in the Kasai estimator, where each acquired sample flows through the structure. Not shown are the control and sample numbers assigned to the samples, which ensures the

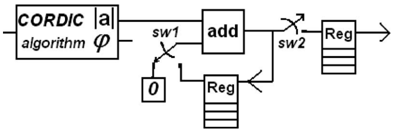

Fig. 5 Flow-through processor structure for calculating the envelope and averaging over *M* scans. This figure details further block g in Fig. 2. “Reg” blocks are storage for *N* locations. Logic ensures via switch sw1 that the first scan is not accumulated with old data. Switch sw2 at the output ensures that only the final averaged result for a series of scans is sent downstream.

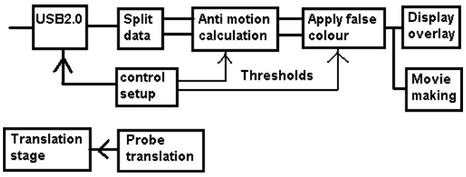

Fig. 6 Program in the PC implementing motion compensation, display of overlayed images, and generation of movie.

proper sequencing, storage, and retrieval from the on-chip RAM of the FPGA. The normalization by the factor $1/M$ due to the number of M sequential scans is done in the presentation software of the PC.

Data from the Kasai and envelope estimators are grouped together for each pixel by the function illustrated in block h in Fig. 2. Frames are processed one axial scan at a time, each corresponding to a line in the final image. The first pixel in the first axial scan and the last pixel in the last axial scan of a frame are tagged with a frame marker carried over with the data to the PC. This simplifies the reconstruction of the images on the PC. Block j in Fig. 2 is a custom USB2.0 interface that links to the PC with a data rate of more than 10 Mbytes/s. The advantage of an USB2.0 interface is that it enables the display software to be implemented on laptop PCs, which all have built-in USB2.0 interfaces today.

2.1.6 *Scan control and data-flow control*

Axial scan rate is 4 kHz. Only the data acquired during the forward scan are processed. The center frequency is set by the EOM (JDSU, PM-130-005), which is driven by a sawtooth waveform[37] setting the center frequency of the interferogram at 3.2 MHz. The lateral scan is made by a galvanometer model 6220 from Cambridge Technology (Lexington, Massachusetts).

A controller for the EOM as well as the lateral scanning is implemented in the FPGA. The driver for the RSOD (Electro-Optical Products Corporation, Glendale, New York, SC-30-8 × 9-16-4000) delivers a trigger to this module at the start of each axial scan, which in turn paces the acquisition of the data, and the lateral movement. The controller ensures that the phase of the signal to the EOM and to the lateral movement is constant from scan to scan. The controller also takes account of the number of sequential scans at each position. In case there is congestion in the downstream consumption of acquired data, the transverse scan is stopped until room for new data becomes available. There is a data buffer on the FPGA that always will hold at least one additional processed axial scan. The halting of the lateral scan is made between two lateral positions to not interfere with the critical timing required for phase shift measurements.

2.1.7 *Antimotion algorithm*

Bulk movement will result in a phase shift, which in this application is unwanted. To suppress this effect, a method described in Ref. 48 is implemented. On each processed axial scan a histogram is made of the phase shift for each pixel having envelope amplitude above a given threshold. This thresholding improves the noise properties. The histogram is subsequently searched for the most frequent phase-shift value. In scans where only a small part of the pixels are imaging blood flow, this phase shift is a good measure of the block movement. Before display, this value is subtracted from the measured Doppler values, thus suppressing bulk movement.

2.1.8 *Display and user interface*

The software in the PC is written in LabVIEW (National Instruments, Austin, Texas). Figure 6 shows a block diagram of the most important parts. Data from the FPGA are read via the USB2.0 interface. As the envelope (16 bit) and Doppler shift data (16 bit) are interleaved, the block “split data” in Fig. 6 extracts the pixels into a structural and Doppler image. After application of the antimotion algorithm, each pixel is applied a false color. An image is built that is the structural image with an overlay of the Doppler image. The overlay uses two programmable thresholds: one on the envelope value, and one on the absolute value of the Doppler phase shift. A given pixel is displayed with its false color phase shift value if both the envelope and the phase shift are above their threshold values. Otherwise, the false color value of the envelope is displayed.

3 Results

3.1 *Phantom Experiments*

To test the system’s ability to detect velocities, we did measurements on a flow phantom with known flow velocity. A picture of the setup used for the measurements is shown in Fig. 7(a). The stationary solid phantom was a mixture of epoxy resin, hardener, ink, and TiO_2 particles aiming for optical properties close to biological tissue. In a depth of 150 μm in the stationary phantom, a small flow channel with a diameter of 400 μm had been drilled as shown in Fig. 7(b). For all measurements, we used an Intralipid 2% solution for the flow phantom, and an angle of 80.2 deg between the flow channel and the optical beam was estimated based on measurements of the surface angle [76.2 deg, as indicated in Fig. 7(b)] before and after the experiment. An example of a Doppler OCT image is shown in Fig. 8, together with the flow profile through the center of the flow channel. To extract the peak or maximum velocity in the flow channel, a second-order polynomial fit is used. In Fig. 9, the peak velocity determined by the Doppler OCT system is plotted as a function of the pump peak velocity. As expected for a laminar flow, the curve shows a

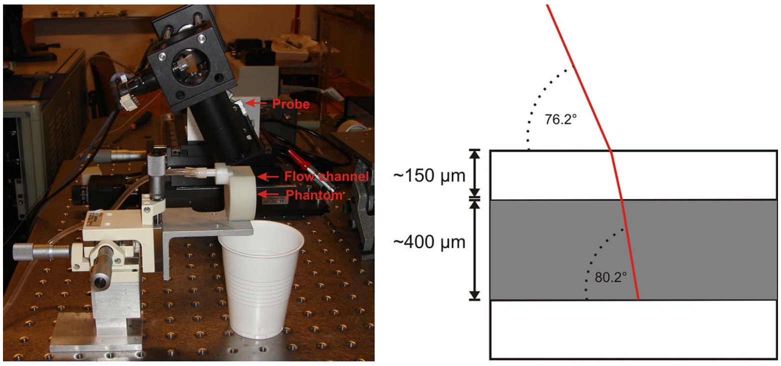

(a) **(b)**

Fig. 7 Setup used for the phantom measurements: (a) Photograph of the probe and phantom. (b) The flow channel is positioned about 150 μm below the surface of the stationary phantom. The angle between the flow direction and the optical beam is 80.2 deg.

linear relation between the pump flow velocity and the velocity measured with the Doppler OCT system. A minimum detectable average flow velocity of ~0.3 mm/s was estimated.

3.2 *In Vivo Imaging of Cardiac Dynamics in the Chick Embryo*

Doppler imaging was performed on day-2 and day-9 chick embryos in shell-less culture on a special positioning stage that allows movement of the embryo in x and y directions. Fertilized chicken eggs (White Leghorn, Gallus gallus) were obtained from a commercial supplier (Lohmann Tierzucht, Cuxhaven, Germany). Eggs were incubated at 38 °C and 75% relative humidity. After 48 h of incubation, the eggs were removed from the incubator. The eggshell was cracked and the whole content of the egg (albumen, yolk with the embryo) was transferred to a sterile hexagonal polystyrene weighing boat in a petri dish with water and reincubated until scanning with OCT. Day-2 hearts are looped early heart tubes. Other embryos were kept in the incubator until day 9; this is the stage when the chick heart is fully formed.

Figure 10 demonstrates a cross section of a day-2 (HH stage 14) chick heart tube in the region of the outflow tract

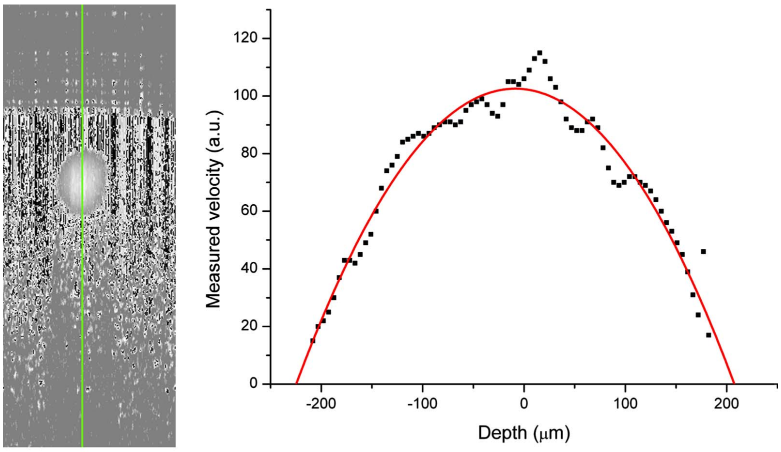

(a) **(b)**

Fig. 8 (a) Doppler image with a pump peak velocity of 4.5 mm/s. The green vertical line indicates the A-scan position used for extraction of the peak velocity. (b) Corresponding velocity profile (squares). A parabolic fit is used to estimate the peak velocity (solid curve). (Color online only.)

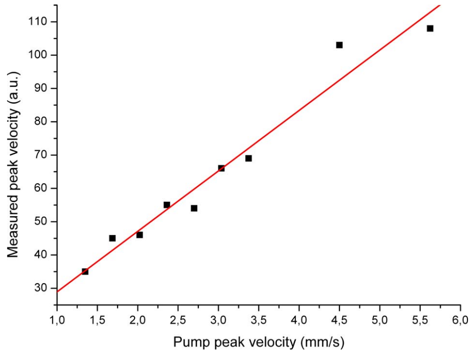

Fig. 9 The peak velocity determined by the Doppler OCT system as a function of the pump peak velocity.

visualized by OCT [Fig. 10(a)] and color Doppler OCT [Fig. 10(b)]. Arrows in Fig. 10(a) indicate lumen of a heart tube filled with blood that is detected by color Doppler OCT, as shown in Fig. 10(b). Figure 11 is the visualization of a vitelline vessel in a day-9 chick embryo by OCT and dimensional relations of vessel size to embryo size. Video 1 is an *in vivo* recording of a pulsating vitelline artery of a day-9 chick heart visualized by color Doppler OCT. The rhythmical pulsation of the vessel shown in the movie reflects the regular heart beat with periodic ejections of blood into the peripheral vitelline arteries. Video 2 is an *in vivo* recording of blood flow in the aorta in a day-9 chick heart visualized by color Doppler OCT in the sagittal plane. Video 3 is an *in vivo* recording of a color Doppler OCT scan demonstrating established blood flow in the right coronary artery (RCA) (yellow box) arising from the ascending aorta in a day-9 chick heart in the sagittal plane. Note the filling of RCA during diastole when the vessel becomes fully visible shortly after the start of recording in the movie. Note also the rhythmical contraction of the right ventricle, where the left ventricle is not depicted because of penetration limitation for deeper regions >2 mm due to high scattering of tissue (for the same reasons the stem of the left coronary artery could not be imaged clearly, and thus not demonstrated here).

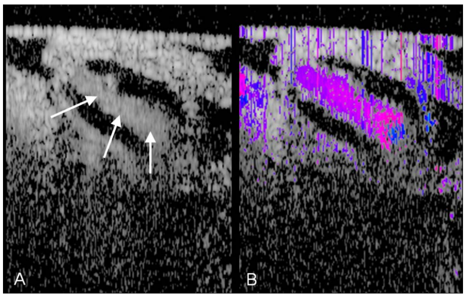

Fig. 10 Cross section of HH stage 14 chick heart tube in the region of the outflow tract visualized by (a) OCT and (b) color Doppler OCT (recording frame rate 2.5 frames/s). Arrows in (a) indicate lumen of heart tube filled with blood that is detected by color Doppler OCT, as shown in (b). (Color online only.)

4 Conclusion

We demonstrate a field programmable gate-array-based real-time optical Doppler tomography system. A complex-valued bandpass filter was used for the first time in OCT signal processing to create the analytic signal. This method simplifies the filter design, and allows an efficient and compact implementation by combining the conversion to an analytic signal with a pulse shaping function without the need for extra resources, as compared to the Hilbert transform method. Flow phantom experiments, and the use of this system for *in vivo* imaging of cardiac dynamics in the chick embryo, are presented. The visualization of blood flow in the early embryonic heart as well as in the aorta, small peripheric vitelline vessels, and coronary arteries of fully formed chick hearts are demonstrated. Finally, use of the FPGA is not restricted to time-domain OCT, but can be applied to process any digital signal and consequently also signals from frequency-domain OCT systems.

Appendix: Use of Complex Filter to Generate Analytic Signal

Let the real, sampled OCT signal from the detector be $x[n]$, where n is the sample index. The signal is multiplied by a complex exponential $\exp(-j\omega_0 n)$, where ω_0 is the radian frequency. The result is $y_1[n]$, and its real and imaginary parts are then in turn passed through a linear time-invariant discrete filter with a real-valued impulse response $h[n]$. The complex result $y_2[n]$ is subsequently multiplied by the exponential $\exp(j\omega_0 n)$. This procedure is illustrated in Fig. 12.

The response $y[n]$ can be written as

$$y[n] = \exp(j\omega_0 n)\{[x[n]\exp(-j\omega_0 n)]^* h[n]\}, \tag{10}$$

where * represents a convolution. Alternatively, this can be written as

$$y[n] = \exp(j\omega_0 n) \sum_{k=-\infty}^{\infty} x[k]\exp(-j\omega_0 k)h[n-k], \tag{11}$$

or equivalently

$$y[n] = \sum_{k=-\infty}^{\infty} x[k]h[n-k]\exp[j\omega_0(n-k)]. \tag{12}$$

Interpreted as a convolution, we can rewrite this to obtain

$$y[n] = x[n]^*\{h[n]\exp(j\omega_0 n)\}. \tag{13}$$

The signal from the detector can be approximated by a modulated real-valued sinusoidal-wave signal with carrier frequency ω_c, which can be written as

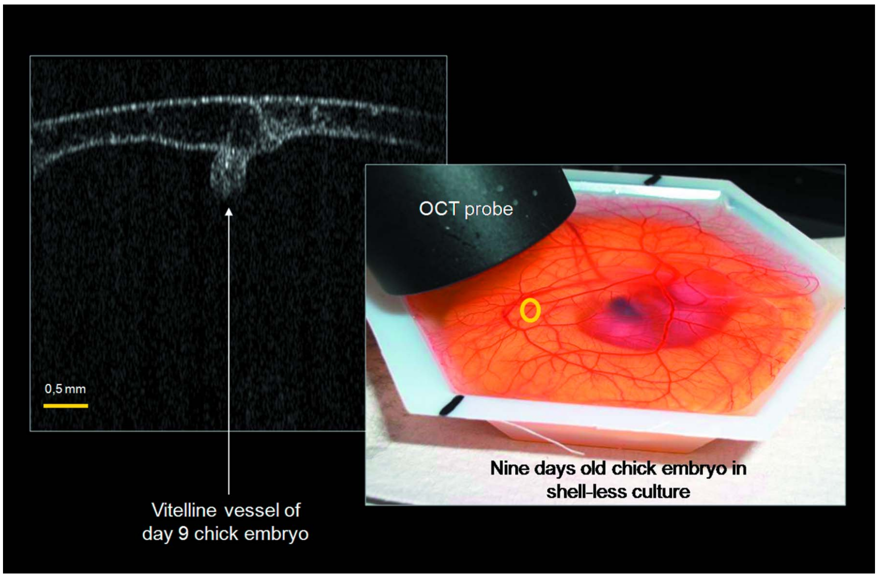

Fig. 11 Visualization of a vitelline vessel in a day-9 chick embryo by OCT and dimensional relations of vessel size to embryo size.

$$
\begin{aligned}
x[n] &= a[n]\cos(\omega_C n + \phi[n]) \\
&= \mathrm{Re}\{a[n]\exp(j\phi[n])\exp(j\omega_C n)\}, \qquad (14)
\end{aligned}
$$

where $a[n]$ is the envelope and $\phi[n]$ is the phase modulation. Equation (14) is equivalent to

$$
x[n] = \frac{1}{2}a[n]\{\exp[j(\omega_C n + \phi[n])] + \exp[-j(\omega_C n + \phi[n])]\}. \qquad (15)
$$

Inserting Eq. (15) into Eq. (13), we get

$$
\begin{aligned}
y[n] = \Big(&\frac{1}{2}a[n]\{\exp[j(\omega_C n + \phi[n])] + \exp[-j(\omega_C n \\
&+ \phi[n])]\}\Big)^* \; [h[n]\exp(j\omega_0 n)], \qquad (16)
\end{aligned}
$$

which also can be written as two convolutions

$$
\begin{aligned}
y[n] = &\frac{1}{2}\{a[n]\exp[j(\omega_C n + \phi[n])]\}^*[h[n]\exp(j\omega_0 n)] \\
&+ \frac{1}{2}\{a[n]\exp[-j(\omega_C n + \phi[n])]\}^*[h[n]\exp(j\omega_0 n)]. \qquad (17)
\end{aligned}
$$

If we define the modulation $g[n]=a[n]\exp(j\phi[n])$, and let $G[\exp(j\omega)]$ be its Fourier transform, Eq. (17) becomes

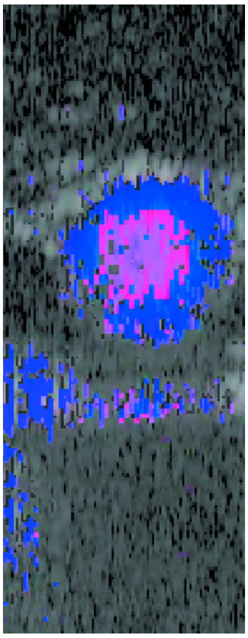

Video 1. *In vivo* recording of a pulsating vitelline artery of a day-9 chick heart visualized by color Doppler OCT. The rhythmical pulsation of the vessel reflects the regular heart beat with periodic ejections of blood into the peripheral vitelline arteries. (Color online only.) (MOV 1.2 MB.) [URL: http://dx.doi.org/10.1117/1.3081062.1].

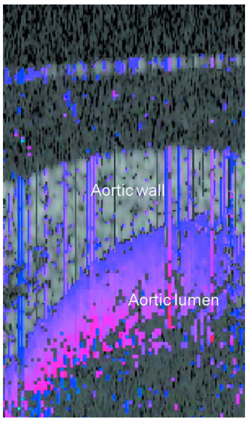

Video 2. *In vivo* recording of blood flow in the aorta in a day-9 chick heart visualized by color Doppler OCT in the sagittal plane. (Color online only.) (MOV 1.0 MB.)
[URL: http://dx.doi.org/10.1117/1.3081062.2].

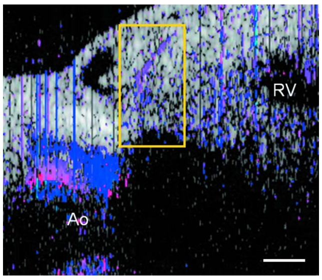

Video 3. *In vivo* recording of a color Doppler OCT scan demonstrating established blood flow in the right coronary artery (RCA) (yellow box) arising from the ascending aorta (Ao) in a day-9 chick heart in the sagittal plane. Note the filling of RCA during diastole when the vessel becomes fully visible shortly after the start of recording. Note also the rhythmical contraction of the right ventricle (RV), where the left ventricle is not depicted because of penetration limitation for deeper regions >2 mm due to high scattering of tissue (for the same reasons the stem of the left coronary artery could not be imaged clearly, and thus not demonstrated here). Bar=100 μm. (Color online only.) (MOV 1.1 MB.)
[URL: http://dx.doi.org/10.1117/1.3081062.3].

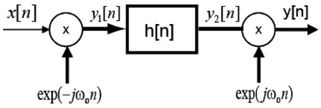

Fig. 12 Complex bandpass and phase-splitting filter. Wide lines are complex and narrow lines are real-valued signals.

$$y[n]=\frac{1}{2}[g[n]\exp(j\omega_C n)]^*(h[n]e^{j\omega_0 n}) + \frac{1}{2}[g^*[n]\exp(-j\omega_C n)]^*[h[n]\exp(j\omega_0 n)]. \tag{18}$$

The Fourier transform of Eq. (18) gives this result

$$Y[\exp(j\omega)]=\frac{1}{2}G\{\exp[j(\omega-\omega_C)]\}H\{\exp[j(\omega-\omega_0)]\} + \frac{1}{2}G\{\exp[j(\omega+\omega_C)]\}H\{\exp[j(\omega-\omega_0)]\}. \tag{19}$$

By selecting $\omega_c \approx \omega_0$, and letting $h[n]$ be a low-pass filter structure with a bandwidth such that $G\{\exp[j(\omega+\omega_c)]\}$ and $H\{\exp[j(\omega-\omega_0)]\}$ are nonoverlapping, the second term in Eqs. (15)–(19) can be neglected, giving the approximate filtered output $\tilde{y}[n]$

$$\tilde{y}[n]=\frac{1}{2}[g[n]\exp(j\omega_C n)]^*[h[n]\exp(j\omega_0 n)], \tag{20}$$

or in the frequency domain

$$\tilde{Y}[\exp(j\omega)]=\frac{1}{2}\{G(\exp[j(\omega-\omega_C)])\}H\{\exp[j(\omega-\omega_0)]\}. \tag{21}$$

Rearranging terms of Eq. (20) gives

$$\tilde{y}[n]=\frac{1}{2}\exp(j\omega_C n)\{g[n]^*(h[n]\exp[j(\omega_0-\omega_C)n])\}. \tag{22}$$

This shows that the output looks as if the modulation $g[n]=a[n]\exp(j\phi[n])$ is filtered through the frequency-shifted low-pass filter $h[n]\exp[j(\omega_0-\omega_c)n]$ and subsequently multiplied with a complex sinusoid $\exp(j\omega_c n)$ with the original carrier frequency of $x[n]$.

To reliably reproduce the envelope and phase modulation, the filter $h[n]\exp[j(\omega_0-\omega_c)n]$ should have sufficient bandwidth to pass the spectrum of $g[n]$, i.e., $H\{\exp[j(\omega-\omega_0)]\}$ should overlap $G\{\exp[j(\omega-\omega_c)]\}$. By choosing $h[n]$ to have linear phase, which is simple for a digital FIR filter, there will be no dispersion in the filter, and the phase of the output reliably reproduces the phase of the interferogram within the passband.

In an OCT system, both the temporal pulse shape and the noise content are important parameters. The response should have little or no ringing, but still sharp edges. Sharp edges mean wide bandwidth and thus more noise will be let through. Our implementation has a response with Gaussian-shaped approximation, which makes a good compromise between temporal response smoothness and bandwidth.

Note that the filtering process illustrated in Fig. 12 is only symbolic. In accordance with Eq. (13), the filter is actually implemented as two real FIR filters operating on the same signal $x[n]$. This can be written as

$$y[n] = x[n]^*\{h[n]\cos(\omega_0 n)\} + jx[n]^*\{h[n]\sin(\omega_0 n)\}. \qquad (23)$$

The precalculated impulse responses of the two filters are thus

$$h_{re}[n] = h[n]\cos(\omega_0 n) \quad \text{and } h_{\mathrm{im}}[n] = h[n]\sin(\omega_0 n). \qquad (24)$$

Acknowledgments

This work was supported by a research grant of the Braukmann Wittenberg Heart Foundation to Yelbuz, and by the Danish Research Agency (BIOPHOT framework program, grant number 26-02-0020). We thank P. Wübbolt-Lehmann, K. Reccius, and J. Misske, all at Hannover Medical School, for their technical assistance in embryo preparations for shell-less culture. Furthermore, we thank Thomas M. Jørgensen and Harold T. Yura for valuable discussions regarding the signal processing.

References

1. C. K. Phoon, "Circulatory physiology in the developing embryo," *Curr. Opin. Pediatr.* **13**, 456–464 (2001).
2. B. B. Keller, "Embryonic cardiovascular function, coupling, and maturation: a species view," in *Development of Cardiovascular Systems*, W. W. Burggren and B. B. Keller, Eds., pp. 65–87, University Press, (1998).
3. P. J. Gruber and J. A. Epstein, "Development gone awry: congenital heart disease," *Circ. Res.* **94**, 273–283 (2004).
4. A. C. Gittenberger-de Groot, M. M. Bartelings, M. C. Deruiter, and R. E. Poelmann, "Basics of cardiac development for the understanding of congenital heart malformations," *Pediatr. Res.* **57**, 169–176 (2005).
5. J. I. Hoffman, "Incidence of congential heart disease, I: postnatal incidence," *Pediatr. Cardiol.* **16**, 103–113 (1995).
6. J. I. Hoffman and S. Kaplan, "The incidence of congenital heart disease," *J. Am. Coll. Cardiol.* **39**, 1890–1900 (2002).
7. B. B. Keller, L. J. Liu, J. P. Tinney, and K. Tobita, "Cardiovascular developmental insights from embryos," *Ann. N.Y. Acad. Sci.* **1101**, 377–388 (2007).
8. D. E. Stewart, M. L. Kirby, and K. K. Sulik, "Hemodynamic changes in chick embryos precede heart defects after cardiac neural crest ablation," *Circ. Res.* **59**, 545–550 (1986).
9. S. Stekelenburg-de Vos, N. T. Ursem, W. C. Hop, J. W. Wladimiroff, A. C. Gittenberger-de Groot, and R. E. Poelmann, "Acutely altered hemodynamics following venous obstruction in the early chick embryo," *J. Exp. Biol.* **206**, 1051–1057 (2003).
10. S. A. Boppart, M. E. Brezinski, B. E. Bouma, G. J. Tearney, and J. G. Fujimoto, "Investigation of developing embryonic morphology using optical coherence tomography," *Dev. Biol.* **177**, 54–63 (1996).
11. S. A. Boppart, G. J. Tearney, B. E. Bouma, J. F. Southern, M. E. Brezinski, and J. G. Fujimoto, "Noninvasive assessment of the developing Xenopus cardiovascular system using optical coherence tomography," *Proc. Natl. Acad. Sci. U.S.A.* **94**, 4256–4261 (1997).
12. T. M. Yelbuz, M. A. Choma, L. Thrane, M. L. Kirby, and J. A. Izatt, "Optical coherence tomography: a new high-resolution imaging technology to study cardiac development in chick embryos," *Circulation* **106**, 2771–2774 (2002).
13. M. A. Choma, S. D. Izatt, R. J. Wessells, R. Bodmer, and J. A. Izatt, "Images in cardiovascular medicine: *in vivo* imaging of the adult Drosophila melanogaster heart with real-time optical coherence tomography," *Circulation* **114**, e35–e36 (2006).
14. M. W. Jenkins, F. Rothenberg, D. Roy, V. P. Nikolski, Z. Hu, M. Watanabe, D. L. Wilson, I. R. Efimov, and A. M. Rollins, "4D embryonic cardiography using gated optical coherence tomography," *Opt. Express* **14**, 736–748 (2006).
15. M. W. Jenkins, D. C. Adler, M. Gargesha, R. Huber, F. Rothenberg, J. Belding, M. Watanabe, D. L. Wilson, J. G. Fujimoto, and A. M. Rollins, "Ultrahigh-speed optical coherence tomography imaging and visualization of the embryonic avian heart using a buffered Fourier domain mode locked laser," *Opt. Express* **15**, 6251–6267 (2007).
16. M. W. Jenkins, P. Patel, H. Deng, M. M. Montano, M. Watanabe, and A. M. Rollins, "Phenotyping transgenic embryonic murine hearts using optical coherence tomography," *Appl. Opt.* **46**, 1776–1781 (2007).
17. M. W. Jenkins, O. Q. Chughtai, A. N. Basavanhally, M. Watanabe, and A. M. Rollins, "*In vivo* gated 4D imaging of the embryonic heart using optical coherence tomography," *J. Biomed. Opt.* **12**, 030505 (2007).
18. W. Luo, D. L. Marks, T. S. Ralston, and S. A. Boppart, "Three-dimensional optical coherence tomography of the embryonic murine cardiovascular system," *J. Biomed. Opt.* **11**, 021014 (2006).
19. K. Norozi, L. Thrane, J. Männer, F. Pedersen, I. Wolf, S. Mottl-Link, H. P. Meinzer, A. Wessel, and T. M. Yelbuz, "*In vivo* visualization of coronary artery development by high-resolution optical coherence tomography (OCT)," *Heart* **94**, 130 (2008).
20. S. Yazdanfar, M. Kulkarni, and J. Izatt, "High resolution imaging of *in vivo* cardiac dynamics using color Doppler optical coherence tomography," *Opt. Express* **1**, 424–431 (1997).
21. V. X. D. Yang, M. L. Gordon, E. Seng-Yue, S. Lo, B. Qi, J. Pekar, A. Mok, B. C. Wilson, and I. A. Vitkin, "High speed, wide velocity dynamic range Doppler optical coherence tomography (part II): imaging *in vivo* cardiac dynamics of *Xenopus laevis*," *Opt. Express* **11**, 1650–1658 (2003).
22. A. Mariampillai, B. A. Standish, N. R. Munce, C. Randall, G. Liu, J. Y. Jiang, A. E. Cable, I. A. Vitkin, and V. X. D. Yang, "Doppler optical cardiogram gated 2D color flow imaging at 1000 fps and 4D *in vivo* visualization of embryonic heart at 45 fps on a swept source OCT system," *Opt. Express* **15**, 1627–1638 (2007).
23. M. W. Jenkins, O. Q. Chughtai, A. N. Basavanhally, M. Watanabe, and A. M. Rollins, "*In vivo* gated 4D imaging of the embryonic heart using optical coherence tomography," *J. Biomed. Opt.* **12**, 030505 (2007).
24. B. A. Filas, I. R. Bfimov, and L. A. Taber, "Optical coherence tomography as a tool for measuring morphogenetic deformation of the looping heart," *Anat. Rec.* **290**, 1057–1068 (2007).
25. A. F. Fercher, W. Drexler, C. K. Hitzenberger, and T. Lasser, "Optical coherence tomography—principles and applications," *Rep. Prog. Phys.* **66**, 239–303 (2003).
26. J. G. Fujimoto, M. E. Brezinski, G. J. Tearney, S. A. Boppart, B. Bouma, M. R. Hee, J. F. Southern, and E. A. Swanson, "Optical biopsy and imaging using optical coherence tomography," *Nat. Med.* **9**, 970–972 (1995).
27. J. G. Fujimoto, "Optical coherence tomography for ultrahigh resolution *in vivo* imaging," *Nat. Biotechnol.* **21**, 1361–1367 (2003).
28. J. A. Izatt, M. D. Kulkarni, S. Yazdanfar, J. K. Barton, and A. J. Welch, "*In vivo* bidirectional color Doppler flow imaging of picoliter blood volumes using optical coherence tomography," *Opt. Lett.* **22**, 1439–1441 (1997).
29. Z. Chen, T. E. Milner, D. Dave, and J. S. Nelson, "Optical Doppler tomographic imaging of fluid flow velocity in highly scattering media," *Opt. Lett.* **22**, 64–66 (1997).
30. S. K. Yan, D. Q. Piao, Y. L. Chen, and Q. Zhu, "Digital signal processor-based real-time optical Doppler tomography system," *J. Biomed. Opt.* **9**, 454–463 (1997).
31. A. W. Schaefer, J. J. Reynolds, D. L. Marks, and S. A. Boppart, "Real-time digital signal processing-based optical coherence tomography and Doppler optical coherence tomography," *IEEE Trans. Biomed. Eng.* **51**, 186–190 (2004).
32. V. Westphal, S. Yazdanfar, A. M. Rollins, and J. A. Izatt, "Real-time, high velocity-resolution color Doppler optical coherence tomography," *Opt. Lett.* **27**, 34–36 (2002).
33. B. H. Park, M. C. Pierce, B. Cense, and J. F. de Boer, "Real-time multi-functional optical coherence tomography," *Opt. Express* **11**, 782–793 (2003).
34. V. X. D. Yang, M. L. Gordon, B. Qi, J. Pekar, S. Lo, E. Seng-Yue, A. Mok, B. C. Wilson, and I. A. Vitkin, "High speed, wide velocity dynamic range Doppler optical coherence tomography (Part I): System design, signal processing, and performance," *Opt. Express* **11**, 794–809 (2003).
35. H. Engelbrecht Larsen, R. Thorup Nilsson, L. Thrane, F. Pedersen, T. Martini Jørgensen, and P. E. Andersen, "Optical Doppler tomography based on a field programmable gate array," *Biomed. Signal Process. Control* **3**, 102–106 (2008).
36. G. J. Tearney, B. E. Bouma, and J. G. Fujimoto, "High-speed phase- and group-delay scanning with a grating-based phase control delay line," *Opt. Lett.* **22**, 1811–1813 (1997).
37. J. F. de Boer, C. E. Saxer, and J. S. Nelson, "Stable carrier generation and phase-resolved digital data processing in optical coherence tomography," *Appl. Opt.* **40**, 5787–5790 (2001).
38. Y. Zhao, Z. Chen, C. Saxer, S. Xiang, J. F. de Boer, and J. S. Nelson, "Phase-resolved optical coherence tomography and optical Doppler tomography for imaging blood flow in human skin with fast scanning speed and high velocity sensitivity," *Opt. Lett.* **25**, 114–116 (2000).
39. A. M. Rollins, M. D. Kulkarni, S. Yazdanfar, R. Ung-arunyawee, and J. A. Izatt, "*In vivo* video rate optical coherence tomography," *Opt. Express* **3**, 219–229 (1998).
40. A. V. Oppenheim, R. W. Schafer, and J. R. Buck, *Discrete-Time Signal Processing*, 2nd ed., p. 205, Prentice Hall, Englewood Cliffs, NJ (1998).
41. A. V. Oppenheirp, R. W. Schafer, and J. R. Buck, *Discrete-Time Signal Processing*, 2nd ed., pp. 180–184, Prentice Hall, Englewood Cliffs, NJ (1998).
42. D. F. Elliott, *Handbook of Digital Signal Processing Engineering*

Applications, pp. 225–226, Academic Press, San Diego, CA (1987).
43. A. V. Oppenheim, R. W. Schafer, and J. R. Buck, *Discrete-Time Signal Processing*, 2nd ed., p. 795, Prentice Hall, Englewood Cliffs, NJ (1998).
44. J. E. Volder, "The CORDIC trigonometric computing technique," *IRE Trans. Electron. Comput.* **EC-8**, 330–334 (1959).
45. J. C. Bajard, S. Kla, and J. M. Muller, "BKM: a new hardware algorithm for complex elementary functions," *IEEE Trans. Comput.* **46**, 955–936 (1994).
46. J. A. Jensen, *Estimation of Blood Velocities Using Ultrasound*, Cambridge University Press, Boston, MA (1996).
47. C. Kasai, K. Namekawa, A. Koyano, and R. Omoto, "Real-time two-dimensional blood flow imaging using an autocorrelation technique," *IEEE Trans. Sonics Ultrason.* **SU-32**, 458–463 (1985).
48. V. X. D. Yang, M. L. Gordon, A. Mok, Y. Zhao, Z. Chen, R. S. C. Cobbold, B. C. Wilson, and I. A. Vitkin, "Improved phase-resolved optical Doppler tomography using Kasai velocity estimator and histogram segmentation," *Opt. Commun.* **208**, 209–214 (2002).

Lars Thrane received his MSc degree in physics and chemistry in 1995 from Odense University, Denmark, and his PhD degree in physics in 2001 from the Technical University of Denmark (DTU), Denmark. Currently, he is holding a Senior Scientist position at DTU Fotonik, Department of Photonics Engineering, DTU. From 2001 to 2003, he worked as a post doc at the Optics and Fluid Dynamics Department, Risø National Laboratory, Denmark, including a stay for 5 months (February to June 2002) as a visiting post doc at the Biomedical Engineering Department, Duke University, North Carolina. From 2004 to 2008, he has been holding a scientist position; 2004 to 2007 at the Optics and Plasma Research Department, Risø National Laboratory, Denmark, and in 2008 at DTU Fotonik, Department of Photonics Engineering, DTU. His research interests include development of optical coherence tomography systems for biomedical applications.

Kambiz Norozi received his MD/PhD degree in 1991 from the Medical School of Hannover (MHH), Germany. Currently he is an associate professor of pediatrics (cardiology) in the Department of Pediatrics at the University of Western Ontario, London, Canada. Since June 2003 and until his move to Canada in October 2008, he worked as a consultant pediatric cardiologist in the Children Hospital of MHH. From June 2003 until January 2005, he was the head coordinator of the bicenter clinical research project (Hannover and Göttingen) investigating adolescents and adults with congenital heart defects (ACHD). From February 2005 until his move to Canada, he was the senior research associate in the Cardiovascular Development Research Laboratory at MHH. His research interests, besides ACHD, are *in vivo* imaging and functional analysis of the developing heart using technologies such as high-speed video recording and OCT.

Talât Mesud Yelbuz is a physician-scientist who received his MD/PhD degree in 1992 from Georg-August-University in Göttingen, Germany. Currently he is a professor of pediatrics (cardiology) in the Department of Pediatrics at McMaster University, and head of the Division of Cardiology at McMaster Children's Hospital of Hamilton Health Sciences Center, Hamilton Ontario, Canada. He is also a member in the School of Biomedical Engineering (SBME), associate member in the Department of Mechanical Engineering at McMaster University, and Director of the Cardiovascular Development Research Laboratory in SBME. Since October 2003 and until his move to Canada in August 2008, he worked as a consultant pediatric cardiologist and head of research in the Department of Pediatric Cardiology and Intensive Care Medicine at Hannover Medical School, Hannover, Germany. Here he developed and directed the Cardiovascular Development Research Laboratory for the last five years and was promoted to associate professor of pediatrics (cardiology) in December 2004. His research interests include *in vivo* imaging and functional analysis of the developing heart using technologies such as high-speed video recording, OCT, MRI, and micro-CT.

Biographies and photographs of the other authors not available.